Investigation of biomimetic fish scale arrays and leading-edge serrations on base flow modification for transition delay

Muthukumar Muthuramalingam

Thesis submitted for the degree of Doctor of Philosophy

Department of Mechanical Engineering & Aeronautics

City, University of London

December 2020

Contents

List of Figures

List of Tables

Acknowledgements

First and foremost, I would like to thank Prof. Christoph Bruecker who gave me a chance to pursue Doctoral research and for his motivation, continuous support and guidance. I would also like to thank Late Prof. S. Soundranayagam for motivating me to pursue research on fluid dynamics. I am grateful to Dr. Dhamotharan Veerasamy for recommending me to Prof. Christoph Bruecker and for technical and personal discussions along with Dr. Sathiskumar Anusuya Ponnusami. I thank Prof. O. N. Ramesh and Dr. A. P. Haran for providing academic recommendations for joining City, University of London. My current position is supported by the BAE Systems and German Research Foundation in the grant DFG BR 1494/32-1, which is also gratefully acknowledged. I would like to thank Prof. Ulrich Rist for allowing me to conduct experiments at University of Stuttgart, Germany and the guidance given by Dr. Dominik Puckert is also acknowledged. Thanks to Leo S. Villemin for his interest on fish scales and his generous willingness which made me involved in this project and contributes to a major part of this thesis. Technical inputs on the experiments from Dr. Chetan Jagadeesh is acknowledged. I thank Dr. Sudhakar Yogaraj for his technical discussions and encouragement. Furthermore, I would like to thank Avin Alexander, Dhinesh Raja, Suriyakumar, Anand Muthusamy, Sriram Ganesan, Vijaya Sankaran, Moses Rajkumar, Sarojmala, Dr Ajandan and Dr Rajesh for providing support at various levels. Thanks to the workshop technicians, Keith Pamment, Subramaniam Kugathasan, Grant Clow and Richard leach for their technical support. I would also like to thank my lab members Dr. Qianhui Li, Dr Mohamed Elshalakani and Omar Selim for their support and technical discussions. Sincere and heartfelt thanks to Edward Talboys for his support on multiple occasions on PIV, conducting experiments and language corrections. Finally and most importantly, I thank my parents and my wife for their motivation, support and sacrifice without which this work would not have been possible.

Abstract

Drag reduction techniques have been the crux of aerodynamic research for many decades due to their potential to reduce the use of fossil fuels and the resulting air pollution. One such strategy is to delay the laminar-turbulent transition employing active or passive flow control methods to maintain the laminar flow to a maximum extent which directly reduces the skin friction drag on the streamlined bodies. In this aspect, two biomimetic geometries inspired by fish scale arrays and the leading-edge serrations have been investigated in this work. Both geometries modify the base flow to be more stable and less susceptible to fundamental fluid instability, namely the Tollmien-Schlichting wave and the crossflow vortices.

Biomimetic fish scale arrays produce periodic and spatially varying velocity modulation known as streaks. The backward-facing step like flow in the central region and the zig-zag motion in the overlapping region of the scale arrays is the main factor to generate the streaky flow. When this streaky base flow interacts with the Tollmien-Schlichting wave the growth rate of the unstable wave is attenuated to delay the transition. The extent of the transition delay depends on the amplitude of the streaks and for the maximum streak amplitude, the streaky base flow can completely cancel the unstable Tollmien-Schlichting wave. This model can be customized on aerofoils where the transition is promoted by the Tollmien-Schlichting wave and to design a natural laminar flow aerofoil.

Biomimetic leading-edge serrations act like three-dimensional cascade blades which

are very different from the conventional vortex generators. The serrations turn the incoming flow towards the inboard portions of the wing and this flow turning was proved using flow visualisation study on a flat plate in a water tunnel. Large Eddy Simulations on a serrated aerofoil also indicate the inward turning of the flow to delay the instabilities on a swept wing. Based on the current findings, noise reduction is also hypothesized and therefore this special geometry should be further investigated for consideration in the development of silent flight.

Thesis structure

During my doctoral research period, three journals have been published in which I was the first author. This thesis is a compilation of all three journals which form a prospective publication format. Basic introduction on biomimcry and boundary layers are given in Chapter-1, followed by each publication as a separate chapter which will generally contain the following sections: (1) Abstract (2) Introduction with literature review (3) Materials and Methods (4) Results and (5) Discussion and Conclusions. At the end of every chapter a critical analysis section is added to discuss about the critical issues based on limitations and some new results. The publications are listed below with salient points to give a brief idea to the reader.

Publications

1) Muthuramalingam, M., Leo S. Villemin and Bruecker, C. (2019), 'Streak formation in flow over biomimetic fish scale arrays' , Journal of Experimental Biology **222**. - Published: 30 August 2019

- First order modelling of fish scale topology and fish scale array from measurements from European sea bass.
- Fluid simulations over biomimetic fish scale array revealed that fish scale array produces streaky base flow.
- This streaks was confirmed using flow visualisation behind biomimetic and real fish scale array .

- Drag reduction is observed for certain boundary layer to scale height ratio in a laminar flow condition.

2) Muthuramalingam, M., Dominik K. Puckert, Rist, U., and Bruecker, C. (2020), 'Transition delay using biomimetic fish scale arrays' , Scientific Reports **10**. - Published: 03 September 2020

- The biomimetic scale array was compared with many real fish scale arrays by visual inspection.
- Two different streak amplitudes were generated by the biomimetic fish scale array and was tested in the presence of Tollmien-Schlichting wave.
- Both models delayed transition when compared with the reference Blasius case which largely increased the laminar flow region, thus giving a large reduction in skin friction drag.
- Higher the streak amplitude, higher the tendency to attenuate the TS wave.

3) Muthuramalingam, M., Talboys, E., Wagner, H., and Bruecker, C. (2020), 'Flow turning effect and laminar control by the 3D curvature of leading edge serrations from owl wing' , Bioinspiration & Biomimetics. - Online: 02 November 2020

- Modelling of the three dimensional curved serrations to represent the real serrations.
- The serrations are compared with curved cascade blades which turn the flow based on the inlet flow angle and geometric variation.
- The serrations produce a crossflow which counteracts the velocity profiles which could delay swept wing transition. This flow turning was investigated using simulations and flow visualisation.
- The flow turning was also observed on a cambered aerofoil with serrations.

Chapter 1

Introduction

The introduction herein is intended to present the reader with the subjects of the research carried out in this work and the basics of the boundary layer and its related instability. It is not intended to provide a complete background, but to inform the reader of the basics related to the chapters of the thesis. Therefore, mainly review articles and standard textbooks are referred here, which can then be further researched based on the interest of the reader. A complete literature review is given for each chapter of this prospective publication-style thesis.

Evolution has developed various living organisms for their well-organized use of their bodies and structures to adapt to the environment and circumstances they experience. In recent times, nature has become a source of inspiration for humans to develop their technologies to solve complex problems in various fields. This field of research is known as Biomimetics and there are many examples of biomimicry, ranging from daily life activities to space exploration [1].

Few examples for applied bio-inspired technology are listed below. A daily life example is: hook and loop fastener was inspired from bur seeds which use its hooks to stick on to animals thus getting transported far away from its parent which leads to

[1] https://biomimicry.org/

pollination. In medicine: learning from the mosquito's mouth to develop a needle to reduce the pain. Technological innovations are: bullet train in Japan was inspired by the Kingfisher's beak, which reduces noise and power. Mercedes-Benz designed a bionic car inspired from boxfish resulting in low drag (Choi et al., 2012).

Biomimicry in energy, aeronautical and marine applications is essentially focused on energy enhancement, drag and noise reduction, which directly reduces energy expenditure and noise pollution. Recently, the aerodynamic aspect of maple seeds has been used to enhance power extraction by regulating the root leakage of the wind turbine by retrofitting. The leading-edge tubercles on humpback whale flippers are used to boost power generation in turbulent and unsteady wind conditions. Shark skin-inspired riblets are used to minimize the turbulent boundary layer drag at high Reynolds numbers and are highly likely to be used on aircraft. Hydrophobic coatings are studied to reduce the drag on boats and ships (Jiang et al., 2011). It should be emphasized here that these are only a few applications and researches which have been studied in the field of biomimicry which show that there are still many things which can be learnt from nature and which could focus on aeronautical applications.

Air travel has been on the rise in recent years and is projected to grow at a higher rate, which would restrict the use of fossil fuels. Even a small improvement in aircraft performance will significantly reduce fuel costs and also reduce pollutant levels. The main penalty for flying an aircraft comes from the drag induced by its motion. Among the various drag components, about 45% of drag is due to friction. This frictional drag is due to the turbulent boundary layer that forms over aircraft surfaces such as fuselage and wings. It is, therefore, necessary and vital to reduce this drag component to obtain a significant benefit in fuel usage. This thesis which comprises of three published articles will concentrate on the uses of potential biomimicry solutions to reduce skin friction drag. To provide a brief background information on boundary-layer instabilities, a short summary is given to make the thesis easier to read. This overview is not complete, however, interested readers can refer to literary works, such as (White, 2006; Panton, 2013; Schlichting and Gersten, 2017; Anderson, 2011). The following section will discuss concepts of boundary layer, instability and transition.

1.1 Boundary layer

When a body moves through a fluid or in a relative reference frame, when a fluid flow passes over the body, it influences and displaces the fluid which is much different from the free stream velocity. It is because of the shape of the body, which could be determined by inviscid flow (neglecting viscosity) using Euler's equation. This model gives zero drag in an incompressible flow that is considered to be a hydrodynamic paradox. Later on, the reason for this paradox was revealed by Prandtl in his famous experiment on diffusers, where the expected increase in pressure did not follow the inviscid flow assumption (Eckert, 2017). It was revealed that although the fluid flow away from the adjacent walls can be approximated by Euler's equations, the flow near the boundary is dominated by the viscosity of the fluid. Viscosity causes the fluid velocity to be zero near the wall and gradually increase to the free stream velocity away from the wall. This velocity variation within a small region is known as the boundary layer. This layer separates the viscous-dominated and inertia-dominated flow regions that are responsible for complicated fluid flow phenomena such as transition, turbulence and flow separation. Viscous flow over an aerofoil is shown in Fig.1.1 which gives a clear picture of the boundary layer region.

The boundary layer region imparts a shear stress on the surface of the body as shown in Eqn.1.1, where τ_{wall} is the shear stress at the wall, 'μ' is the dynamic viscosity of

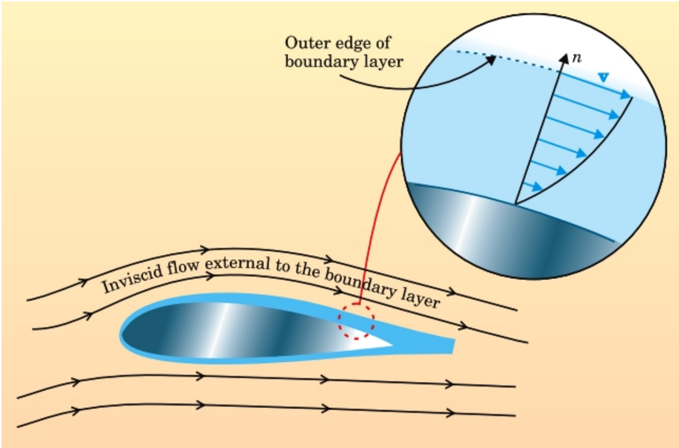

Figure 1.1: **Viscous flow over an aerofoil.** The blue coloured border depicts the thin boundary layer region. Inset shows the velocity profile inside the boundary layer. Source: Prandtl's boundary layer by John D. Anderson (Anderson, 2005).

the fluid and '$\frac{dU}{dy}$' is the velocity gradient at the surface ($y = 0$).

$$\tau_{wall} = \mu \frac{dU}{dy}\bigg|_{y=0} \tag{1.1}$$

Figure.1.2 shows typical velocity profiles in a laminar and turbulent flow. The laminar velocity profile has less velocity gradient which arises from the smooth flow of fluid particles which are well defined and predictable, whereas, the velocity gradient for a turbulent flow is more because of the mixing process due to the eddies in the flow. It is because of this reason laminar flows are more susceptible to boundary layer separation which increases the pressure drag while turbulent flow reduces or avoids separation but increases the skin friction drag. Hence, there is always a trade-off in fluid dynamics to make the flow laminar or turbulent.

Flow over any surface starts off initially with a laminar boundary layer and breaks down into a turbulent flow due to disturbances caused by surface imperfections or inlet flow turbulence. This is attributed to the receptivity of the boundary layer, which amplifies its most unstable modes. This primary instability can develop into secondary instabilities and promote transition which causes it to further break down into turbulent flow. This phenomenon takes place when the disturbances are very low thus named as a classic transition scenario. However, when the disturbances are too high, the laminar flow breaks down quickly into a turbulent flow thus establishing a 'bypass' transition.

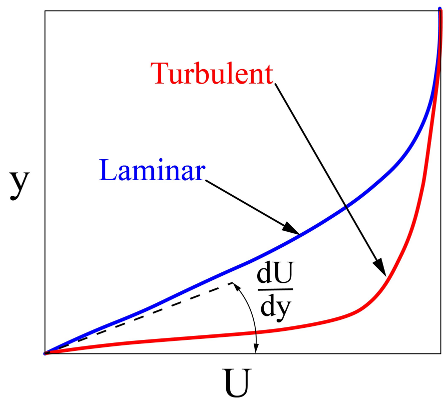

Figure 1.2: **Boundary layer velocity profile.** Blue curve - laminar, Red curve-turbulent and dashed line represents velocity gradient $\frac{dU}{dy}$ at wall.

In various aeronautical, marine and energy applications, the body which moves through the fluid consists of complex shapes like aerofoils and nearly axisymmetric bodies like fuselages and missiles where the pressure and roughness variation on the body is inevitable and changes the flow situation from case to case. Therefore, researchers have classified the fluid flow experiments based on a combination of various parameters to study its individual effects. For example, the pressure gradient was neglected by considering the flow on a flat plate at zero incidence by varying the inlet flow turbulence, surface roughness and discrete patterned roughness. In the next section, fluid flow instabilities will be discussed.

1.2 Flow stability

The motion of the viscous fluid flow is modelled by Navier-Stokes equations. The governing differential equation for incompressible, Newtonian fluid flow is given in

Eqn.1.2, where **'U'** represents the fluid velocity in x, y and z directions, 'p' denotes pressure and $\mu\nabla^2\mathbf{U}$ represents the viscous forces.

$$\rho\frac{d\mathbf{U}}{dt} = -\nabla p + \mu\nabla^2\mathbf{U} + f. \tag{1.2}$$

These equations when solved along with the continuity equation provides the variation of the flow variables in the considered domain known as base flow. As mentioned earlier, fluid flow instability is to be solved for the infinitesimal disturbances in the domain and to investigate whether these small disturbances grow either in time or space. For instance if the velocity profile considerably varies in the 'y' direction and the flow weakly varies in the 'x' direction, the flow variables are approximated as Q = $\mathbf{Q}$(y) + q(x,y,t), where $\mathbf{Q}$(y) refers to the base flow and q(x,y,t) denotes the infinitesimal fluctuations. Generally, the variable q(x,y,t) is approximated as $\mathbf{q}(y)e^{i(\alpha x-\omega t)}$, where '$\alpha$' is defined as the wavenumber and 'ω' is defined as the wave velocity (both α and ω are complex functions). When this functional form is plugged into the Navier-Stokes equation and with linearisation, it will result in the hydrodynamic stability equation called as Orr-Sommerfeld equation given in Eqn.1.3.

$$v'''' - 2\alpha^2 v'' + \alpha^2 v - iRe[(\alpha U - \omega)(v'' - \alpha^2 v) - \alpha U'' v] = 0 \tag{1.3}$$

This Orr-Sommerfeld equation is an Eigen value problem which can be solved either in space or time depending on the flow situation. If real wavenumbers are used then it will result in temporal stability whereas if real frequencies are used it results in spatial stability.

1.2.1 Tollmien–Schlichting wave instability

Two-dimensional laminar flow over a flat plate at zero incidence (no pressure gradient) is considered here. Therefore, the streamwise velocity 'U' varies strongly in wall-normal ('y') direction and weakly varies in the flow ('x') direction while there is no flow in the spanwise direction (W = 0). This results in self-similar velocity profiles known as Blasius boundary layer profile (Schlichting and Gersten, 2017) as shown in Fig.1.2 (see blue curve). Laminar flow over flat plate with zero imperfections will not exhibit any transition to turbulent flow mechanisms. The velocity profile is stable as there is no inflection point inside the boundary layer as required by the Rayleigh criteria $\frac{d^2U}{dy^2} = 0$ (Betchov and Criminale, 1967). However, because of the viscosity effects inside the boundary layer through the Orr-Sommerfeld equation, it was found that beyond a critical Reynolds number the Blasius profile is unstable for a combination of wavenumbers and frequencies. These waves were identified by Tollmien and Schlitching and was named after them (White, 2006). Figure.1.3 shows a typical plot of neutral stability curve for fluid flow over a flat plate with zero pressure gradient. The neutral stability curve is obtained by solving the Orr-Sommerfeld equation at different Reynolds numbers so that the waves are neutrally stable which means ($\alpha_i = 0$). The region inside the neutral stability curve amplifies the waves (unstable with $\alpha_i > 0$) and for any region outside the stability curve the flow is stable for any frequencies and wavelengths. For example, at a constant frequency ($\omega = const$ denoted by the dotted black line in Fig.1.3), the infinitesimal velocity fluctuations imposed before location X_F will decay until it reaches the location X_F where it enters the unstable region. From X_F until X_S the wave will amplify according to the stability analysis and after X_S the fluctuations will decay. This amplification is the primary cause of triggering transition on a flat plate boundary layer if the fluctuations are considerably higher.

Figure.1.4 depicts the different stages in a zero pressure gradient flat plate boundary

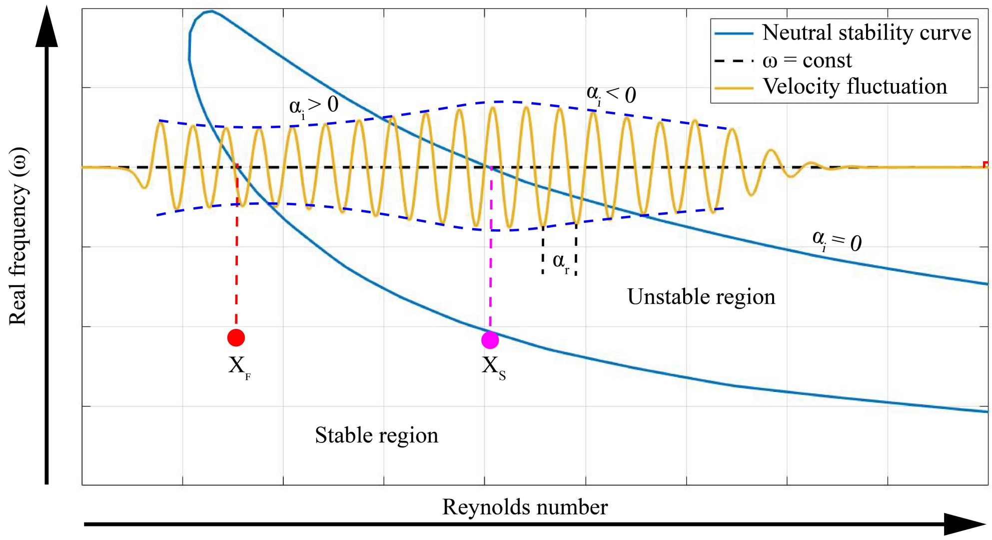

Figure 1.3: **Stability curve for flow over flat plate with zero pressure gradient.** Blue line - neutral stability curve, yellow line - velocity fluctuations, dotted blue line - envelope of velocity fluctuations.

layer from the leading edge of the flat plate (White, 2006). The flow is laminar and stable for disturbances upto certain extent of the flat plate, which is shown by the neutral stability curve in Fig.1.3. Once the waves enter the neutral stability limit, the two dimensional vorticity waves grow inside the boundary layer and is considered to be the primary instability mechanism. These vorticity waves are further distorted in spanwise direction (peaks and valleys) to generate streamwise vortices which induces spanwise flow to produce inflectional velocity profiles near the peak region which causes break down of the vortices. Further downstream, the vortices produce turbulent spots which are categorized as high frequency oscillations which later results in fully turbulent flow.

Other flow parameters considerably change the stability of laminar boundary layer profiles. For instance, a favourable pressure gradient ($\frac{dP}{dx} < 0$) stabilizes the flow and an adverse pressure gradient ($\frac{dP}{dx} > 0$) destabilizes the flow faster because of the inflectional velocity profiles. Also, depending on the level of inlet flow turbulence, significant changes occurs in the process of transition.

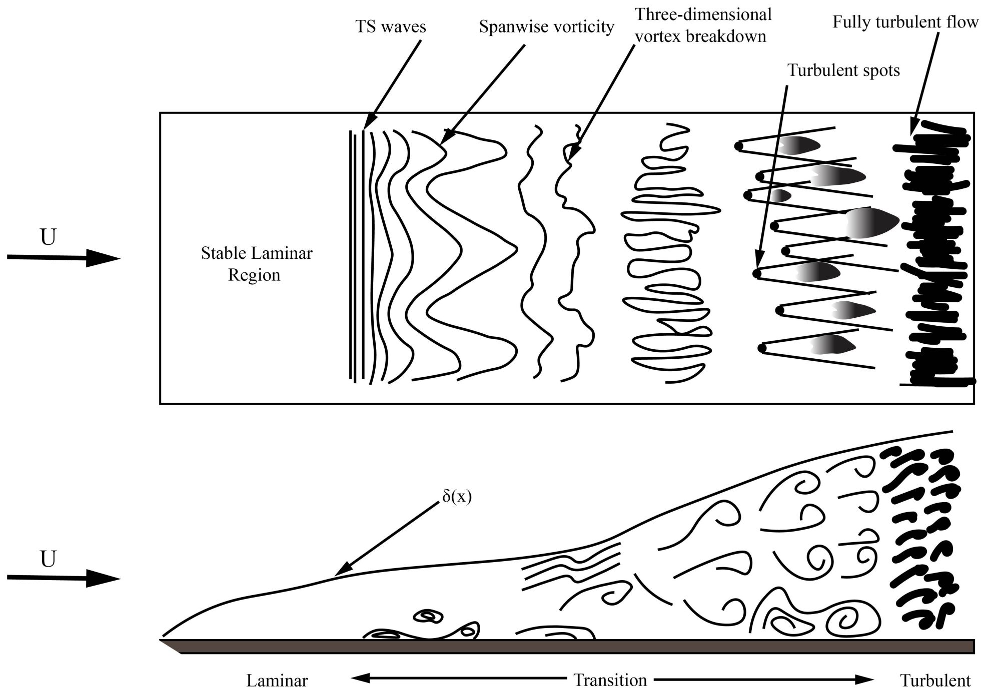

Figure 1.4: **Transition to turbulence from Tollmien-Schlichting wave instability.** Reproduced from White (White, 2006).

1.2.2 Crossflow instability

In this section, instability on flow over swept bodies with pressure gradient will be discussed. Flow over a swept wing is shown in Fig.1.5A, where 'U' is the free stream velocity and 'β' is the sweep angle of the wing. The flow coordinates are denoted by X and Z direction and X' and Z' coordinates represents the chordwise and spanwise direction with respective to the wing. A streamline approaching from free stream has a velocity component along the leading edge (towards outboard direction) and a favourable pressure gradient causing the potential streamlines to curve. The pressure gradient is balanced by the curvature of the streamlines in the outer layer. However, at the surface the velocity should be zero because of the viscosity while the pressure gradient induces a secondary flow. This crossflow is approximately perpendicular to the tangential direction of the local flow. The crossflow is similar to a wall jet like flow where the velocity is zero at the wall and at the edge of the boundary layer (Saric et al., 2003). Typical tangential and crossflow velocity profiles on a swept wing are shown in Fig.1.5B. It is evident that the crossflow velocity has an inflection point and therefor the crossflow velocity profile is unstable through Rayleigh criterion (Betchov and Criminale, 1967).

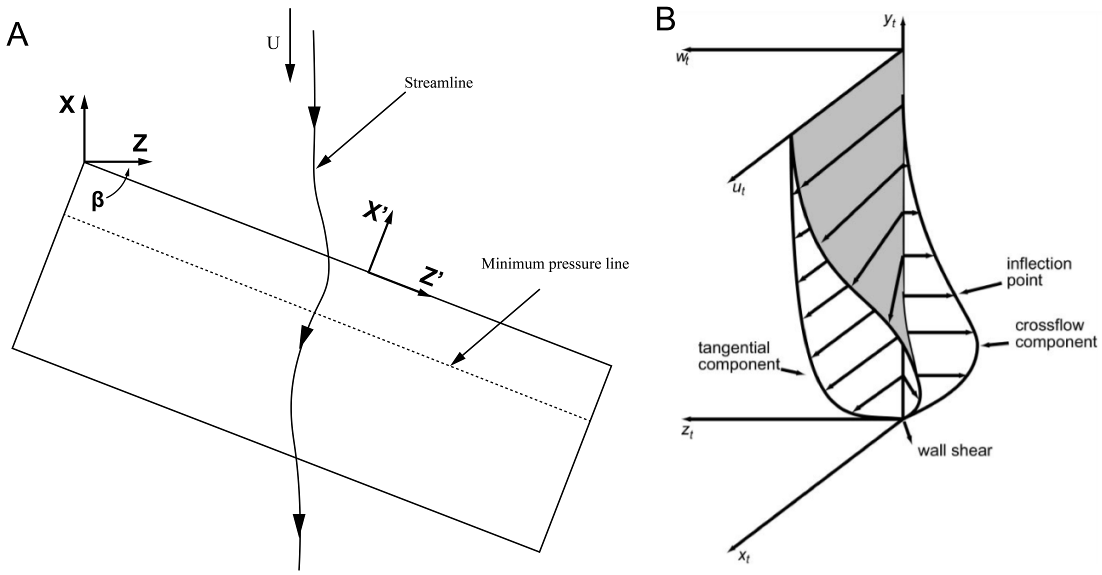

Figure 1.5: **Flow over swept wing and velocity profiles.** (A) Streamlines viewed from top view. Adapted from Houghton (Houghton et al., 2017). (B) Tangential and crossflow velocity profiles on a swept wing. From Saric (Saric et al., 2003).

This inflectional crossflow profiles generate stationary crossflow vortices which are almost aligned with the flow direction. These vortices can be stationary or travelling depending on the surface imperfections and free stream turbulence. These crossflow vortices are located along the spanwise direction with a spacing 'λ', which can be obtained by the linear stability analysis. Fig.1.6A shows the surface flow visualisation picture on a swept wing using oil flow and ultra-violet light illumination. The flow is from left to right and the crossflow vortices are visibly similar to streaks. Each streak is located at critical wavelength 'λ', which is the most fundamental instability mode. The darker regions behind the crossflow vortices indicate that the boundary layer is going through transition as the dye will be washed away quickly due to higher skin friction. The regular spacing of crossflow vortices before the transition region is shown in Fig.1.6B. These crossflow vortices are stationary and of zero frequency, hence, the most fundamental critical mode can be forced by placing cylindrical roughness elements at the leading edge of the aerofoil at the same critical spacing 'λ'.

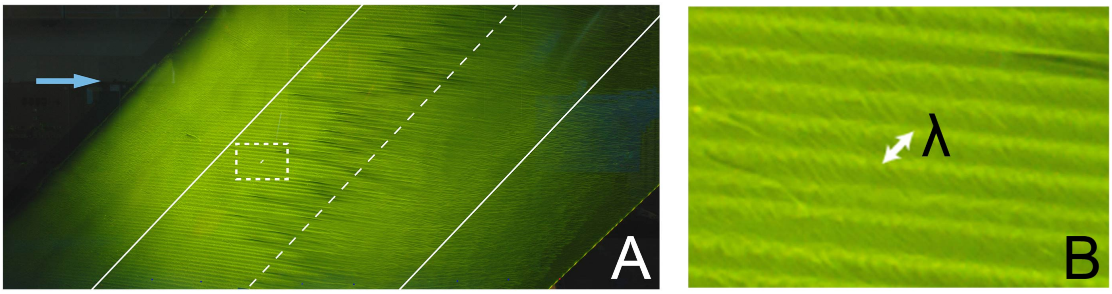

Figure 1.6: **Flow visualisation picture over a 45 deg swept wing.** (A) Crossflow vortices on a NACA 66018 aerofoil at Re $= 2.15 \cdot 10^6$ (flow is from left to right). (B) Enlarged picture from frame 'A' which shows the wavelength (λ) of the crossflow vortices. From Serpieri (Serpieri and Kotsonis, 2015).

The stationary crossflow vortices are weak in nature, however, they can vary the downstream velocity profiles considerably to initiate transition through secondary instability mechanisms. There are three modes in the secondary instability regimes, Type - I is based on streamwise velocity gradient along spanwise direction, Type - II is based on streamwise velocity gradient along wall normal location and Type - III is based on the interaction between stationary and travelling vortex modes (Serpieri and Kotsonis, 2016). As opposed to TS waves, the crossflow vortices grow strongly in a favourable pressure gradient region ($\frac{dP}{dx} < 0$). Therefore, to study the crossflow transition, accelerating flow region is mostly considered. In flow situations where a favourable pressure gradient is followed by an adverse pressure gradient region, as in flow over aerofoils, both TS and crossflow instabilities can coexist and can exhibit complex interactions (J. Ray and William S., 1999). Finally, swept wings with finite leading edge radius, can develop boundary-layer instability along the attachment line (Lin and Malik, 1997), however this instability is not considered in this thesis.

1.3 Motivation for Research

Most fluid flow instabilities have trivial features. Depending on the flow conditions, the primary instability mechanism makes the flow unstable in the linear regime. Later, they induce secondary instabilities which is a possible route to turbulence. Therefore, to delay transition, consideration should be given to the methods that suppress critical instabilities in order to extend the laminar flow. A review of such methods is given in (Beck et al., 2018). In this thesis, plausible flow control mechanism by the appendages which are present on two species have been investigated. Both these structures have a common aspect, that is, to change the base flow on the surface to make it more stable and delay transition by attenuating the flow instabilities.

The first research is on the fish scale array which is present on almost all bony fish species. The most relevant literature for this overview is the Physical Review Fluids from Lauder (Lauder et al., 2016) and is given here. Fish scales are made of collagen fibres which grow from scale pockets from the body and are covered with epidermis. When a fish larvae is hatched, it swims in the low Reynolds number regime using anguilliform mode (similar to eel and sea snake). While the larvae grows, it gradually increases its body length and swimming speed which transits from low Reynolds number regime to an inertial regime. Correspondingly, its morphology and swimming style changes to carrangiform or thunniform motion based on the species. For example, the larvae of sea bass (*Dicentrarchus labrax*) changes its swimming style from anguilliform to sub-carangiform approximately after 192 hours post hatch (hpH) (Olivier et al., 2013). Its final form is attained after 960 hpH where the total body length is about 30mm and the Reynolds number is more than 1000. Concurrently, the scales also develop on the body at the same time and after that the canals along the lateral line develops. It indicates that the effect of scales on the flow dynamics is very important even from the juvenile stage. Moreover the pattern of scale variation is similar between phylogenetically separated species indicating a common mode of behaviour with the environment for similar scale arrangement (Ibáñez et al., 2009). From the previous literature (Wainwright and Lauder, 2017; Lauder et al., 2016; Wainwright and Lauder, 2016; Wainwright et al., 2017) , very little light has been shed on the shape and arrangement of fish scales despite it being one of the most common species all over the globe. Very few studies hinted at the possible flow control mechanism based on the surface roughness of the scale array. However, considering fish scales only as roughness elements will undermine the ultimate potential of the scales for the following reasons. First, the scale shape or the topography is not arbitrary and has a definite structure. Secondly, the scale array has a pattern by itself and is not random in terms of the relative placement between them. Therefore, the combination of the shape and structure points out strongly that they would cause a major effect on the flow modulation and should be investigated in detail.

The second research is on the leading edge serrations on barn owl wings. Owl wings have many delicate features like velvet surface, trailing edge fringes, leading edge serrations and porous feather surfaces. All these features combinedly make the owl's flight extremely quiet which is useful for hunting its prey during night times. Although being researched more than a century, the precise flow control mechanism is not yet revealed in detail. An overview on plausible effects of these features are given in the annual review of fluid mechanics from Jaworski (Jaworski and Peake, 2020), while later on in the chapter more detailed references will be given. In this thesis, the effect of leading edge serrations is studied. In most of the previous investigations, the leading edge serrations were modelled as two dimensional structures which were placed at the leading edge of an unswept wing or a flat plate and only one investigation on curved serrations was close to the real serrations (Juknevicius et al., 2017). However, in a real owl's wing, the serrations are located where there is a significant change in the sweep angle of the wing. Moreover, the serrations are highly curved elements with considerable changes in the cross sectional size. Therefore, it is viable to examine the flow over the leading edge serrations with two major considerations. First, to accurately model the three dimensional serrations which are comparable with the real serrations. Second, to understand the flow behaviour of the three dimensional serrations on an swept wing or flat plate.

To summarize, this thesis will answer many questions on the flow manipulation of the fish scales and the three dimensional leading edge serrations using simulation and experimental results.

Chapter 2

Streak formation in flow over biomimetic fish scale arrays

Abstract

The surface topology of the scale pattern from the European Sea Bass (*Dicentrarchus labrax*) was measured using a digital microscope and geometrically reconstructed using Computer Assisted Design modelling. Numerical flow simulations and experiments with a physical model of the surface pattern in a flow channel mimic the flow over the fish surface with a laminar boundary layer. The scale array produces regular rows of alternating, streamwise low-speed and high-speed streaks inside the boundary layer close to the surface, with maximum velocity difference of about 9%. Low-velocity streaks are formed in the central region of the scales whereas the high-velocity streaks originated in the overlapping region between the scales. Thus, those flow patterns are linked to the arrangement and the size of the overlapping scales within the array. Because of the velocity streaks, total drag reduction is found when the scale height is small relative to the boundary-layer thickness, i.e. less than 10%. Flow simulations results were compared with surface oil-flow visualisations on the physical model of the biomimetic surface placed in a flow channel. The results show

an excellent agreement in the size and arrangement of the streaky structures. The existence of streaks is also proven on sea bass (*Dicentrarchus labrax*) and common carp (*Cyprinus carpio*) by surface flow visualisation. From comparison to recent literature about micro-roughness effects on laminar boundary layer flows it is hypothesized that the fish scales could delay transition which would further reduce the drag.

2.1 Introduction

All bodies, which move through a surrounding fluid, will generate a boundary layer over its surface because of the no-slip condition at the wall (Schlichting and Gersten, 2017). This boundary layer is a region of concentrated vorticity, which shears the fluid near the body surface and the work done to shear the fluid is the measure of the energy which is spent in locomotion (Anderson et al., 2001). The shear stress near the surface depends on the velocity gradient at the wall and the type of boundary layer, which exist near the surface (Schlichting and Gersten, 2017). If the boundary layer is laminar, the drag will be lesser, but it is more prone to separation at adverse pressure gradients, which increases the pressure drag. A turbulent boundary layer produces more skin friction because of the additional turbulent stress near the surface, however, it can sustain much stronger adverse pressure gradient which allows operating on off-design conditions (Schlichting and Gersten, 2017). There is always a trade-off in design to maintain the initial boundary layer laminar for the maximum extent so that the skin friction drag is reduced (Selig et al., 1995) and changing quickly to turbulent boundary layers in areas which are prone to separation. For marine vehicles, one may overcome larger friction by modifying the surface with a hydrophobic coating so that the fluid slips along the surface in contrast to the no-slip condition of an uncoated one. As a consequence, the skin friction is reduced which in turn reduces the net drag of the body (Ou et al., 2004; Daniello et al., 2009). This technology was motivated by the lotus-effect, reviewed recently in (Bhushan and Jung, 2006). This phenomenon contributes to self-cleaning of the surface which could reduce fouling in the marine environment (Bhushan et al., 2009). For large fast aquatic swimmer such as sharks, there has been numerous experimental and computational studies on the skin denticles (Wen et al., 2014; Oeffner and Lauder, 2012; Domel et al., 2018). Those were found to manipulate the near skin flow to reduce turbulent drag. However, little work has been done on smaller and slower fish with laminar or transitional boundary layer and the role of different arrangements and patterns of fish scales on their swimming behaviour and hydrodynamics. Up to now, there are only hypotheses about the role of fish scale in hydrodynamics, reported in a recent article by (Lauder et al., 2016) who claimed also that there is still no detailed proof of their hydrodynamic function. Wainwright and Lauder (Wainwright and Lauder, 2016) measured the scale morphology of bluegill sunfish (*Lepomis macrochirus*) with GelSight technology and speculated about the hydrodynamic function of the scales. Later, using the same technology the surface topography of various fish species was measured with and without the mucus layer (Wainwright et al., 2017). Some physical characteristics of scales from grass carp (*Ctenopharyngodon idellus*) were measured and manufactured as a bionic surface. An indication of drag reduction of about 3% was reported (Wu et al., 2018). They claimed a water-trapping mechanism to be responsible for this reduction, mainly due to flow separation behind the scales. No further details were given on the flow structure. In addition, the scales were not overlapping but treated as individual elements. The present paper aims to reproduce the fish surface more realistic based on statistics of scale measurements and reproduction of the overlapping scale array along the body. We focus our studies on the European Bass (*Dicentrarchus labrax*), which is a fish commonly found in Mediterranean, North African and North Atlantic coastal water regions. The fish scale pattern and array overlap are almost homogeneous over the length of the body.

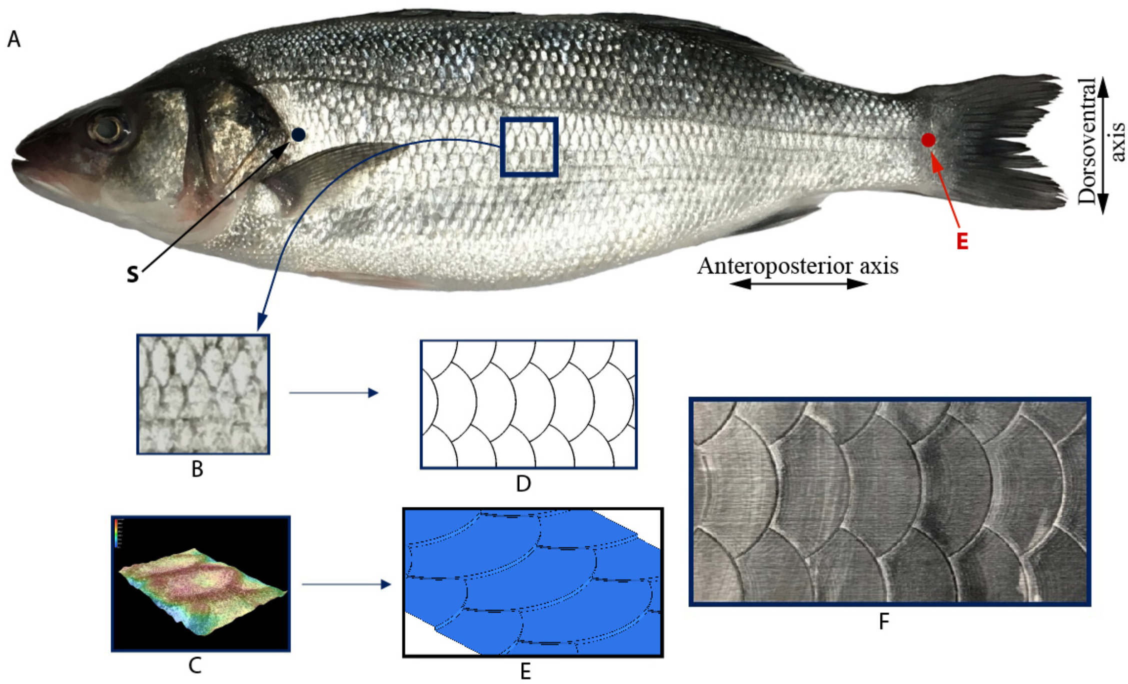

Figure 2.1: **Microscope images and CAD replication of Sea bass fish scales** (A) Picture of a Sea bass. Point S and E show the regions where measurements were taken. (B) Top view of the scales. (C) Topographical view from scanning with the Digital Microscope. (D) Top view of replicated CAD model. (E) Isometric view of CAD model (F) Photograph of 3-D printed model from top.

2.2 Materials and Methods

2.2.1 Fish Samples

European bass (*Dicentrarchus labrax*) was collected from a local fishmonger (Moxon's Fishmonger, Islington, London). Five individuals of both sexes (total length of ≥ 33 cm) were used for the experiments. Sampling occurred from the pectoral region to the caudal region at ten equally spaced intervals between point S and E as shown in Fig. 2.1A. The skin of the fish was cleaned repeatedly with a 70% ethanol solution to remove the mucus layer. Immediately after cleaning, scale samples were removed from the skin and placed on object slides. Samples were analysed with a digital microscope (VHX-700FE series, Keyence) using the 3D mapping feature of the built-in software. This allowed to scan the 3D contour and to store the coordinates for later replication of the scale surface in Computer Aided Design (CAD) software. The 2D images and the 3D topographical scan from the microscope, the replicated CAD design and the 3D printed surface of fish scale array are shown in Fig. 2.1B-F. The physical model was scaled 10 times larger than the actual size, a practical scale for experimental studies in the flow channel (Panton, 2013). Experiments with up or down-scaled models are a common strategy in hydrodynamic and aerodynamic research based on the boundary-layer scaling laws explained in Appendix-2.

2.2.2 Computational Methodology

The computational domain and the boundary conditions are shown in Fig. 2.2A. For comparison with the experiments, the length-scale of reference herein is the same as for the 10-times up-scaled physical model. The dimension in 'x' (anteroposterior axis), 'y' (dorsoventral axis) and 'z' (lateral axis) directions are 250mm, 200mm and 80mm. The array of scales is designed with 10 rows along 'x' direction and 5 rows in the 'y' direction. The scale height from the base varies both in 'x' and 'y' direction. Hence, the height of the scale at a given position P(x,y) is defined as $h(P)$, whereas the maximum height of the scale in the centreline (h_s) is about 1mm, which corresponds to a 10-times enlarged value compared to the measured value of 100 microns. At the inlet to the domain, a laminar Blasius-type boundary layer velocity profile with a boundary-layer thickness (δ) of 10mm was imposed. This profile can be approximated according to Pohlhausen (Panton, 2013) as a second order polynomial profile given by the Eqn.3.1.

$$\frac{u(y)}{U_\infty} = A(\frac{y}{\delta}) + B(\frac{y}{\delta})^2 \tag{2.1}$$

$$\delta(x) = \frac{5 \cdot x}{\sqrt{Re_x}} \tag{2.2}$$

$$Re_x = \frac{\rho \cdot U_\infty \cdot x}{\mu} \tag{2.3}$$

where A and B are the coefficients based on the free stream velocity ($U_\infty = 0.1ms^{-1}$) and the boundary-layer thickness (δ = 10mm) at the inlet (A = 2, B = -1). The boundary-layer thickness given by Eqn.3.2 corresponds to a flat plate Reynolds number of about $Re_{xo} = 33000$ with an imaginary inlet length of $x_o = 333$mm from the leading edge of a flat plate until it reaches the inlet of the domain, where the Reynolds number (Re_x) is defined by Eqn.3.3. Except for the floor and the fish scale array, all the other side walls were specified with free slip conditions, i.e. zero wall-shear. The domain was meshed with 18 million tetrahedral elements with 10 prism layers near the wall with a first cell value of 0.06mm. To study the effect of scale height relative to boundary-layer thickness on total drag, different boundary-layer thickness at the entrance were simulated. Therefore, the inlet domain was extended for 200mm upstream as shown in Fig. 2.2B and different boundary-layer thicknesses at the new inlet was specified as 5,10 and 15mm. The problem was solved using the steady state pressure based laminar solver in ANSYS Fluent 19.0 with a second-order upwind method for momentum equation. Water was used as the continuum fluid in this Computational Fluid Dynamics (CFD) study with a density (ρ) of 1000 kgm^{-3} and a dynamic viscosity (μ) of 0.001 $kgm^{-1}s^{-1}$.

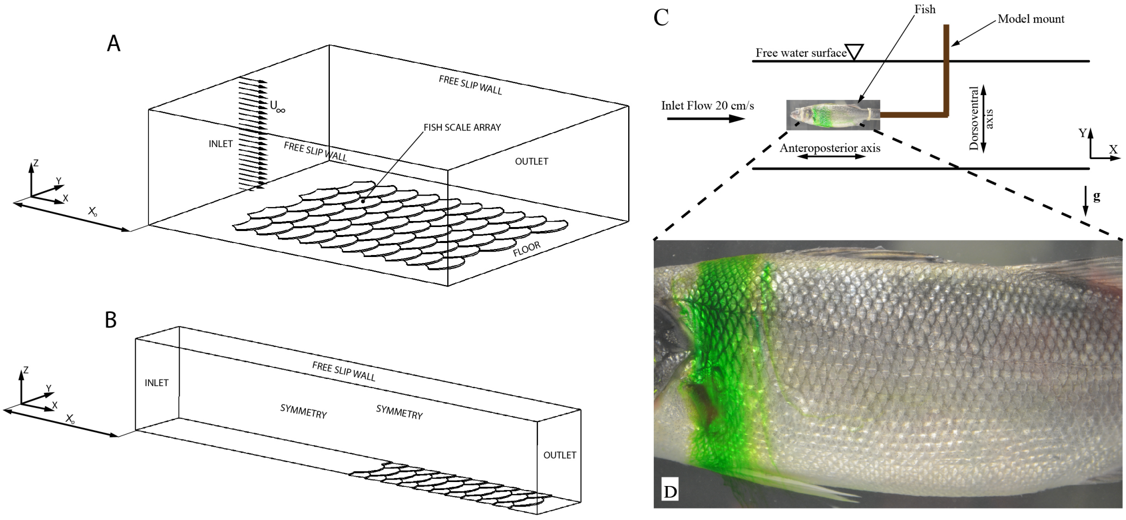

Figure 2.2: **Computational domain and Experimental set-up** (A) Configuration of the fish-scale array in CFD similar to the condition of the physical model of the scale array at the bottom wall of the wind tunnel. Note that the velocity vector represents the inlet profile with free-stream velocity parallel to the 'x' axis in positive direction (Anteroposterior direction). 'y' axis represents the spanwise (Dorsoventral direction) and 'z' axis represents wall normal direction. (B) CFD domain with symmetry conditions to simulate the drag variation with no end effects. In both the figures 'x_o' is the imaginary length from the leading edge of the plate to the inlet of the domain. (C) Schematic diagram of the experimental set-up. (D) Dye coating on the surface of the fish.

2.2.3 Surface Flow Visualisation on Biomimetic Fish Scale Array

The fish scale array with dimensions explained in the previous section was 3D printed with ABS plastic using Fused Deposition Modeling (FDM)(Printing machine - Raise 3D). For manufacturing, the base layer thickness needed to be 4mm to ensure stable handling. The model was placed on the floor of a wind tunnel (PARK Research Centre, Coimbatore, India) in the test section (cross-section of 450mm and 600mm width). To reduce the disturbance of the step at the leading edge, a chamfered flat plate (size 250mm x 200mm x 4mm) was placed upstream and downstream such that the region with the scale array is flush with the wall. Surface oil-flow visualisation was performed with a mixture of Titanium-di-oxide, kerosene and a drop of soap oil added to it to avoid the clustering of particles. For more details of this visualization see (Merzkirch, 2012). Before starting the wind tunnel, the model was painted with the mixture in the region downstream to the scale array. Thereafter, the tunnel flow was started to a free-stream velocity of $12ms^{-1}$ which gave a boundary-layer thickness of about 10mm at the entrance to the scales. Wind transports the dye according to the local wall shear. A camera mounted on the top of the tunnel is capturing this process.

2.2.4 Surface Flow Visualisation on Real Fish Skin

Flow visualisation experiments on real fish (lifeless) were conducted in a return type open surface water tunnel at City, University of London. The test section is 40 cm wide x 50 cm depth x 120 cm in length and transparent in all the sides to provide an optical access for flow studies. Inlet flow velocity was set at 20 cm/sec. Sea bass (Dicentrarchus labrax) of length (L $\approx$ 340mm) and common carp (Cyprinus carpio) of length (L $\approx$ 320mm) were used in this study. The fish was mounted on a 'L' shaped string at the centre of the water tunnel from the base (see Fig. 2.2C). Synthetic food colour was mixed with few drops of oil and coated on the surface of the body just downstream of the snout of the fish as shown in Fig. 2.2D. The ratio between the viscosity of the water and the oil lies in the range discussed by Squire (Squire, 1961), hence the effect of the oil flow on the flow dynamics is very small. The motion of the oil-mixture was captured with a high speed camera which was mounted outside the water tunnel.

2.3 Results

Flow data obtained from the CFD results are first presented as velocity fields and profiles. Figure. 2.3A shows colour-coded contours of constant streamwise velocity

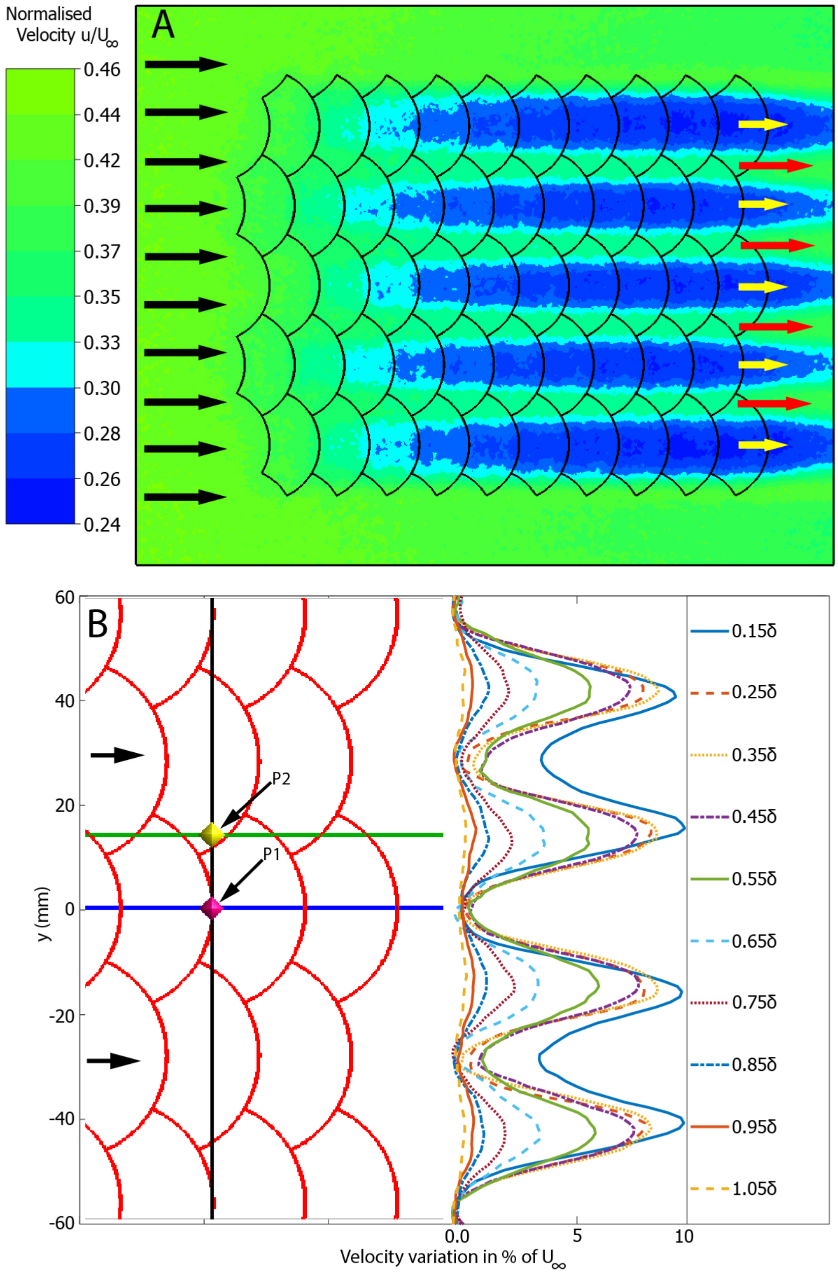

Figure 2.3: **Velocity contour and velocity profiles** (A) Normalised Velocity Contour at a wall-parallel plane at a distance of z = 0.25δ from the surface. Arrows indicate flow direction. Note that the black arrows at the inlet are uniform in length, while red and yellow arrows at the outlet differ in length. (B) Velocity variation in spanwise direction at various wall-normal distances in the boundary layer. Scale array is shown in red color for better illustration. **Blue line (Line-1)** represents a centreline of a row of scales. **Green line (Line-2)** represents the overlap region between the scales. Black line represents a location in the 'x' direction at 190mm from inlet. Location1 (P1) and Location2 (P2) are probe points at 190mm from inlet on centreline region and overlap region. Black arrow indicates mean flow direction

(normalised with the free-stream velocity) in a wall-parallel plane at a distance of 0.25δ. At the inlet, the velocity is uniform along the spanwise direction ('y' direction), whereas, along the flow direction over the scales, there is a periodic velocity variation in spanwise direction. Low-velocity regions have emerged in direction of the centrelines of the scales, which is indicated with yellow arrows. In comparison, high-velocity regions (Red Arrow regions) are seen along the regions where the scales overlap each other. These high velocity and low-velocity regions are referred in the following as streaks. These structures are linked in number, location and size with the overlap regions along the dorsoventral axis over the surface.

Further information of the variation of the velocity in the streaks is demonstrated in Fig. 2.3B. It shows spanwise profiles of the streamwise velocity at the location $x = x_o + 190mm$ (8^{th} scale in the row along streamwise direction from the inlet) for different wall normal locations. At a wall normal location of 0.15δ the velocity variation is around 10% of U_∞ between the peak (local max) and valley (local min) in the profile. Given this difference, the streak amplitude is calculated using the Eqn.3.4 from (Siconolfi et al., 2015).

$$A_{ST} = \left[\max_{y}\{U(X,y,z)\} - \min_{y}\{U(X,y,z)\} \right] \Big/ (2U_\infty) \tag{2.4}$$

As seen from the different profiles, the location of peaks and valleys do not change with wall normal position, therefore the streaks extend over most of the boundary-layer thickness in a coherent way. The streak amplitude A_{ST} is plotted along the wall normal location in Fig. 2.4 and it can be seen that the streak amplitude is maximum within the first 20% of the boundary-layer thickness with a value of 4.5% of U_∞. As the distance from the wall increases, the streak amplitude decreases monotonically until the displacement effect of the scales has died out at the outer edge of the boundary layer (1.05δ from the wall).

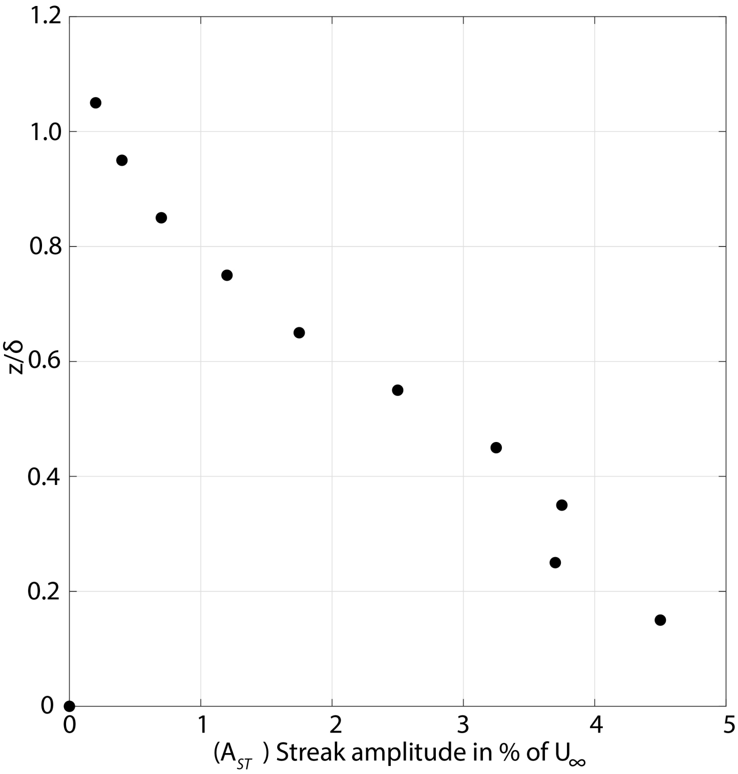

Figure 2.4: **Variation of streak amplitude along wall-normal direction for model fish scales.** Measurements were made 190 mm from water inlet (along black line shown in Fig. 2.3b

Experimental flow visualisation pictures of the streaks behind the fish scale array are shown in Fig. 2.5A. As the particle mixture coated on the surface moves according to the direction and the magnitude of wall-shear, the mixture moves farther in the regions of high shear, than in regions of low shear. Therefore, the flow produces streaky patterns on the surface with different length downstream of the scale array (Fig. 2.5A). The red lines depict the orientation of the streaks relative to the pattern of the scale array. It is clearly seen that the high-speed streaks are formed in the overlap regions as claimed from the CFD results. For better comparison with the CFD results, the surface flow visualisation over the scale array is overlaid with surface streamlines from CFD (see Fig. 2.5B), which is discussed later. Figure. 2.5C shows the result from the surface flow visualisation experiment on sea bass

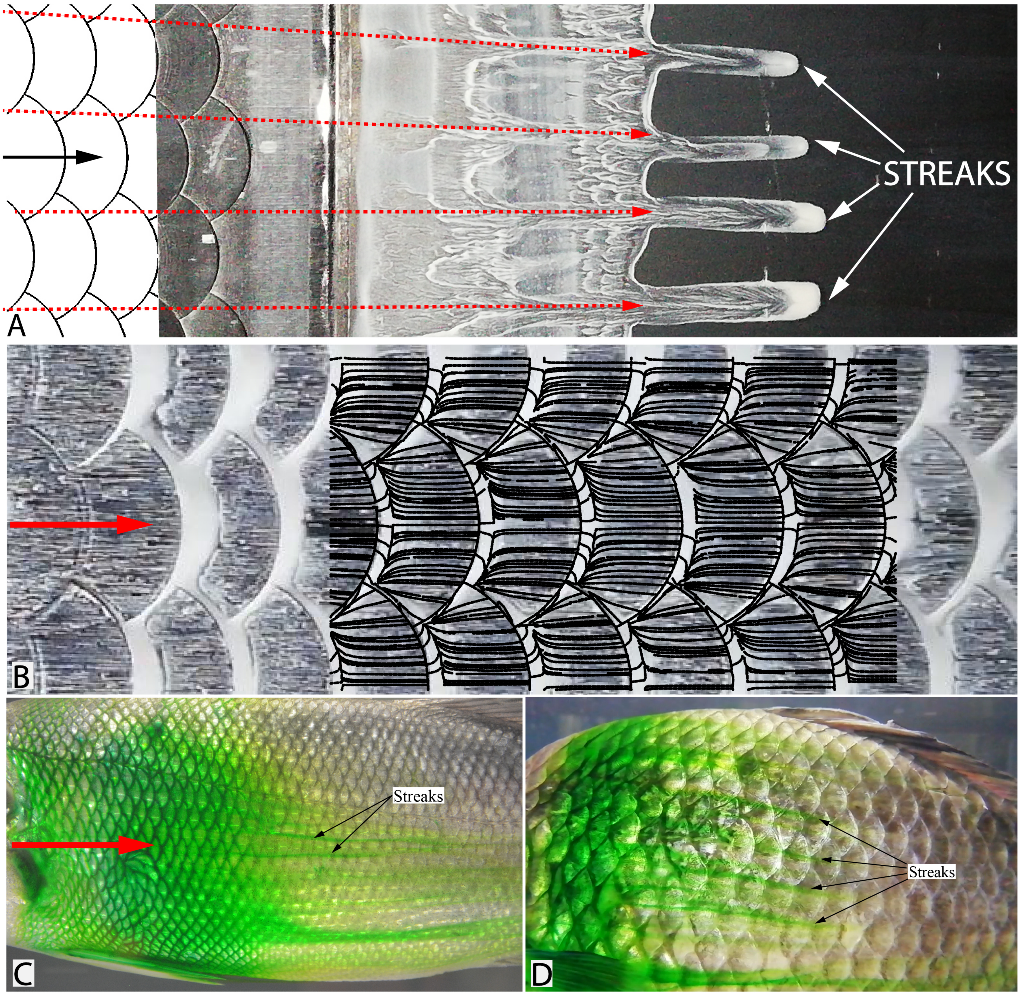

Figure 2.5: **Surface flow visualisation on the scales.** (A) Black arrow represents mean flow direction. Note that the oil-mixture was painted in the region downstream of the scales to highlight the generation of the streaks. 2-D top view of the CAD model is merged to get the impression of the arrangement of the scales. The red arrows were added to illustrate the trace of the streaks relative to the arrangement of the scales. (B)Red arrow represents the mean flow direction. Herein, the oil-mixture was painted directly onto the scales. Surface streamlines from CFD simulation are overlaid to compare the results. Note that the regions of accumulated oil-patches match with the regions of flow reversals from CFD simulation. (C and D) Oil-flow visualisation on sea bass (*Dicentrarchus labrax*) and common carp (*Cyprinus carpio*).

(Dicentrarchus labrax). It is evident that two clear streaks are seen on the surface where the scales overlap each other. The same experiment was repeated with the common carp (Cyprinus carpio) which has a larger scale size but with a similar overlap pattern when compared with sea bass. In this case four streaks are clearly visible along the overlap region of the scales as shown in Fig. 2.5D. Hence the number of overlap regions defines the number of streaks produced on the surface of the fish. The results from the biomimetic scale array is in excellent agreement with the flow over real fish surface.

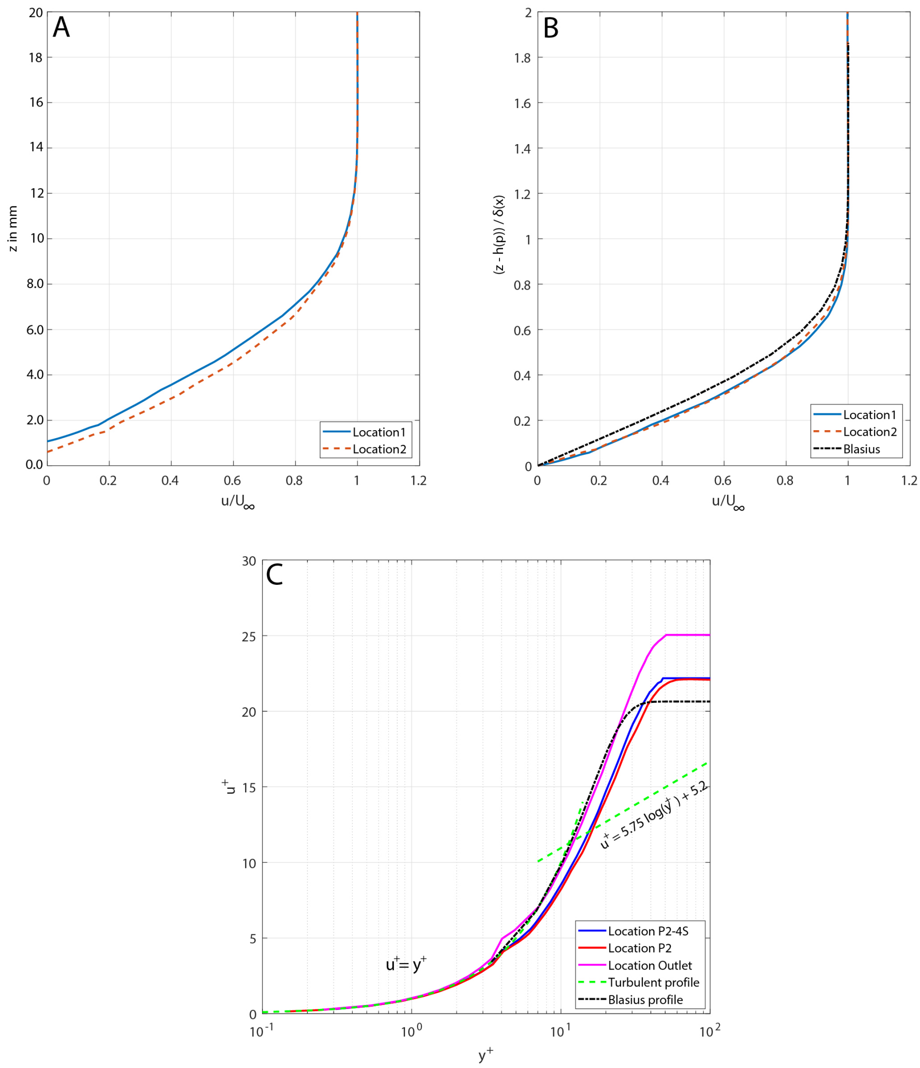

Figure 2.6: **Boundary layer profiles at Location 1 and Location 2 (probe points P1 and P2 in Fig. 2.3B).** (A)Normalised velocity profiles in the absolute coordinate system. Note that the shift in velocity profiles along 'z' direction is because of the change in scale height h(P) for the different probe points P (B)Normalised velocity in the body coordinate system with Blasius laminar boundary layer profile along a smooth flat plate. (C) Dimensionless velocity profile at three locations: Location P2, four scales upstream from Location P2 (P2-4S) and at outlet.

Figure. 2.6 shows the variation of the normalised velocity profile at two locations along the span at the 8^{th} scale row (probe point location P1 and location P2 , compare Fig. 2.3B). In the absolute coordinate system (Fig. 2.6A) there is a shift in 'z' direction because of the variation in the scale height h(P) along the span of the surface. When the profiles are plotted in the body relative system ($z = z - h(P)$) the difference along the wall normal direction (Fig. 2.6B) becomes more obvious. With the scales on the surface, the gradient of the velocity near the wall gets steeper in the location discussed here (at the probe points P1 and P2). This is concluded from the comparison to the Blasius velocity profile for a smooth flat plate (dashed black line). However, the boundary-layer thickness is approximately the same. Figure. 2.6C shows the variation of the dimensionless velocity profile at three locations: at Location P2, four scales upstream from Location P2 (Location P2-4S) and at the outlet of the computational domain. Dimensionless velocity u^+ is defined by $u^+ = u/u_\tau$ where, frictional velocity at the wall $u_\tau = \sqrt{(\tau_w/\rho)}$ and wall coordinate y^+ is defined by $\rho u_\tau y/u_\tau$. It is evident that at all three locations the profile is similar to the reference Blasius profile (dotted red line) suggesting that at all locations the velocity variation is laminar. This suggests that scales change the profile shape inside the boundary layer region but do not change the boundary-layer thickness (nevertheless affecting the displacement and momentum thickness). The flat plate velocity profile for the turbulent case with log-law is shown for comparison.

The surface streamline picture generated from the CFD results is shown in Fig. 2.7A. In the centreline of the scales, the flow mostly follows the direction of the main flow. Section X-X is enlarged and the cross-sectional flow in the centre of the scales is shown in Fig. 2.7B. It is seen that the flow follows the small slope caused by the tilt angle of the scale until it separates from the sharp edge on the scales and reattaches further downstream at approximately 2.5 times the scale height (h_s) on

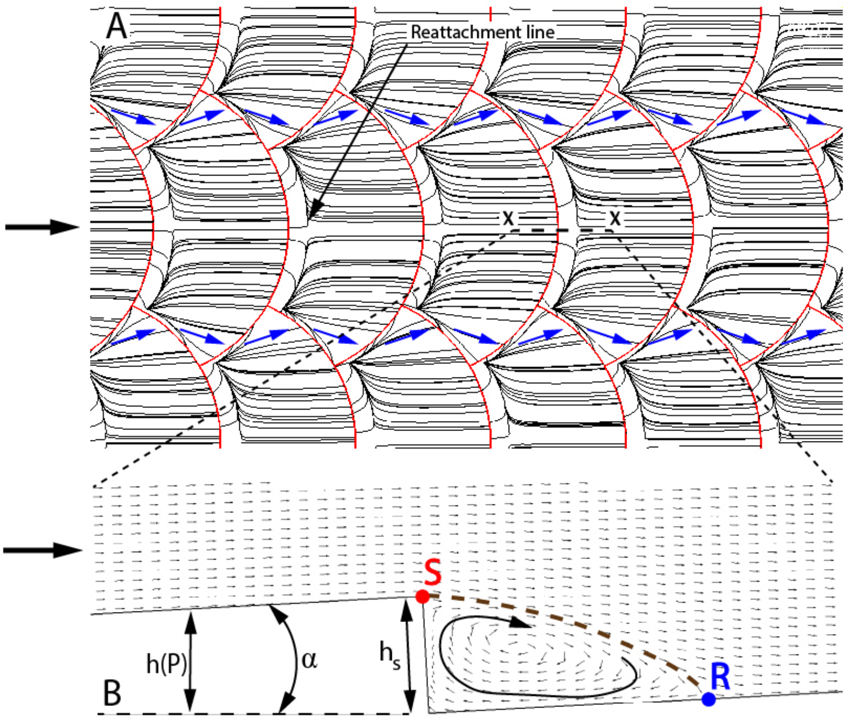

Figure 2.7: **Surface streamline and vector plots from CFD simulation.** (A)Top view of surface streamline over the scales. Note the zig-zag motion along the overlap region compared to the parallel flow at the central regions of the scales. (B)Vector field in the x-z cross sectional plane along the central region of the scale at line X-X (vectors indicate only direction and not magnitude). $h_s = 1mm$ and $\alpha = 3$ degrees. S and R represents the separation and reattachment of the flow streamlines. Thick dashed line indicates the region of recirculating flow with an arrow indicating the direction of rotation. In both drawings the black arrow indicates the mean flow direction.

the surface as a laminar boundary layer. This non-dimensional reattachment length is very similar to the value reported in horizontal backward facing step flows if the Reynolds number defined with the step height and free stream velocity is around 100 for the given flow situation(Goldstein et al., 1970). This separated flow region behind the step is visible from the dividing streamline (shown as thick dotted line in Fig. 2.7B). Also, from the surface flow visualisation, the separated flow region behind the edge of the scales can be observed by the white patches due to the accumulation of the particles (see Fig. 2.5B). These white-patched regions match in size and locations with the flow reversal zones in the CFD. When the fluid moves along

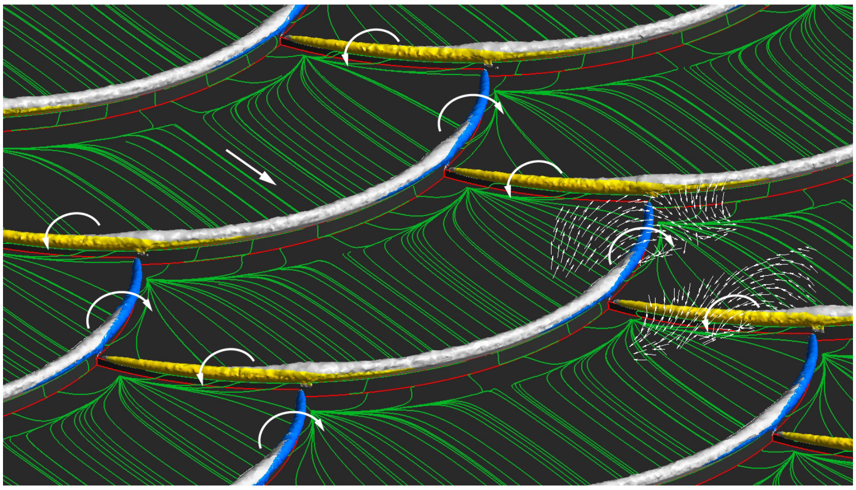

Figure 2.8: **Surface streamline plot with direction of vortices.** Vector plots at the overlap region for two consecutive scale rows. Helicity coloured in yellow for positive (Vortex direction CCW) and blue for negative (Vortex direction CW). Other rotational vectors are based on the colouring of vortices. Vortices are identified with 'Q' criterion. White straight arrow represents the mean flow direction.

the scales, the streamwise component of velocity is reduced in the central region of the scale by the large separated zone as explained above. This causes a spanwise pressure gradient and forces the fluid to move from the central region of the scales to the overlapping region. This movement is seen in the zig-zag pattern (shown in blue arrows in Fig. 2.7A) with larger spanwise components of fluid motion. The spanwise flow towards the overlapping region produces a higher streamwise velocity because of mass conservation. This causes high-speed streaks in these regions. In addition, it is evident that the flow reversal is reduced compared to the cross-section at the central region of the scales. This is the root cause of producing low speed and high-speed streaks.

Figure. 2.8 shows the surface streamlines on the scale array along with cores of intense vortices visualised by isosurfaces of the 'Q' value (Jeong and Hussain, 1995). The colours of the isosurfaces indicate the streamwise helicity which is defined as $(U_x.\omega_x)$, where, ω_x is the vorticity component along 'x' direction. The yellow colour region defines the region in which the vortex direction is Counter Clockwise (CCW) with respect to the 'x' axis direction (i.e. mean flow direction represented by a white straight arrow in Fig. 2.8.), similarly, the blue colour region defines the vortex direction in Clockwise (CW). It also displays the cross-flow velocity fields on planes parallel to the Y-Z plane near the scale overlap region for two consecutive scales. The vortex in the central region of the scales (i.e. white colour vortex core) reflects the reversed flow region behind the step. There the flow direction remains nearly aligned with the mean flow. In comparison, when the flow moves downstream in the overlap region it is affected by successive vortices with alternating direction switching from CCW to CW and vice versa. This causes the streamlines in the overlap region to generate a zig-zag pattern as already illustrated in Fig. 2.7A.

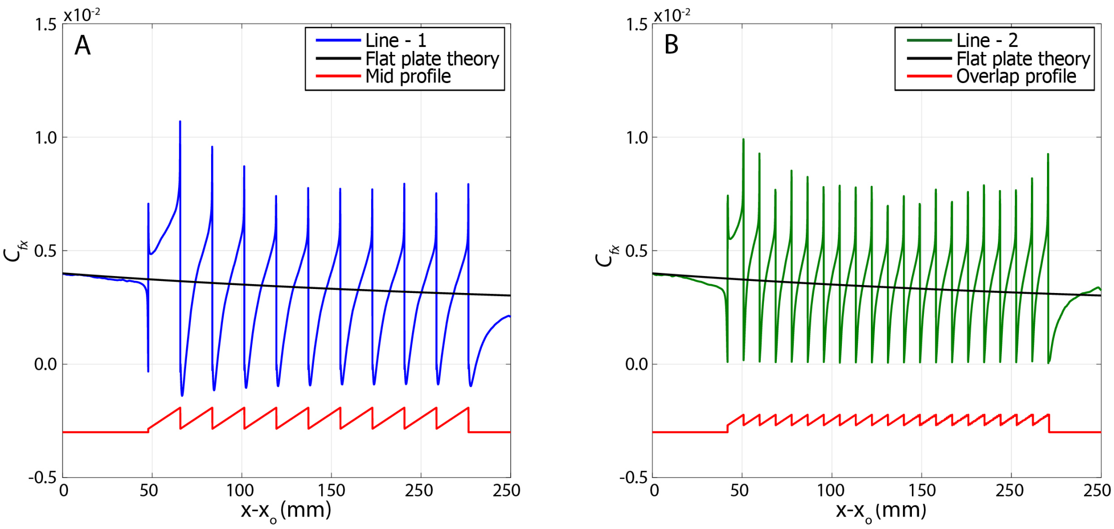

Figure 2.9: **Variation of skin friction coefficient** (C_{fx}) **along 'x' direction at two locations.** (A)Blue line represents the C_{fx} variation along **(Line-1)** (refer **Blue line** in Fig. 2.3B) (B)Green line represents the C_{fx} variation along **(Line-2)** (refer **Green line** in Fig. 2.3B). Red lines represents variaion of 'z' coordinate in 'x' direction along corresponding locations (not to scale). Black line represents the variation of $C_{fx\,theory}$ for flat plate boundary layer by Eqn.2.5. x_o (333mm) is the imaginary length before the inlet of the domain.

2.3.1 Skin Friction and Total Drag

As previously mentioned, the scales modulate the near wall flow with streaks which will change the wall shear stress (τ_w) distribution on the surface when compared with flow over smooth flat plate. To analyse this effect, skin friction coefficient C_{fx} defined by Eqn.2.5 is plotted along the centreline (see **Blue line (Line-1)** in Fig. 2.3B) together with the surface profile variation in Fig. 2.9A. In addition, the figure shows the profile of the theoretical skin friction coefficient ($C_{fx\,theory}$) for a smooth flat plate case, given in Eqn.2.6. Along the initial smooth part of the surface until 25mm the skin friction coefficient follows the theoretical skin friction coefficient $C_{fx\,theory}$. As it enters the scale region, initially the skin friction drops because of the adverse pressure gradient caused by the first wedge. Over the scale, it increases again because of the local acceleration until it reaches the maximum at the edge of the scale. Then, C_{fx} drops to a negative value because of the recirculation region explained in Fig. 2.7b. Once the flow reattaches, the skin friction gets positive again and increases until it reaches the peak as it approaches the edge of the next scale. This process repeats itself in flow direction with the succession of scales. The same process happens in the overlap region, but here, for a single scale length, the process happens twice because of two small steps formed by the adjacent scales in the lateral overlap region (note the difference in the scale profile in the central region in Fig. 2.9A and the scale profile in the overlap region in Fig. 2.9B). Additionally, the streamwise wall shear does not reach negative values in the valleys as there is no flow reversal in these zones. The shear drag along the central region (determined by the integration of wall shear in the streamwise direction along **Blue line (Line-1)** in Fig. 2.3B) gives a 12% reduced value compared to the theoretical drag for a smooth flat plate. In contrast, the overlap region (determined by the integration of wall shear in the streamwise direction along **Green line (Line-2)** in Fig. 2.3B) gives a 5% increase in shear drag. This tendency along the span correlates with the low and high-velocity regions as the wall shear stress is directly proportional to the velocity gradient. The integral over the total surface leads to the total friction drag, which is a net effect of the streaks. As we introduce a surface which is not smooth, the total drag is the sum of the friction and the pressure drag. The latter depends on the wake deficit behind the step of the scale because of the separated flow regions. Both need to be taken into account from the CFD results to investigate the net effect on possible total drag reduction.

In order to investigate the relative contributions of friction and pressure drag over the skin, we varied the boundary-layer thickness (δ) relative to fish scale height (h_s) as reported in Table 2.1. The inlet boundary-layer thickness in the CFD domain was increased in steps from $\delta = 5mm$, 10mm and 15mm respectively with a free stream velocity (U_∞) value of $0.1ms^{-1}$. Drag coefficients were calculated using the drag force values obtained from CFD. The change in friction drag and total drag coefficients is given in Eqn.2.7. The theoretical drag coefficient ($C_{d\,theory}$) is calculated by integrating the skin friction coefficient ($C_{fx\,theory}$) along the 'x' direction.

$$C_{fx} = \frac{\tau_w}{0.5 \cdot \rho \cdot U_\infty^2} \tag{2.5}$$

$$C_{fx\,theory} = \frac{0.73}{\sqrt{Re_x}} \tag{2.6}$$

$$\Delta C_{df}(\%) = \frac{(C_{df} - C_{d\,theory})}{C_{d\,theory}} \times 100 \qquad \Delta C_{d\,tot}(\%) = \frac{(C_{d\,tot} - C_{d\,theory})}{C_{d\,theory}} \times 100 \tag{2.7}$$

δ/h_s	C_{dp}	C_{df}	$C_{d\,tot}$	$C_{d\,theory}$	$\Delta C_{df}(\%)$	$\Delta C_{d\,tot}(\%)$
5	0.000277	0.00448	0.00476	0.00453	-1.03	5.08
10	0.000193	0.00301	0.00320	0.00316	-4.68	1.43
15	0.000129	0.00214	0.00226	0.00236	-9.31	-3.84

Table 2.1: Dependence of drag force with boundary-layer thickness to fish scale height ratio

For all the three cases the change in friction drag ($\Delta C_{df}(\%)$) relative to the smooth flat plate is negative indicating that the scales are efficient in reducing skin friction. This effect increases with increasing boundary-layer thickness to scale height ratio. However, the total drag is only reduced for the third case ($\Delta C_{d\,tot} = -3.84\%$) when δ/h_s ratio is 15. This is the typical ratio between the boundary-layer thickness and the scale height in cruising conditions of the flow around the fish and will be explained in the discussion.

2.4 Discussion

In this paper, 3D microscopic measurements of the scales on the European bass fish are presented. Based on the data statistics, a biomimetic scale array was replicated with the use of Computer Aided Design and 3D printing. The study differs from previous ones on biomimetic scales (Dou et al., 2012; Wainwright et al., 2017; Wainwright and Lauder, 2017) that it is the first for European bass and the first using a typical 3D curvature of the scales with an additional overlap pattern. Flow over the scale array was analysed using Computational Fluid Dynamics and experimental results were obtained from the surface flow visualisation. Excellent qualitative agreement was found, showing the formation of alternating high-speed and low-speed streaks along the span, which concludes that the location, size and arrangement of the streaks are linked with the overlap pattern of the scales. The experimentally validated CFD data further allows drawing conclusions about the total drag of the surface, which is relatively difficult to obtain. The derived drag values show that the overlapping scale arrays are able to reduce the body drag if their characteristic step height is sufficiently small (at least one order of magnitude) compared to the local boundary-layer thickness. If this conclusion holds for typical flow conditions and size of the scale for European bass, the consequence would be a reduction of total drag, hence costing less energy to the fish in cruising. In the following, we discuss the possible relevance of this finding to the situation of sea bass in steady swimming conditions, including a critical review of the limitations of the study.

2.4.1 Mucus layer and transport

- Any mucus on the scales needed to be washed away for optical reasons before the scales could be measured in the microscopy. It is known for similar fish species that the mucus only covers the microstructures of the scales such as circulae and the ridges which connect the ctenii, therefore the overall shape of the scales is not affected by the wash-out procedure (see also the conclusion by (Wainwright et al., 2017)). Additionally, from Rosen-Cornford hypothesis, the mucus layer is reluctant to lower friction (laminar boundary layer) and could be broken and mixed at the aft portion of the fish where turbulence could set-in (Rosen and Cornford, 1971). Thus the flow dynamics is representative for the natural situation of the scales in the flow and our assumption holds in the areas where laminar boundary layers prevail during swimming.
- The observed recirculating flow near the central region of the scales might be helpful in retaining the mucus and reducing the mucus secretion rate if the mucus layer breaks from the surface. This inference is supported from the fact that in the surface flow visualisation experiments the mixture was largely trapped in these regions. This is comparable with the results on flow over grass carp fish scales (Wu et al., 2018).

2.4.2 Swimming speed and Reynolds number

- The swimming speed of European bass is proportional to its body length (Carbonara et al., 2006). For the fishes considered in this study, the swimming speed lies in the range from $1.2ms^{-1}$ and $1.4ms^{-1}$ corresponding to a Reynolds number (calculated with the full body length L) in the range between 4×10^5

and 6×10^5. This is in classical fluid dynamics when transition from laminar to turbulent boundary layer flow sets in. As the reference length is the tail end, we can conclude that the boundary layer over the sea bass for most of the body length remains laminar. Direct measurements of the boundary layer on sea bass are not known so far, however, such data exist for comparable fish such as a scup (*Stenotomus chrysops*), a carangiform swimmer, and rainbow trouts (*Oncorhynchus mykiss*). Scup have mostly an attached laminar boundary layer over its body for most of the time and incipient separation appears only for short time intervals in the swimming cycle (Anderson et al., 2001). PIV analysis on swimming rainbow trout at a Reynolds number of 4×10^5 revealed a laminar boundary layer with transition to turbulence in the caudal region (Yanase and Saarenrinne, 2015). Hence, the laminar CFD analysis performed in this study is representative for the effect of fish scales on typical European bass.

- For the total drag of the biomimetic surface, a drag reduction was only observed when the scale step-height was sufficiently small relative to the local boundary-layer thickness (one order of magnitude). At a swimming speed of $1.2ms^{-1}$ and for a fish length of 300mm the boundary-layer thickness will be about 1.5mm at the mid of the fish body (from Eqn.3.2) measured from the snout of the fish to the begin of the caudal fin (see Appendix-3 for the boundary-layer thickness on approximated fish body). In this region, the scale height measured from the microscope was about 0.1mm which gives a boundary-layer thickness to scale height ratio (δ/h_s) of 15 and has proven reduction in drag. Interestingly, the boundary-layer thickness of scup is also in the same range discussed here. Hence, the study shows, at least for steady swimming conditions, valid implications on total drag reduction due to the presence of overlapping scale arrays. The present work is focused only on the fishes with teleost integument as mentioned in the introduction. The drag reduction discussed in this paper relates on laminar boundary layers. For turbulent boundary layers, the scales from the cartilaginous fishes are known to reduce turbulent drag (Dean and Bhushan, 2010), which is based on another physcial mechanism. Although those swimmers are typically larger and performing at much higher Reynolds number, the scale thickness is still within 1 to 5% of the turbulent boundary-layer thickness (Afroz et al., 2016). Therefore, the optimum scale thickness (relative to the boundary-layer thickness) is not different from our findings.

- The size of the fish scale changes linearly with the body length from Lee's equation (El-Nasr, 2017), similarly, the critical swimming speed also increases with length (Carbonara et al., 2006). Hence, the boundary-layer thickness to scale height ratio (δ/h_s) remains approximately constant throughout the growing phase. For a constant bodylength of two species such as tuna and common carp, the swimming speed is higher for tuna and lower for common carp. Correspondingly, the boundary-layer thickness will be thinner for tuna and thicker for common carp. It would be the reason for tiny scales on tuna when compared with the bigger scales on common carp. However, a definite answer is only possible with more detailed study of several species.

2.4.3 Relevance of streaks in boundary-layer transition

- The fish scale pattern could be considered as distributed roughness placed on a smooth surface. Hence for this type of roughness elements, the roughness Reynolds number calculated from $Re_k = \rho u_k h_s/\mu$ is 20, where u_k is the undisturbed velocity at the maximum roughness height (i.e., scale height h_s). From various literature the critical roughness Reynolds number to induce bypass transition is around 250 (Doenhoff and Braslow, 1961), (Rizzetta and Visbal, 2007). Therefore, the roughness Reynolds number is more than one order below the critical value. Furthermore, the slope of the scale (α) is 3 degrees or 0.052 radians. From Singh and Lumley (Singh and Lumley, 1971) if the slope of the roughness element is far lesser than unity (i.e.,$\alpha << 1$) then the stability of the velocity profiles is increased because of the roughness. This leads to a fact that the fish scales act like micro roughness elements which are placed well inside the boundary layer to produce steady low and high-speed streaks without inducing bypass transition.

- Studies of the boundary layer flow over a flat plate have shown that placing arrays of micro-roughness elements on the plate can delay transition (Fransson and Talamelli, 2012; Siconolfi et al., 2015). The effect of those elements is that they produce low speed and high-speed streaks inside the laminar boundary layer, which delay the non-linear growth of the Tollmien-Schlichting waves (Fransson et al., 2004). Although the mechanisms to generate the streaky pattern might be different (lift-up mechanism of streamwise vortices versus alternating vortices in the overlap regions), the fish-scale array producing streaks could also lead to the delay in transition.

To summarize, the biomimetic fish scale array produces steady low and high-speed streaks, which are arranged in spanwise direction in the same pattern as the rows of the overlapping scales. Those regular arrangement of streaky structures are known from flow studies on generic boundary layer flows to stabilize the laminar steady state and delay transition to turbulence. As already mentioned, the Reynolds number of the fish considered here lies in the transitional range. Thus, we conclude that steady streaks similar as those observed for the biomimetic scale array are indeed produced by the scales of fish and help to maintain laminar flow over the fish body. The presented biomimetic surfaces can be engineered by purpose to reduce skin friction and delay transition in engineering application. However, this only refers to steady swimming conditions. Undulatory motion of the body during active propulsion plays an additional role in the boundary-layer transition. Experiments with undulatory moving silicone wall in flow show an alternating cycle between re-laminarization and transition in the trough and at the crest of the body wave (Kunze and Bruecker, 2011). As the fish surface can also undergo bending motion, the overlapping scales can move relative to each other and deploy in regions of strong curvature. From previous measurements of the boundary layer over swimming scup, it is known that the boundary layer remains laminar for most of the body without flow separation even in the adverse pressure gradient region (i.e. aft part of the fish) (Anderson et al., 2001). If the scales therefore also take part in any manipulation of flow separation is still an open question (Duriez et al., 2006). From a technological perspective, artificial surfaces with scales can even be built from flexible material, addressing also the issue of local flow separation.

2.5 Appendix

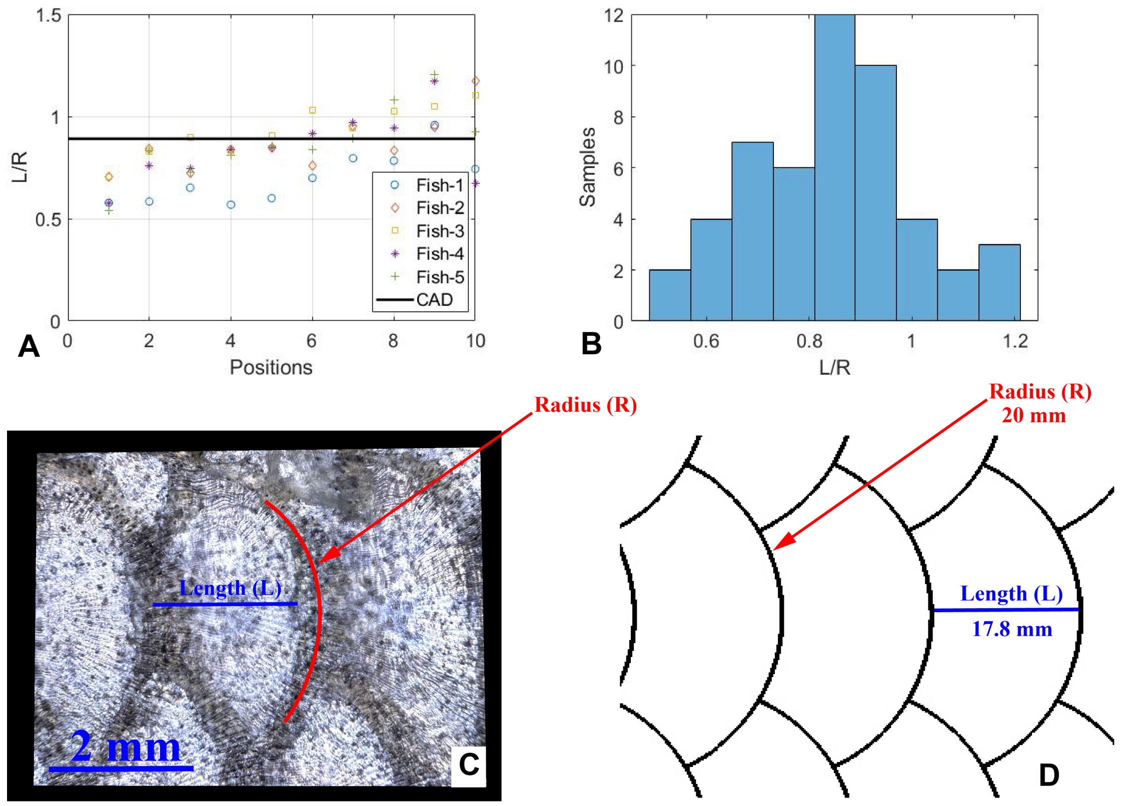

Figure 2.10: (A) Length to Radius ratio of European Sea bass (Dicentrarchus labrax) scales. (B) Histogram of the data (right) Note that the maximum occurrence is at a value of about 0.8 to 0.9. (C) Digital microscope from microscope showing the dimensions measured. (D) CAD model dimensions.

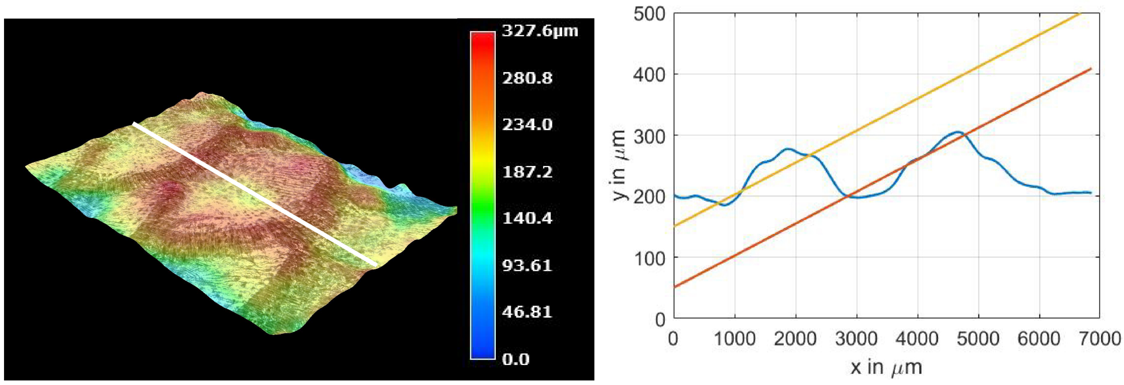

Figure 2.11: 3D topography obtained with a digital microscope. White colour line - Profile variation was measured (left). Profile height along the centreline of the fish scale. The lines indicate the average tilt of scales from the horizontal axis (Approximately 3 degrees) (right).

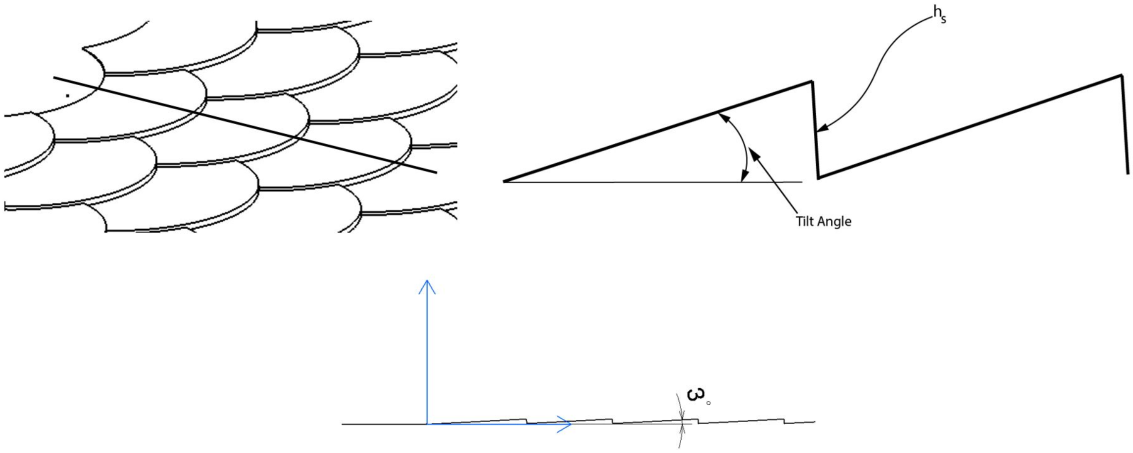

Figure 2.12: 3D view from CAD model (Left). Tilt angle of scale from horizontal axis and scale height h_s (Not to scale)(Right). Actual tilt angle of the scale (3 degrees) shown in bottom.

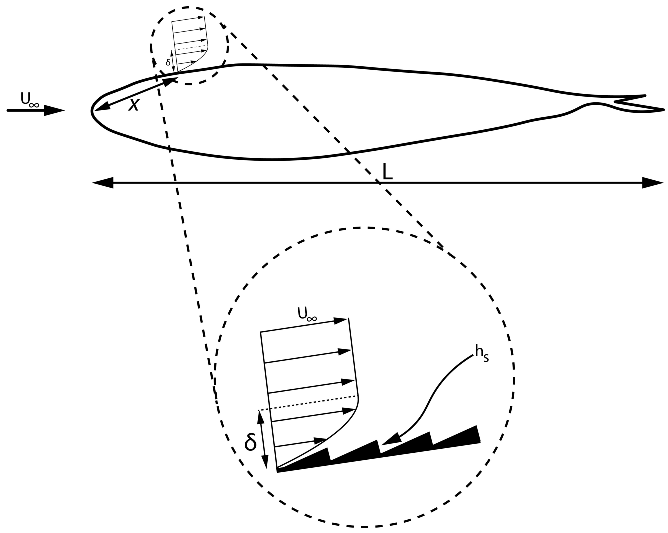

Figure 2.13: Boundary layer on swimming fish. Enlarged picture shows the boundary layer and scale cross section (Not to scale).

Consider a fish of length (L) swimming at velocity (U_∞). In relative frame of reference it is equivalent that a free stream fluid with a velocity (U_∞) flows over the fish body as shown in Fig. S4. Due to the viscosity of the flowing liquid and the no slip condition on the fish surface a boundary layer develops over the fish skin. Fish of about 300mm length were considered in this study with a critical swimming speed around 1 m/s. Water with density (ρ) of 1000 kg/m^3 and viscosity (μ) 0.001 kg/ms is considered as the continuum fluid. At a distance of 'x' from the snout of the fish the boundary-layer thickness (δ) is calculated from the Blasius boundary-layer thickness calculated from (Schlichting and Gersten, 2017):

It should be noted here that this equation will not provide the actual boundary-layer thickness and it will give only the order of magnitude of the boundary-layer thickness. Hence, at a distance of 40 to 100mm the boundary-layer thickness (δ) is in the order of 1mm. The scale with height (h_s) in the order of 0.1mm (100 microns) when measured from the microscope. The Reynolds number based on the boundary-layer thickness given by Eqn.2 is 100.

Additionally, the ratio of the boundary-layer thickness to the scale thickness (δ/h_s) is 10. In order to study the flow in detail, the scales were scaled-up by a factor of 10 and geometric similarity is maintained since the scaling is constant in all the directions. To maintain the Reynolds number based on the boundary-layer thickness at a value of 100 the velocity is fixed at 0.1 m/s without changing the fluid properties. So, kinematic similarity is maintained in fixing the Reynolds number and the results from this study is completely comparable with the actual flow field.

2.6 Critical Analysis

The computational and experimental study revealed that the biomimetic fish scale array produces a streaky base flow, which was also proven to exist on the real skin of two fish species. In this section some responses are given for the comments and suggestions from the reviewers.

Claim-1 *What are the limitations of using the digital microscope to acquire the fish scale geometry and how accurate was the modelling of the biomimetic fish scales with the actual fish scale shape?*

Firstly, the accuracy of modelling the fish scales largely depends on the accuracy of the experimental handling procedure of the fish and the instruments available for digitizing the scale geometry of the fish skin. This might be trivial as other researches done on shark skin showed possible ways to do so. However, the scales on bony fish species are different from the denticles on shark skin. From the literature, it is found that the denticles on shark skin are intact and do not change their shape even after several hours of slicing them from the shark body. Therefore, a small section of the shark skin can be cut out and placed under the microscope for geometrical studies. This method was first tried for the scales on bony fish species, however, it was not successful. As soon as a portion of the skin was taken out from the bony fish, the scales dried up very quickly and each scale became deformed to a great extent, in particular the distal end of the scales bent away from the body. Therefore, the fish needed to be directly recorded to obtain the scale images without slicing the skin. Secondly, with the mucus still on the fish skin, the scanning method using a microscope partly failed to reconstruct the surface topology due to intense reflections. Thus, it was essential to clean the mucus on the fish skin prior to the 3D scanning. Even then, the scales dried out after a few minutes because of the exposure from the intense illumination of the microscope. Some scanning attempts failed due to unknown reasons. In summary, a good quality scan required several trial and errors. The limitations of the microscope used in this study can be overcome by using a technology like Gelsight (Wainwright et al., 2017) in future studies, which was so far not available.

Furthermore, the topology measured using the microscope was simplified as a first-order geometrical approximation, based only on three essential parameters which are the length of the scale section which is exposed to the flow, the average radius of the scale and the average inclination. The other parameters like the curvature of the scales in other planes were not considered for this study. Most radically, the biomimetic scales had sharp edges and corners, whereas in real fish scale arrays the edges and corners are not sharp and are covered with mucus. Nevertheless, the existence of streaks on real fish skin and the alignment of streak pattern on the biomimetic skin showed us that the first-order approximation of the surface topology is a good representative to test the hydrodynamic function of the scales.

Claim-2 *The mucus coating was not considered in the analysis. What will change if we include the mucus coating?*

Modelling the presence of the mucus was discarded in the present thesis because of the following reasons: (i) The mucus thickness can largely vary along different positions on the scale surface, which is difficult to measure in real life situations, where wall-shear and locomotive action may cause further difficulties to precisely measure the surface topology. (ii) The mucus is a non-Newtonian fluid, which requires a multiphase fluid dynamics modelling, which was beyond the scope of the current work.

A possible role of the presence of mucus will be discussed here as a speculation based on our flow visualisation studies with the biomimetic scale array. We could observe that tracer particles stagnated just behind the central region of the scales in the region of the backward facing step. Hence, the mucus could also accumulate in that region, causing the smoothing of the step in the overlap region. Also, the stagnant mucus there could partly be washed away as a kind of surface bleeding in the overlapping regions of the scale array, which could further reduce the skin friction. Further, in-depth experimental work is needed to clarify any contribution of the mucus to the hypotheses given herein.

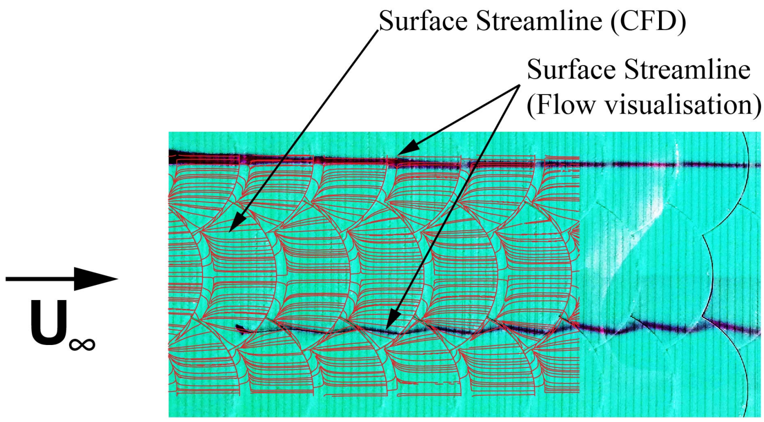

Figure 2.14: Surface flow visualisation pictures overlaid with CFD result.

Claim-3 *The zig-zag flow near the overlapping regions of the scale array was not clear in any of the flow visualisation pictures.*

Surface flow visualization on a flat plate covered with biomimetic scales in a laminar water channel overlaid with surface streamlines from CFD simulation (streamlines from CFD in red colour, surface streamline from the visualisation in thick blue colour) at the University of Stuttgart is shown in Fig.2.14. The zig-zag pattern of the visualized streamlines in the overlap region are in good agreement to the simulation results. The method used for the flow visualization is further described in the next chapter.

Claims: *The following hypotheses were raised during the review process and were investigated in the follow-up publication introduced in Chapter-3.*

- Streak amplitude: How does the streak amplitude depend on the scale height and number of successive scale rows?
- Influence of pressure gradients: Does the scale array produce streaky flows even in flows with pressure gradients?
- Transition: Does the scale array possibly delay transition as known for other mechanisms of streak generation and transition delay (Fransson experiment)?
- Critical roughness: Is there a critical height at which the scale array will promote by-pass transition when tested experimentally?

Future work

The results reported in this study give just an indication of a new biomimetic solution to generate a streaky base flow with possible consequence on laminar-to-turbulent transition or separation flow control (see Chapter-3). There are several aspects which can be studied further on the mechanism of streak generation .

- More accurate measurements of the scale topology can be done using three dimensional Micro CT Imaging under high humidity environmental conditions. Contactless scanning is recommended here since, while in contact the force imposed on the scale surface could deform it to give inaccurate geometry. The more accurate reproduction of the skin topology might provide further details in the flow manipulation near the wall.
- Mucus properties of the fish species studied herein should be measured and considered in further studies. In addition, surface tension effects on the distribution of mucus along the scales should be studied. As an initial analysis, the biomimetic model with mucus can be approximated as a locally smoothed

surface topology without sharp edges and analysed with a single phase flow model.

- Swimming style and kinematics of the each fish species should be mapped and the scale surface should be measured by scanning for that particular swimming mode. In this way, the dynamics of individual scale surfaces can be compared with the pressure gradients which are generated during swimming.

.

Chapter 3

Transition Delay Using Biomimetic Fish Scale Arrays

Abstract

Aquatic animals have developed effective strategies to reduce their body drag over a long period of time. In this work, the influence of the scales of fish on the laminar-to-turbulent transition in the boundary layer is investigated. Arrays of biomimetic fish scales in typical overlapping arrangements are placed on a flat plate in a low-turbulence laminar water channel. Transition to turbulence is triggered by controlled excitation of a Tollmien-Schlichting (TS) wave. It was found that the TS wave can be attenuated with scales on the plate which generate streamwise streaks. As a consequence, the transition location was substantially delayed in the downstream direction by 55% with respect to the uncontrolled reference case. This corresponds to a theoretical drag reduction of about 27%. We thus hypothesize that fish scales can stabilize the laminar boundary layer and prevent it from early transition, reducing friction drag. This technique can possibly be used for bio-inspired surfaces as a laminar flow control means.

3.1 Introduction

Fish are one of the oldest evolutionary species contributing to more than half of the living vertebrates distributed almost evenly across seawater and freshwater regions of the world(Helfman et al., 2009)'(Berra, 2007). It comprises more than 33100 species and is larger than the sum of all other vertebrates, with the size range varying from a few millimetres to more than 10m. Of the 33100 species, more than 26000 belong to bony fish. Only 1000 species belong to cartilaginous fish, such as sharks, and just only 100 species belong to jawless fish (e.g. lamprey and hagfish)(Nelson, 2007). Fish are highly dynamic creatures that persistently travel in water to reproduce, feed on their prey, and evade from their predator(Stenum, 2018). As a result, much of the energy expended is largely for locomotion (against drag from skin friction and pressure drag) within the aquatic environment. This can be still water or turbulent water, which is often the case in river flows(Anderson et al., 2001), citepref8.

Fish have prodigious features for flow control over their bodies, adapted to the environment and living circumstances. The skin and appendages are essentially the main parts where the flow is most likely to be tweaked to meet the need. For example, sharks swim at speeds ranging from 0.3 to 0.9 body-length/sec, reaching Reynolds numbers(Schlichting and Gersten, 2017) more than a million, which makes the boundary layer turbulent over most of their body(Gazzola et al., 2014). The placoid scales (similar to a riblet shape) have been proven to reduce the turbulent skin friction drag(Dean and Bhushan, 2010). Most studies over a decade focused on this specific scale shape(Wen et al., 2014)'(Oeffner and Lauder, 2012). Similarly, pectoral flippers on humpback whales have leading-edge tubercles that prevent stalling and give them high manoeuvrability(Choi et al., 2012). Dolphins (aquatic mammals) reduce their drag by delaying the transition to turbulent flow on their body due to their anisotropic and compliant skin structure which dampens the flow instabilities(Pavlov et al., 2012).

This study will focus on the hydrodynamics of the skin of bony fish. More than 95% of the existing bony fish belong to teleosts whose skin is covered by leptoid scales that are further classified into scales of ctenoid and cycloid type(Nelson, 2007). Scale classification and morphology from various fishes were determined and inferred for possible hydrodynamic functions(Wainwright and Lauder, 2017)'(Wainwright et al., 2017). Most teleost fish operate at the Reynolds number range where transitional boundary-layer flow prevails on the fish surface(Gazzola et al., 2014)'(Anderson et al., 2001). In addition, their elongated body with an elliptical cross-section resembles that of an hydrofoil. Therefore, flow over these bodies can be closely related to the flow over a flat plate. Very few research on the flow dynamics over typical skins of teleost have been performed so far. For grass carp, (*Ctenopharyngodon idellus*) some geometric parameters of the scales were scanned and a bionic surface was created with individual, non-overlapping elements resembling those scales. When tested on a flat plate in a towing tank, the results showed a drag reduction of approximately 3%(Wu et al., 2018). Recently, some of the present authors have investigated the scale structure of European sea bass (*Dicentrarchus labrax*) and designed a biomimetic surface, which mimics the realistic features of overlapping scales and their characteristic surface pattern. Computation Fluid Dynamics (CFD) was used to study the flow pattern over the surface and revealed a hitherto unknown effect of the scales as a mechanism to generate a regular pattern of parallel streamwise velocity streaks in the boundary layer(Muthuramalingam et al., 2019). To prove their existence also on the real fish skin, oil flow visualisation was done on sea bass and common carp, which indeed confirmed their presence in a regular manner along their real body, with the same arrangement relative to the scale array as observed along the biomimetic surface. These results let the authors hypothesize about a possible mechanism for transition delay, inspired by various previous fundamental transition studies, where streaky structures generated by cylindrical roughness elements or vortex generator arrays have shown a delay of transition (Fransson et al., 2014),(Fransson et al., 2006),(Puckert and Rist, 2020).

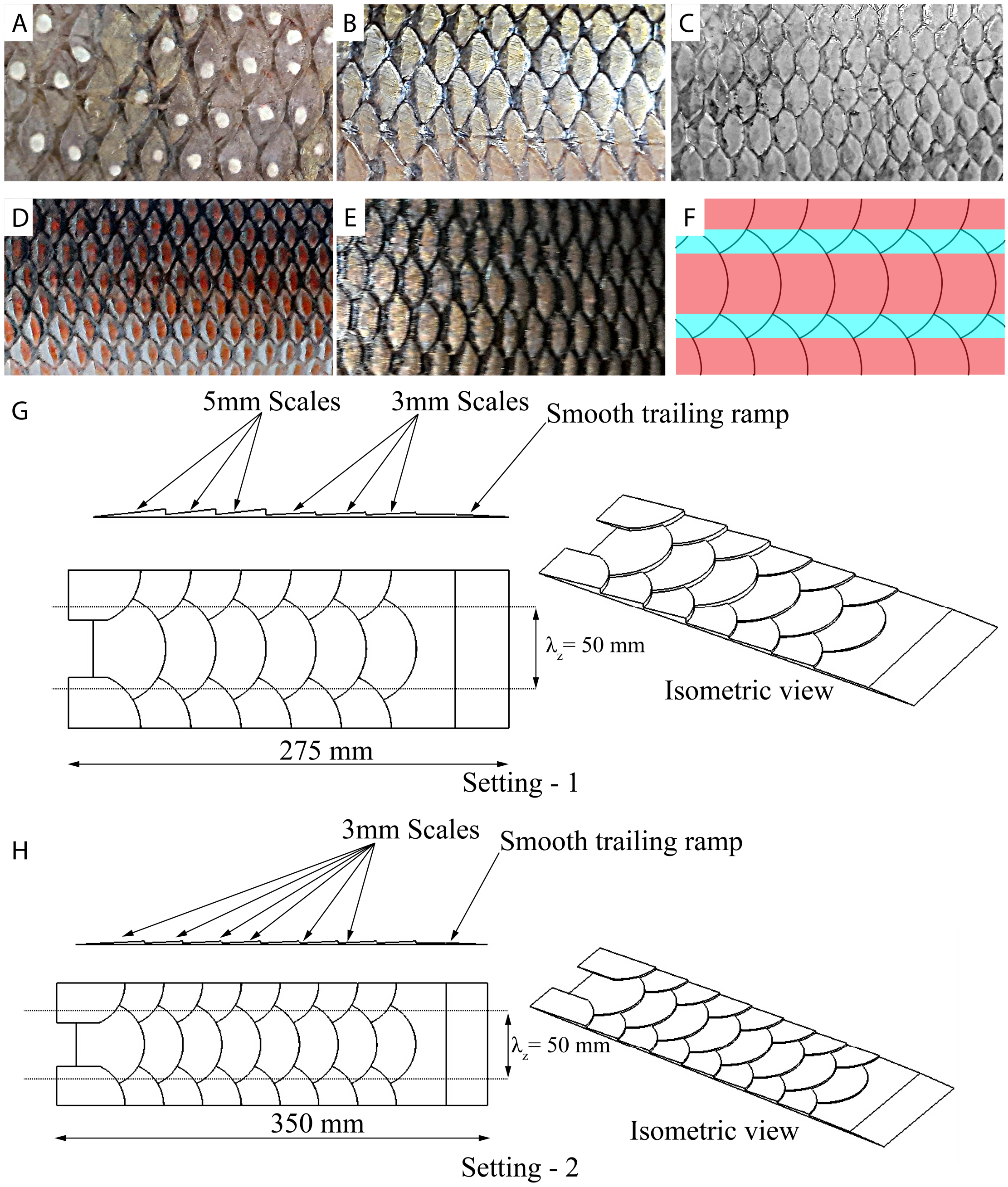

Figure 3.1: **Scale structure on different fishes, biomimetic scale array and CAD drawings of fish scale array** (A) Etroplus (*Etroplus suratensis*). (B) Mrigal carp (*Cirrhinus cirrhosus*). (C) Tilapia (*Oreochromis niloticus*). (D) Rohu (*Labeo rohita*). (E) Catla (*Labeo catla*). (F) Biomimetic scale structure (Pink: Central region, Light blue: Overlap region. (G) Setting-1 which has first three rows with 5mm thick scales followed by three rows of 3mm thick scales. (H) Setting-2 which has eight rows of 3mm thick scales.

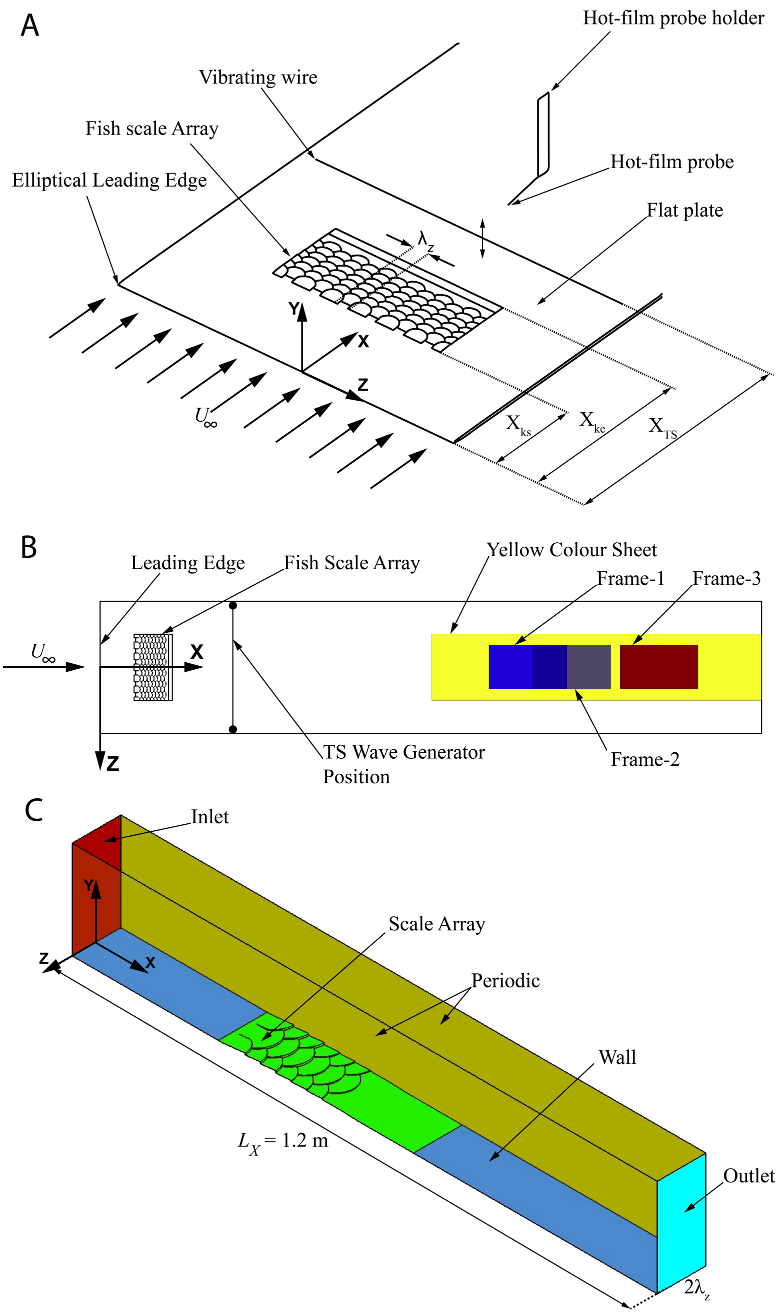

Figure 3.2: **Experimental flow set-up, details of flow visualisation set-up and computational domain** (A) Experimental Set-up in the Laminar Water channel with a biomimetic scale array. (B) Experimental arrangement from top view, Yellow area is the region in which a yellow sheet was glued on the flat plate. All three frames where videos were recorded are shown by rectangles. Note that Frame-1 and Frame-2 have some overlap. (C) CFD domain with periodic conditions. Setting-1 is shown in this figure and for Setting-2 all conditions remain the same except the fish scale array geometry. The inlet was provided with velocity parallel to X-axis with a value of $U_\infty = 0.086$m/sec.

The main purpose of this study is to prove this hypothesis with experiments in a well-established low-turbulence water channel facility, where the transition process can be studied under well-defined boundary conditions with controlled excitation of the fundamental instability of the Tollmien-Schlichting waves. In addition, the facility allows optical access to the boundary-layer flow and detailed measurements of the instability using hot-wire. The facility is established as a unique low-turbulence laminar water channel and there has been a long history of transition experiments(Wiegand, 1996)'(Kruse and Wagner, 1996)'(Lang et al., 2004).

The biomimetic scale array used in this study is based on the scale structure of European sea bass (*Dicentrarchus labrax*), and its details have been published in the authors' preceding paper(Muthuramalingam et al., 2019). Although the geometry was derived from sea bass, the scale pattern is common to most species of seawater and freshwater fishes. Figure.3.1F displays the scale pattern used in this study where the area with pink colour is the central region and the area with a light blue colour represents the region of overlap between adjacent scales. In a direct comparison with real fish scales, the biomimetic scale pattern in Fig.3.1F looks very similar to the natural scales of the species in Fig.3.1A-E.

3.2 Experimental Conditions

The experiments were conducted in the Laminar Water Channel of the Institute of Aerodynamics and Gas Dynamics in Stuttgart, Germany. The test section dimensions are 10m in length (streamwise direction: X-axis), 1.2m in width (spanwise direction: Z-axis) and 0.2m in height (wall-normal direction: Y-axis) with a turbulence intensity value less than 0.05%(Puckert and Rist, 2020). Hot-film anemometry was used to measure the velocity of the flow inside the water channel. A flat plate was used to generate a laminar boundary-layer flow over it at a flow velocity (U_∞) of 0.086m/sec corresponding to a Reynolds number of $Re_L \sim 5.2 \cdot 10^5$ based on the flat plate length ($x = L$) of 6m, where the Reynolds number is defined by ($Re_x = xU_\infty/\nu$) and ν is the kinematic viscosity of water. The experimental details are shown in Fig.3.2A. The leading edge of fish scale arrays was located at (X_{ke}) 0.3m from the leading edge and two models were used to develop different streak amplitudes. The first model, Setting-1 was 3D printed with three rows of scales with 5mm height followed by three rows of scales with 3mm height. The second model, Setting-2 was 3D printed with eight rows of scales with 3mm height. The trailing edge of the model has a smooth ramp to avoid separation behind the model. The roughness height of the scales (h_s) on sea bass was around 0.15mm for a fish length of 350mm. At a swimming speed of around 1.5m/sec the boundary-layer thickness (δ) will be about 0.5mm at the location where the scale array begins, which leads to a δ/h_s ratio of 3. Hence, in this study the δ/h_s ratio is maintained to match the dynamic similarity after the upscaling of the biomimetic scale array(Panton, 2013). This is a common practice in fluid mechanics to upscale the model based on geometric and kinematic similarities, for example, see the tests on upscaled shark skin scales here(Bechert et al., 2000). The CAD drawings of both models are shown in Fig.3.1G and Fig.3.1H in detail. The roughness Reynolds number defined by $R_{kk} = ku_k/\nu$ is 334 for Setting-1 and 143 for Setting-2, where u_k is the undisturbed velocity without roughness at the height (k) of the maximum roughness(Doenhoff and Braslow, 1961). Both models were 3D printed in spanwise segments of 0.2m so that the length of the total setting in Z-axis was 0.6m. A standard procedure in transition research along a flat plate is used herein to investigate the response of the boundary layer to the modified surface. The method uses a vibrating wire, which is spanned in the spanwise direction and used to excitep a 2D Tollmien-Schlitching wave(Schubauer and Skramstad, 1947). Location of the wire within the boundary layer and the vibration frequency are adapted to the theoretical instability diagram of the Blasius solution for a laminar 2D boundary layer(Schubauer and Skramstad, 1947). A wire of 0.1mm diameter is located at $X_{TS} = 1.2$m from the leading edge of the flat plate(Puckert and Rist, 2020) at a wall-normal distance of 5mm from its surface and vibrating at a physical frequency of $f = 0.2\text{Hz}$ (the corresponding normalised frequency is $F = 2\pi f \nu / U_\infty^2 = 166 \cdot 10^{-6}$) with an amplitude of 0.25mm.

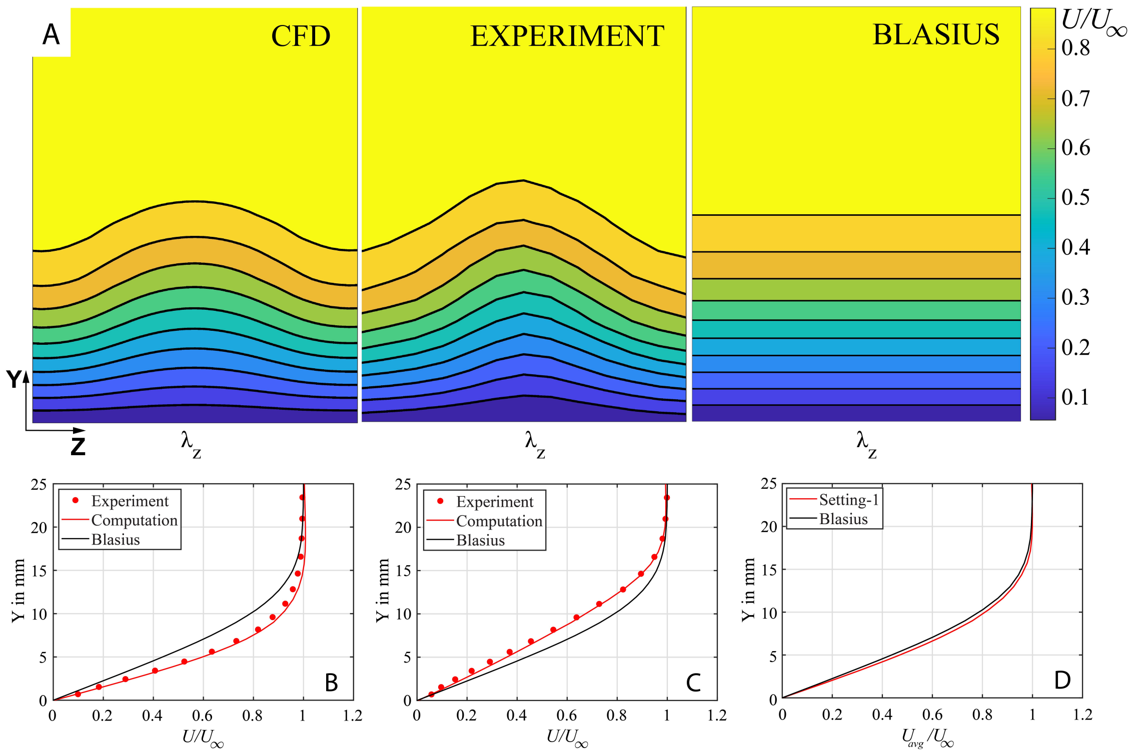

Figure 3.3: **Comparison of CFD with experimental results** (A) Velocity variation of streaky base flow in $Z - Y$ plane at a distance of 1.2m from the leading edge (Left - CFD result, Middle - Hot-film result, Right - Blasius). Normalised velocity profile at (B) the overlap region (high-velocity region) behind the scale array $Z = 0.025\text{m}$. (C) at the central region (low-velocity region) behind the scale array $Z = 0\text{m}$. (D) Spanwise averaged streamwise velocity profile for Setting-1. Black line - Reference Blasius velocity profile

3.3 Results

The surface, mimicking the array of overlapping scales along the flat plate in the low-turbulence facility, again show the generation of streamwise velocity streaks, similar as detected in our previous study on real fish bodies(Muthuramalingam et al., 2019). Contours of constant streamwise velocity in a cross-section of the boundary layer in Fig.3.3A illustrate the velocity variation at 1.2m from CFD simulation and experiment for one wavelength of the streak ($\lambda_z = 50$mm) for Setting-1. Note, that the result is periodic in spanwise direction with each row of scales. The Blasius contour at the right depicts the 2-D mean flow over the same wavelength(White, 2006). A detailed comparison of velocity profiles in the high- and low-velocity regions behind the scales are shown in Fig.3.3B and Fig.3.3C, respectively. In the region of high velocity and low velocity regions the deviation from the reference Blasius profile depicts velocity deficit or increase behind the scale array. Spanwise averaged streamwise velocity in the streaky flow is compared with Blasius profile in Fig.3.3D. The streaky flow produces a fuller velocity profile when compared with the reference flow which results in a shape factor of 2.47 instead of 2.59 which is comparable with the Large Eddy Simulation results reported in literature for the streaky base flow(Schlatter et al., 2010). CFD and experimental results are comparable with only minor variations that may be attributed to the boundary conditions and the experimental uncertainties. Measurements at different locations further downstream prove that the streak persists in streamwise direction (not shown here).

This modulation of the velocity is fundamentally different from the streaky structure generated by the lift-up effect caused by a vortex generator or cylinder array(Fransson and Talamelli, 2012). The streaky structure generated by the overlapping scales is formed by a spanwise periodic flow very close to the surface, and the amplitude of the streak increases with the number of scale rows in the direction of flow. Setting-1 with about the same number of scales as Setting-2 but twice as thick produces a streak amplitude approximately twice as large compared to Setting-2 ($A_{st} \sim 20\%$ for Setting-1 and $A_{st} \sim 10\%$ for Setting-2) as shown in Fig.3.4A. The streak amplitude is defined as in Eqn.3.1 and increases with the number of scale rows from the leading edge of the model, it is seen from Fig.3.4A within X = 0.3m to X = 0.6m (It is the extent where the scales are placed on the tunnel). Afterwards it drops as a result of the decelerating trailing ramp. Once again the flow reorganises up to some extent to increase the streak amplitude and then the viscosity causes it to decay continuously downstream. Both models did not induce a bypass transition (instantly tripping laminar flow into turbulent), nor did they induce secondary streak instability as seen from hot-film signals and with flow visualisations.

$$A_{st} = \left[\max_y \{U(X, y, z)\} - \min_y \{U(X, y, z)\} \right] \Big/ (2U_\infty) \tag{3.1}$$

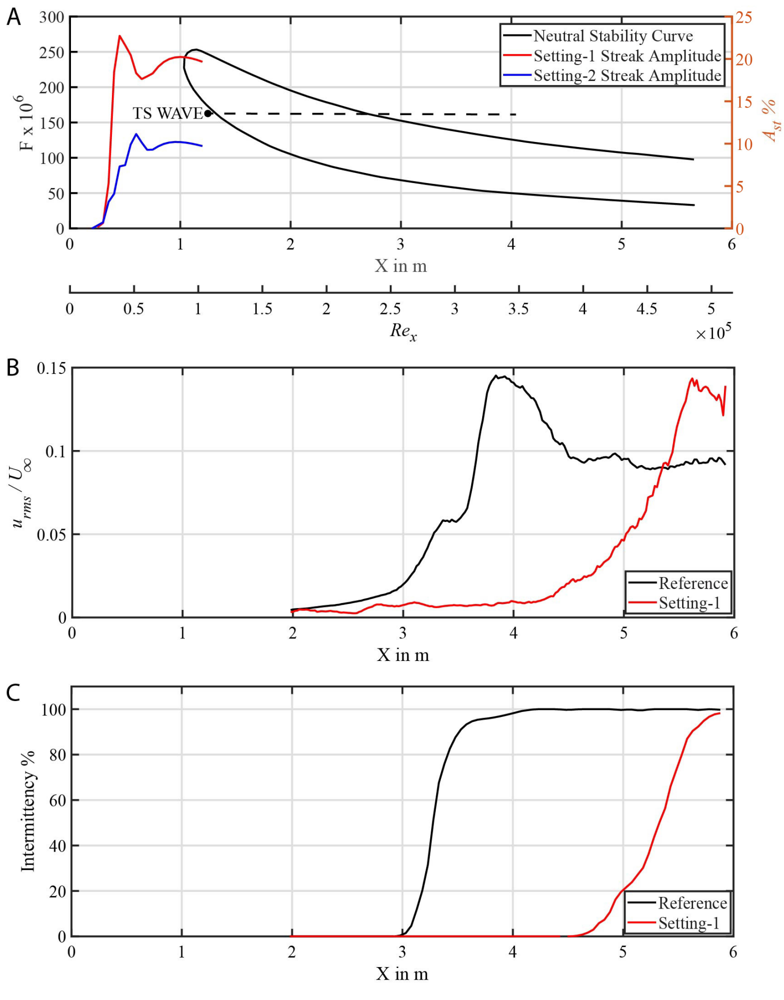

Figure 3.4: **Neutral stability curve, root mean square of velocity fluctuations and intermittency variation** (A) Neutral stability curve and streak amplitude for two settings. (Normalised frequency F given in left 'y' coordinate and streak amplitude A_{st} given in right 'y' coordinate, Black dot marks the TS wave generator position and dotted line indicates the frequency value). (B) u_{rms} plot normalised by free stream velocity (U_∞) for reference flat plate and Setting-1. (C) Intermittency plot for reference flat plate and Setting-1

To investigate the response of the boundary layer to the scaled surface with regard to the laminar-to-turbulent transition process, a controlled transition experiment with a representative Tollmien-Schlichting (TS) wave at a given frequency were performed, following the method invented in (Schubauer and Skramstad, 1947). In Fig.3.4A the neutral stability curve is shown as a black line for the present free-stream velocity of $U_\infty = 0.086$m/s. The neutral stability curve is given along the X-axis and also for comparison with non-dimensional parameters in similar studies based on the Reynolds number (Re_x). The area within the stability curve is the region in which, according to linear stability theory, infinitesimal disturbances will grow exponentially(Schlichting and Gersten, 2017). The velocity signals were measured for 60sec at a data acquisition frequency of 100Hz at $Y = 10$mm from the wall from $X = 1.98$ m to 5.92m for the reference flat plate and fish scale array (Setting-1) cases. In the reference case, the induced small disturbances from the vibrating wire grow in the streamwise direction inside the instability region which can be inferred from the black u_{rms} curve from 2m to 2.6m in Fig.3.4B. Initially, the so-called primary instability mechanism increases the velocity fluctuations until secondary instability mechanism set in, afterwards the fluctuations increase rapidly until they reach a peak around 3.8m in Fig.3.4B. From there on the flow is turbulent as observed from the constant u_{rms} plateau after 4.5m(Shahinfar et al., 2012). However, for the flow with fish scale array (Setting-1), as seen from the red line in Fig.3.4B the fluctuation level u_{rms} remains almost constant until 4m and it increases monotonically but with a lower rate when compared with the reference case. The local flow state can be defined generally by the intermittency parameter which classifies the flow into laminar, turbulent, and transitional (Zhang et al., 2013). The value in percentage indicates the nature of the flow, e.g.: zero represents laminar flow and 100% represents fully turbulent flow, and any value in between indicates how long the flow is turbulent in a given period of time. For the reference flat plate case, the flow is laminar until 3m and becomes turbulent just after 4m as shown in the black curve in Fig.3.4C. For the case with fish scale array as shown in the red line in Fig.3.4C, the flow remains laminar for a larger extent until 4.65m and then becomes turbulent around 6m. This results in a streamwise extension of laminar flow by about 1.65m which corresponds to a 55% delay in transition location.

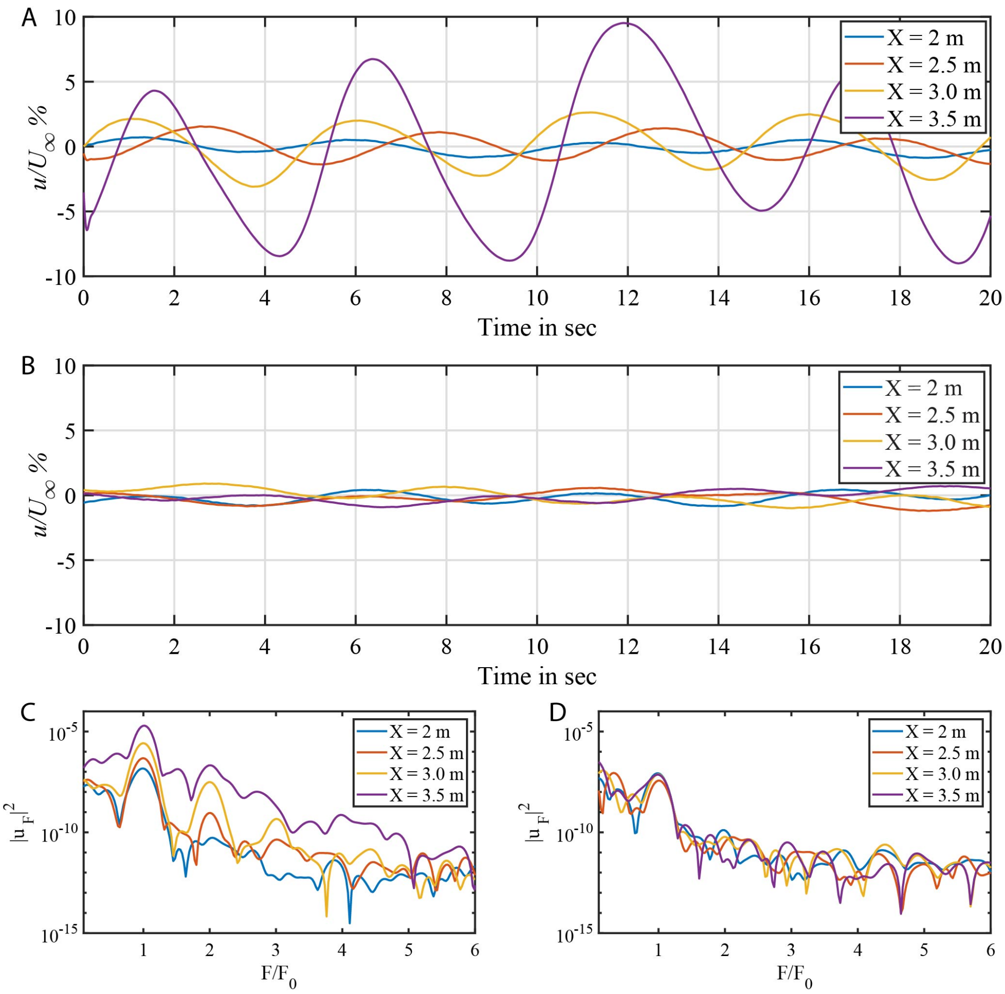

Figure 3.5: **Instantaneous velocity and spectrum for reference flat plate and fish scale array case** (A) Instantaneous velocity at four locations for reference flat plate case. (B) Instantaneous velocity at four locations for fish scale array case (Setting-1). (C) Spectrum for the velocity signals for reference flat plate case. (D) Spectrum for the velocity signals for fish scale array case (Setting-1).

Next, we explore the flow by means of temporal velocity signals for the two cases previously discussed. Figure.3.5A displays the velocity signals subtracted from their mean values at 2, 2.5, 3.0 and 3.5 m for a period of 20 sec for the reference case without fish scales. The amplitude of the velocity signals in Fig.3.5A increases

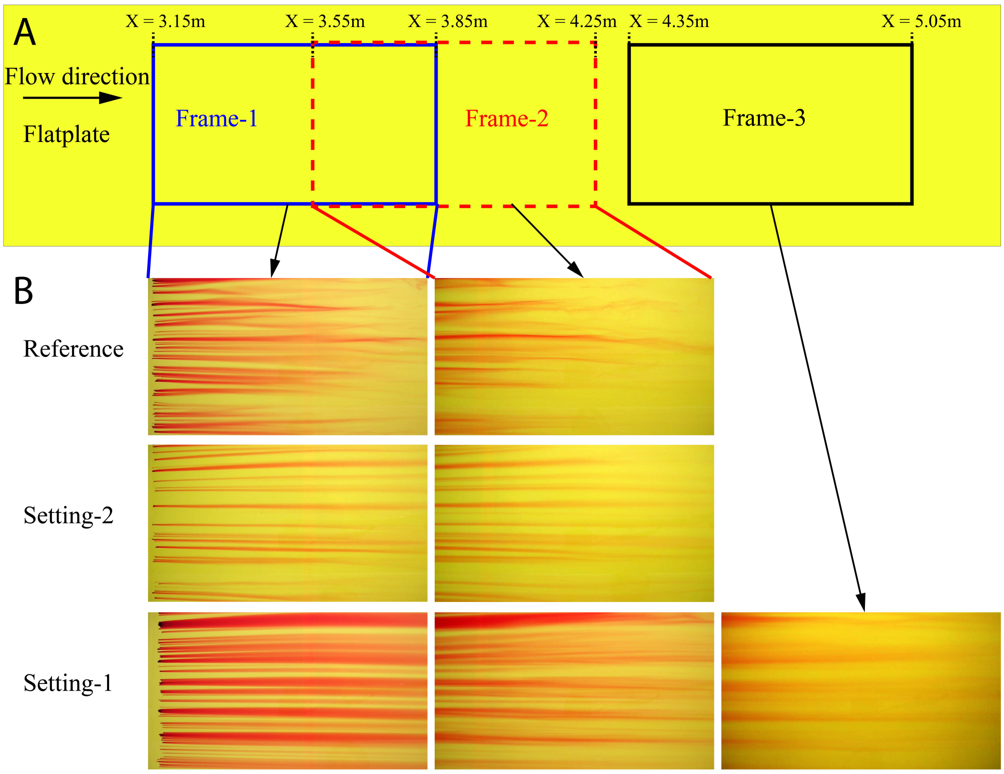

Figure 3.6: **Flow visualisation results** (A) Flow visualisation setting, Frame-1: 3.15 to 3.85m (Blue rectangle), Frame-2: 3.55 to 4.25m (Dotted red rectangle), Frame-3: 4.35 to 5.05m (Black rectangle). Blue line pair mark Frame-1 and Red line pair mark Frame-2 regions. (B) Flow visualisation pictures for reference, Setting-2 and Setting-1 cases.

with streamwise coordinate X. The respective frequency spectra of these velocity signals is given in Fig.3.5C, where the abscissa is normalised with respect to the vibration frequency (F_0 = 0.2Hz) of the vibrating ribbon. At X =2m the spectrum displays a peak at F/F_0=1 which indicates that the fluctuation energy is only from the wire's fundamental vibrating frequency. Higher harmonics and subharmonics of the fundamental frequency F_0 appear further downstream (see the peaks at 3 and 3.5 m) and the disturbance energy also increases compared to the spectrum at 2m. At 3.5m the energy is increased over all frequencies given in the plot indicating that the flow is becoming increasingly disturbed resulting in turbulence. On the contrary, the velocity magnitude for the flow with fish scale array remains within 2% at all locations, as shown in Fig.3.5B. At the same time the fluctuation energy

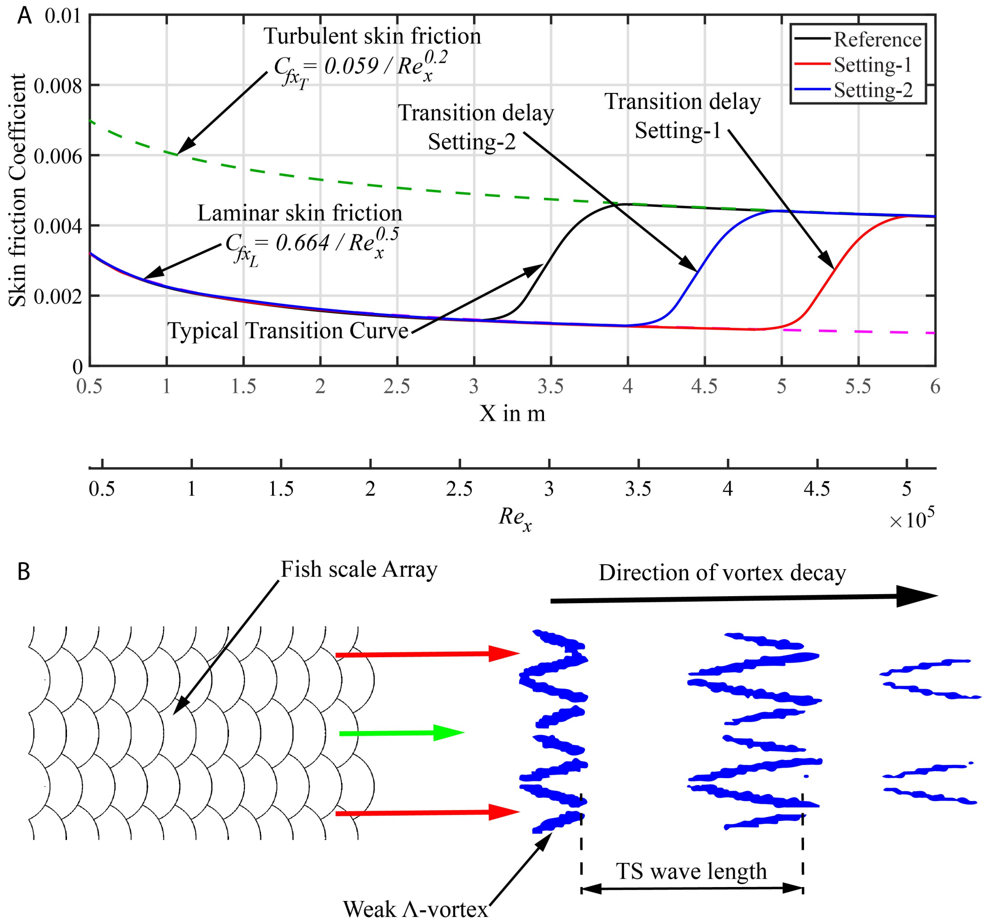

Figure 3.7: **Typical skin friction plot and proposed flow manipulation mechanism** (A) Skin friction coefficient curve: Dashed green line - Turbulent flow, Dashed pink line - laminar flow. (B) Flow behind fish scale array with modulated TS wave. Red arrow - High-velocity region, Green arrow - Low-velocity region.

is very small compared to the flat plate case as shown in Fig.3.5D. Additionally, the higher harmonic components in the flow are completely absent in the case of the fish scale array. This reflects the very low level of velocity fluctuations u_{rms} depicted by a red line in in Fig.3.4B. The increase of u_{rms} beyond 4m is due to uncontrolled background oscillations of the water tunnel and not necessarily due to a re-amplification of the TS wave.

Complementing information about the flow states in different cases is obtained from flow visualisation using the method of surface streakline generation. Individual potassium permanganate crystals were placed on the flat plate and, while dissolving as dye in the water, they visualize the flow close to the surface. These streak lines will be visible as compact dye lines if the flow is laminar, while, in contrast, they develop kinks and diffuse very quickly when the flow is turbulent. The locations where the visualisations has been done is shown in Fig.3.6A for brevity. Figure.3.6B(Reference) shows the visualisation picture for the reference flat plate case from X =3.15 to 3.85m. Certainly, the streaklines are visible for more than 70% of the picture indicating laminar flow with some instabilities. In Figure.3.6B(Reference), where the frame is from 3.55 to 4.25m the streaklines have broken down because of the turbulent flow which is comparable with the hot-film measurements explained above. Figure.3.6B(Setting-1) portray the visualization picture for the same locations described previously, but for the case with fish scale array (Setting-1). The flow is completely laminar in the given locations and even for an additional location from 4.35 to 5.05m as shown in Fig.3.6B(Setting-1). For the case with the second set of fish scale array (Setting-2), the flow is still laminar in the above-mentioned locations until the end of the picture as shown in Fig.3.6B(Setting-2). Hence, this visually proves that the fish scale array increases the laminar flow extent by delaying the transition and this result is in perfect agreement with the transition delay visualisations performed with cylindrical roughness elements(Fransson et al., 2006).

3.3.1 Drag estimation

Flow over any body will experience drag that has two components, skin friction and pressure drag. For a flat plate, the drag is only from skin friction with the friction coefficient for laminar and turbulent flow given by Eqn.3.2 and Eqn.3.3, respectively(White, 2006). These equations were compared with Direct Numerical Simulation results and found to be comparable with similar kind of TS waves(Sayadi et al., 2013).

$$C_{fx_L} = 0.664/\sqrt{Re_x} \tag{3.2}$$

$$C_{fx_T} = 0.059/{Re_x}^{\frac{1}{5}} \tag{3.3}$$

Hence, the total drag along a flat plate with laminar and turbulent flow regimes can be approximated by the summation of the drag components by the Eqn.3.4, where, x_L is the location from the leading edge of the flat plate where the flow is assumed to change from laminar to turbulent state.

$$D_{Net} = D_L + D_T + D_P = \int_0^{x_L} \frac{1}{2} C_{fx_L} \rho U_\infty^2 dx + \int_{x_L}^{L} \frac{1}{2} C_{fx_T} \rho U_\infty^2 dx + D_P \tag{3.4}$$

For the sake of comparing the drag for both cases, the location x_L is assumed where the intermittency factor reaches a value of 50%. For the reference flat plate case the location x_L is estimated from the hot-film measurements to be at 3.3m and for the case with the fish scale array (Setting-1) the location x_L is placed at 5.3m. For Setting-2 the location x_L is chosen from the flow visualisation of about 4.3m since we do not observe any turbulence even at Frame-2. Additionally, when a body like fish scale array is mounted on the flat plate it experiences added pressure drag (D_P). The value of this drag component is calculated from the CFD simulation for a length of $L_X = 1.2$m (as shown in Fig.3.2C). The components of drag for the two cases are given in Table.3.1. The net drag ($\mathrm{D_{Net}}$) is reduced by 0.02N with the fish scale array (Setting-1) and 0.008N for Setting-2. This results in a net drag reduction of about 27% for Setting-1 and 10.7% for Setting-2 when compared with the reference flat plate case.

Configuration	Laminar region x_L (m)	Laminar drag D_L (N)	Turbulent drag D_T (N)	Pressure drag D_P (N)	Net drag D_{Net} (N)
Reference	3.3	0.030421	0.044954	0	0.075375
Setting - 1	5.3	0.038553	0.011172	0.005648	0.055373
Setting - 2	4.3	0.034726	0.027573	0.005048	0.067347

Table 3.1: Comparison of estimated drag for reference flat plate and fish scale arrays

This result can be understood by using the skin friction plots as depicted in Fig.3.7A. The laminar skin friction curve is shown as a dashed pink line and the turbulent skin friction curve as a dashed green line. Typical transition curves appear in all the cases considered here(White, 2006). Generally, if a flow becomes turbulent the skin friction coefficient rises to almost twice its value for laminar flow at a particular location. The total drag of the surface is the area under the skin friction curve, therefore, the area under the curve reduces for fish scale array when compared with the reference flat plate case. Furthermore, the reduction in integral amplitude is proportional to the streak amplitude in the experiments considered here.

We have demonstrated that the fish scale array could delay transition to reduce the net drag. The underlying mechanism is the attenuation of the modulated TS waves due to the streamwise velocity streaks in the base flow. The latter produce a spanwise averaged flow with a steeper velocity gradient than the Blasius solution (reference flat plate case). This leads to a smaller shape factor which is known to stabilize the boundary layer (Schlatter et al., 2010)'(Dörr and Kloker, 2018). This is also seen by the streamwise decay of the observed lambda-vortices for the scales. In comparison, in the classical transition scenario (regular Blasius flow) the two dimensional TS waves grow inside the boundary layer within the linear instability region and grow further until the amplitude of fluctuation increases above a critical amplitude, which is when three-dimensional undulations lead to the formation of strong Λ-vortices(Grek et al., 2000)(non-linear flow regime based on H-type or K-type transition(Schlatter et al., 2010)) and ultimately to turbulence. The spanwise wavelength of these Λ-vortices (spacing between the legs of the Λ-vortex) is generally larger than half of the TS wavelength(Saric, 1986). Herein, for the streaky base flow, the TS waves reorganise already early in the linear phase into weak Λ-vortices as depicted in Fig.3.7B due to the streamwise modulation of the flow. The spanwise wavelength of these weak Λ-vortices is equal to the wavelength of the fish scale array, different from the wavelength on natural transition. In addition, because of the stabilizing effect of the smaller shape-factor of the boundary layer(Dörr and Kloker, 2018) the weak Λ-vortices decay in the downstream direction. This proposed mechanism follows similar arguments given in (Schlatter et al., 2010) for the simulation of transition delay due to finite amplitude streaks.

3.4 Conclusions

In this paper, we have investigated and shown the stabilizing influence of a periodic streaky base flow generated by a biomimetic scale array along a flat plate boundary layer on a Tollmien-Schlitching wave. In the following we shall discuss these results with respect to the existing literature on transition delay after listing out the salient outcomes from this study. The following observations were made:

- The biomimetic fish scale array produces stable velocity streaks in the otherwise laminar boundary-layer flow. The spanwise wavelength of the streaks can be controlled with the spacing between adjacent rows of the scale array.

- The streak amplitude can be increased by increasing the number of rows in streamwise direction or by increasing the thickness of the scale array, as long as the roughness height is not exceeding a critical level to trigger bypass transition.

- The velocity profile develops towards a smaller shape factor (on average over the span) which is known to stabilize the boundary layer (Dörr and Kloker, 2018). As a consequence, early 3D instabilities of the TS waves in form of weak Λ-vortices decay again while convecting downstream, which results in a delay of transition, similar as observed in (Schlatter et al., 2010)

- The observed transition delay has direct consequences on the skin friction drag, as the laminar part of the boundary layer is extended relative to the reference flat plate case. This reduces the energy consumption to overcome the wall friction loss.

As explained in the introduction, most fish species operate in the transitional laminar-to-turbulent Reynolds number regime which was tested in this study (i.e., $Re_L \sim 10^5$). Experiments revealed that the scale array attenuates the TS wave and hence is able to delay laminar-turbulent transition which results in a maximum net drag reduction of about 27% for the given configuration. The present mechanism to generate the streaks differs from those in previous studies where cylindrical roughness elements and vortex generators were used to delay transition. Cylinder arrays can produce maximum streak amplitudes of about 12%, beyond that, the cylinders will trigger bypass transition because of the absolute instability in the wake(Shahinfar et al., 2012). In addition, the roughness elements generate parasitic drag due to the pressure drop around the protruding body. Vortex generators can delay transition with higher streak amplitudes without secondary instabilities, however, they will act as bluff bodies when the flow is not perfectly aligned with the orientation of the vortex generator. Additionally, in the case of purely laminar flow where transition does not occur (i.e. $Re_L < 10^4$), these two types of bodies will always generate parasitic drag.

To be effective at all operating Reynolds numbers, it requires a multi-role flow control mechanism. Our previous studies showed that the biomimetic fish scale array already achieved laminar drag reduction in a clean laminar flow (where the ratio of boundary-layer thickness to the maximum scale height was greater than 10), thus reducing the drag in the low-velocity regime, too(Muthuramalingam et al., 2019). The mechanism by which the overlapping scales generate the streaks is via producing a spanwise flow near the wall, which is sustained by the repeated overlapping along the rows of the scales. When the swimming speed increases and the flow is likely to be transitional, the streaks from the scales tend to prolong the laminar flow by delaying the transition without adding any parasitic drag, thus minimizing skin friction. Note, that the results further indicate no tendency of the scales to generate a by-pass transition. Therefore this mechanism is assumed to be robust against moderate variations in details, like scale shape and height. The results let us speculate that the overlapping scale arrays on most bony fishes are an evolutionary result to minimize friction drag by producing streaky flow which produces a fuller laminar velocity profile on the surface (smaller shape-factor).

Despite the promising results from this study, salient limitations should be mentioned. Primarily, the tests were done on a flat plate ignoring the pressure gradient which is inevitable on the body of the fish. However, recent experiments on an aerofoil with streaky base flow generated by miniature-vortex generators delays transition for a particular configuration which motivates the use of these fish scale array on a surface with imposed pressure gradient(Roy, 2018). Secondly, the flexibility of the scales and also the undulatory motion of the fish is not considered here, which largely changes the transitional boundary layer(Kunze and Bruecker, 2011) due to unsteady effects which were not part of the present study. Therefore, the primary focus was on the performance of the biomimetic fish scale array on a very controlled transition scenario for comparison with previous studies which were successful in delaying flat-plate boundary-layer transition. From the observation that streaks exist, already proven with the help of surface flow visualisations on a real fish, and the observation that scale arrays delay transition without by-pass transition, it is hypothesized that the fish scales are efficient in delaying laminar-turbulent transition on a real fish body, as well. Additionally, the performance of the scale array (rigid or flexible) in turbulent or separated boundary layers remains to be studied in future research.

3.5 Methods

3.5.1 Biomimetic fish scale models

Biomimetic fish scale models were 3D printed at City University of London and University of Stuttgart using ABS plastic material of density about 1080kg/m^3. The array was made in many pieces because of the size restriction in the printer. The models were modeled in CATIA and were 200mm wide and printed as separate tiles with extra 1mm thickness at the base for stable print. The leading part with smooth ramp and three scale rows was printed as one piece and the other three scale rows with trailing edge ramp were printed as a separate piece. When placed one behind the other it will be acting as a single array of scale rows. The tile with scale array was glued on the flat plate of the Laminar Water Channel to keep it in place without any movements. Two models have been used in this study as shown in Fig.3.1G and Fig.3.1H.

3.5.2 Experiments using water channel

The experiments were conducted in the open channel closed loop Laminar Water Channel (Laminarwasserkanal) at University of Stuttgart, Germany. The flow is induced by two axial propellers connected to a frequency control drive to vary the RPM. The flow from the pump is passed through a honeycomb chamber followed by a long diffuser with a series of screens to a settling chamber with a contraction ratio of 7.7:1. Before the contraction three additional sets of screens were used to reduce the turbulence. The turbulence intensity lies below 0.05% within a frequency range of 0.1 - 10Hz at 0.145m/s(Wiegand, 1996). The dimensions of the test section are 10m in length, 1.2m in width and 0.2m in height. Inside the test section a very long but segmented glass plate is used to create a two dimensional Blasius boundary layer. The leading edge of the first plate is elliptical to reduce the leading edge separation and getting zero pressure gradient on the flat plate quickly. In the spanwise direction the plates are little less than the widths of the water channel which provides natural suction to prevent the corner flows. Constant temperature hot-film anemometry was used to measure the velocity of the water using DANTEC 55R15 with a 16-bit A/D converter. The overheat ratio for the hot-film probe was set at 8% as given in the manufacturer manual. All the measurements in this study have been acquired at 100Hz for 60 sec. Before starting the measurement the hot-film was calibrated in still water by traversing the probe with a controlled series of constant velocities to acquire the corresponding voltage from the data acquisition system. Finally a correlation graph was used to find the coefficients in King's law to relate the voltage (E) with velocity (U) given by

$$U = \left[\frac{E^2 - A}{B}\right]^{\frac{1}{C}}. \tag{3.5}$$

The data was post-processed in MATLAB for filtering the signals and also to find the spectrum of the signals. For details on the experimental facility and measurement equipment, the reader is referred to(Puckert, 2019).

3.5.3 Flow visualisation

To perform flow visualisations the water channel was emptied below the flat plate to dry the surface. A yellow colour sheet of width 600mm and length of about

2500mm was placed on the flat plate for better contrast. Then it was left to glue on the surface for a day. The yellow colour sheet was placed from 3 to 5.5m on the flat plate where the flow disturbances grow from laminar to turbulent flow. Potassium permanganate crystals (less than 2mm in average) were placed at the start of the yellow sheet. As the crystals dissolve with water they will colour the water without changing its physical properties. The coloured water will be clearly identified in the regions where the flow is laminar and quickly diffuse and disappear in the turbulent flow regions. The dye flow visualisation was recorded from above the tunnel using digital cameras from three regions. All the video recordings were done with a shutter time of 1/30 seconds. The first frame was from 3.15 to 3.85m, the second frame from 3.55 to 4.25m and the third frame from 4.35 to 5.05m. The setup of the flow visualisation is shown in Fig.3.2B.

3.5.4 CFD Methodology

The computational study was done using ANSYS-Fluent 19.0. The CFD domain with fish scale array was modeled in CATIA with a spanwise length equal to two wavelengths of the array $2\lambda_Z = 100$mm as shown in Fig.3.2C. The leading edge of the fish scale array was placed at $X = 300$mm from the leading edge of the flat plate as in the experiments. The length of the domain in the streamwise direction was set to 1200mm and in the wall normal direction the domain was 200mm in length. The inlet was specified with a velocity of $U_\infty = 0.086$m/sec and the outlet was specified as a pressure outlet. Periodic boundary conditions were used in the spanwise direction and the top domain was specified as free shear boundary with zero normal velocity. The domain was dicretised with 2mm elements in the streamwise direction, 1.43mm in the spanwise direction. The first cell height in the wall normal direction was set at 0.035mm with inflation of 20 cells within 2mm to capture the near wall gradient and a total of 110 grid points were used to mesh the wall normal direction. The major part of the domain was discretised with a Cartesian, structured mesh except the volume with fish scale array which was meshed with both prism and tetrahedral elements.The total number of elements for Setting-1 is 7.8 million and Setting-2 is 8.5 million. Second order pressure and second order upwinding schemes were used for discretisation with a steady state solver which was used to compute the laminar flow through the domain.

Point of clarification: *"The increase of u_{rms} beyond 4m is due to uncontrolled background oscillations of the water tunnel and not necessarily due to a reamplification of the TS wave".* Is it suggesting that the red line in Fig.3.4b is not indicating boundary-layer transition beyond 4m?
The red line in Fig.3.4b is indeed indicating boundary-layer transition beyond 4m. However, the transitional flow is not promoted from the TS wave, but because of the sloshing effect of the tunnel. Open surface water tunnels are known for the sloshing effect similar to oscillation of water like a U-tube. The fundamental frequency of this oscillation is around f=0.07 Hz(Puckert et al., 2017). From the spectrum plots after 4m (not shown here) it was clear that the transition is not from the fundamental frequency or from the harmonics of the TS wave, but from the sloshing effect.

3.6 Critical Analysis

The experimental study revealed that the biomimetic fish scale array could delay transition by suppressing the TS waves, it was tested for two different streak amplitudes. In this section, some responses are given to the comments and suggestions from the reviewers.

Claim-1: *Only one frequency was tested in the water channel. What is the response for other frequencies and wavelengths?*

Due to COVID restrictions, the laminar water tunnel in Stuttgart, Germany could not be accessed further on , therefore CFD was used to find the response for other frequencies. The biomimetic scale arrays used in this CFD study were exactly the same which were used in the laminar water tunnel experiments (Setting-1 and Setting-2 respectively). The computational domain starts from 0.8 and extends to a length of 5m in the streamwise direction as shown in Fig.3.8 and other dimensions were exactly the same as explained in the main text of this chapter. Simulations were used to find the response of the streaky flow at three different TS wave frequencies (f = 0.1, 0.15 and 0.2 Hz). While in the experiments, a vibrating wire was used at a distance of 1200mm from the leading edge to induce the TS waves, during computations a method leaned upon the computational technique from (Rist and Fasel, 1995) was implemented, which generated vorticity disturbances at the bottom wall in a controlled way (TS wave inlet), placed 0.24m (X_{st}) downstream from the main inlet at X_{inlet} from origin. The disturbance overlaid on the velocity profile in the form of a TS wave is shown in Fig.3.8 and it was specified as a user-defined function in Ansys-Fluent. The amplitude of the TS wave velocity was 0.01% of the free stream velocity ($U_\infty = 0.086 m/s$). Inlet to the computational domain was specified with the three velocity components and the pressure distribution from the steady state simulations as a profile data (contains mesh and associated velocity and pressure informations) from a plane at 0.8m. The top domain is specified with free stream velocity in streamwise direction and the wall normal velocity was specified with the vertical velocity from the Blasius-type boundary layer profile. A Non-Iterative Time Advancement (NITA) scheme was used to compute the transient laminar flow solver with central difference method for the momentum equation and second order implicit method for the transient formulation (Watmuff, 2014). One TS wave cycle period was divided into 500 time steps at frequency f = 0.2 Hz (667 time steps at f = 0.15 Hz and 1000 time steps at f = 0.1 Hz, respectively), so that the CFL number always lies within 0.5 to ensure stability of the transient flow simulation.

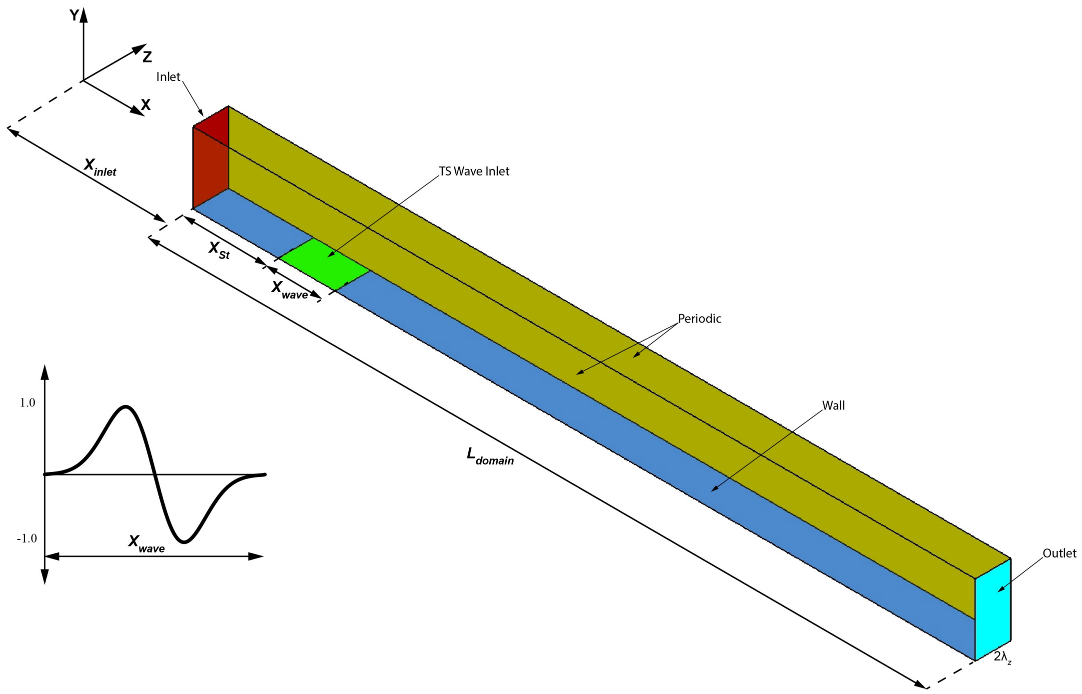

Figure 3.8: **Domain for TS-wave CFD simulation** Inlet to the domain is $X_{inlet} = 0.8m$ from the leading of the flat plate. $L_{domain} = 4.2m$ which starts from 0.8m and ends at 5m in X-direction. The typical profile of the TS-wave velocity is shown on the left.

Figure.3.9A shows the computed mean velocity profile (normalised streamwise component at TS wave of f=0.2Hz) compared with the Blasius profile at a location X = 1.2m. Fig.3.9B shows the corresponding profiles of the streamwise and wall nor-

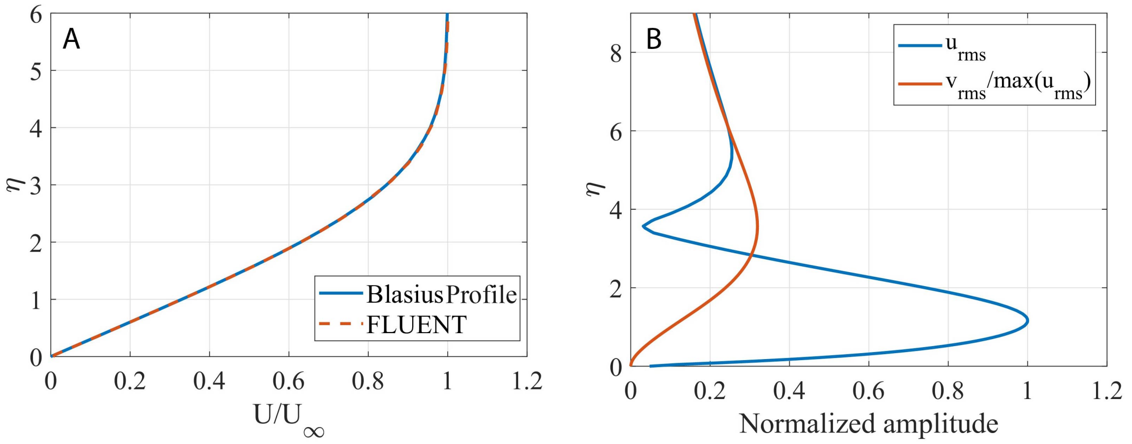

Figure 3.9: **Boundary layer and fluctuation profiles at X = 1.2m:** (A) Comparison streamwise velocity profile from computation with Blasius profile. (B) Streamwise and wall normal fluctuation velocity profiles for f = 0.2 Hz.

mal velocity fluctuations, calculated from a total period of two successive TS wave cycles. The velocity and fluctuation profiles are comparable in shape and structure with the literature (Rist and Fasel, 1995) for a similar case of computational TS wave (same Re-number, same distance) which shows that ANSYS-Fluent herein is a valuable tool to perform a linear stability analysis for the streaky base flows.

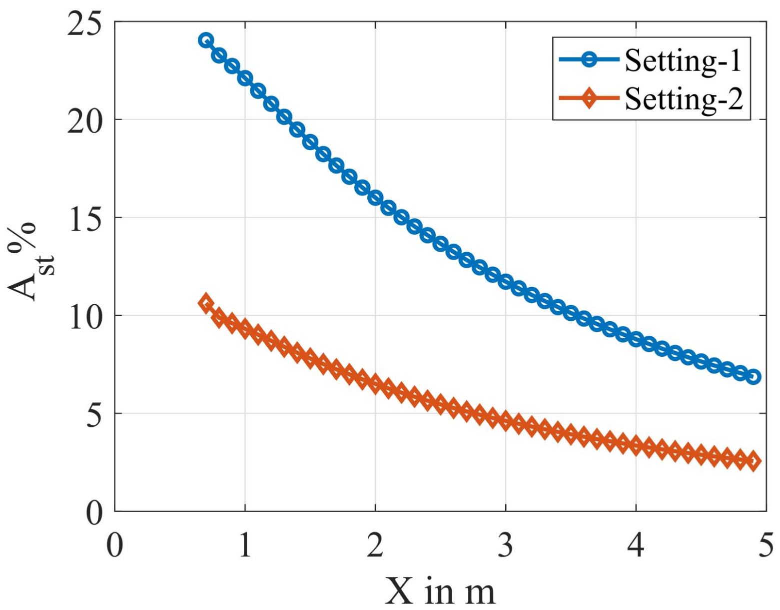

Figure 3.10: Variation of streak amplitude A_{st}% behind the scale arrays for Setting-1 and Setting-2 from X = 0.7m to X = 5.0m.

The streak amplitude behind the scale array for Setting-1 and Setting-2 is plotted in Fig.3.10. It demonstrates that the streak amplitude generated with Setting-2 is almost half that generated with Setting-1 throughout the domain.

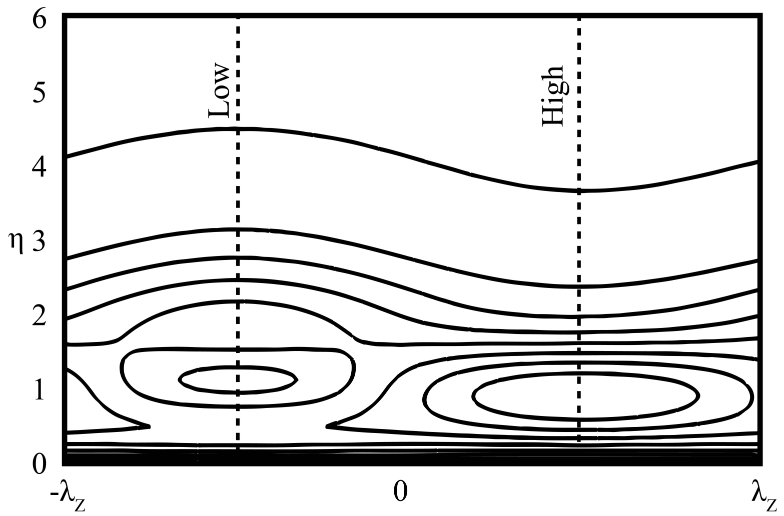

Figure 3.11: Contours of constant velocity fluctuation amplitude (streamwise component) in a cross-section at X = 2.5m for Setting-2 at f = 0.2 Hz.

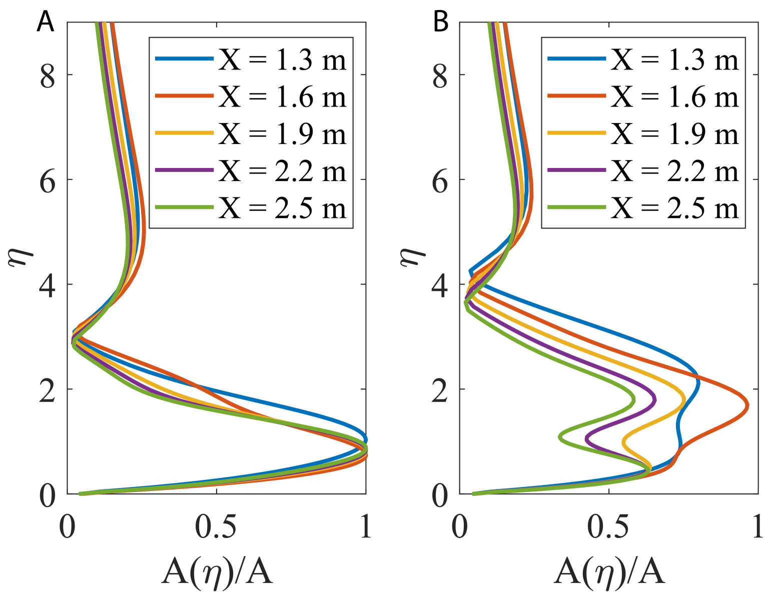

Figure 3.12: **Profiles of Velocity fluctuation (streamwise component) at different locations (X = 1.3, 1.6, 1.9, 2.2 and 2.5m) for Setting-2 at f = 0.2 Hz.** (A) y-position in the center of High-speed streak. (B) y-position inthe center of Low-speed streak.

Fig.3.11 shows the streamwise fluctuation at a plane X = 2.5m at f = 0.2 Hz and Fig.3.12 shows the evolution of streamwise fluctuation at several locations along the low-speed and high-speed locations at f = 0.2 Hz. These results are comparable in shape and structure with the experimental results reported by Fransson (Fransson et al., 2005), who used distributed roughness elements in the form of small cylindrical discs to produce a streaky flow with similar boundary conditions.

Figure.3.13 shows the streamwise velocity fluctuation integral for f = 0.1, 0.15 and 0.2 Hz. The growth of TS waves for the reference case (Blasius profile) at all frequencies reported here, correlate well within the neutral stability curve. When compared with the streaky base flow, the growth rate of TS waves is reduced for all cases except for Setting-2 at f = 0.1 Hz. Hence, it can be concluded that, at least for Setting-1 the TS wave gets attenuated for all investigated frequencies and therefore this case is clearly preferable for possibly transition delay (laminar flow control). Using the same CFD method, various streak wavelengths can be further tested which is left for future work.

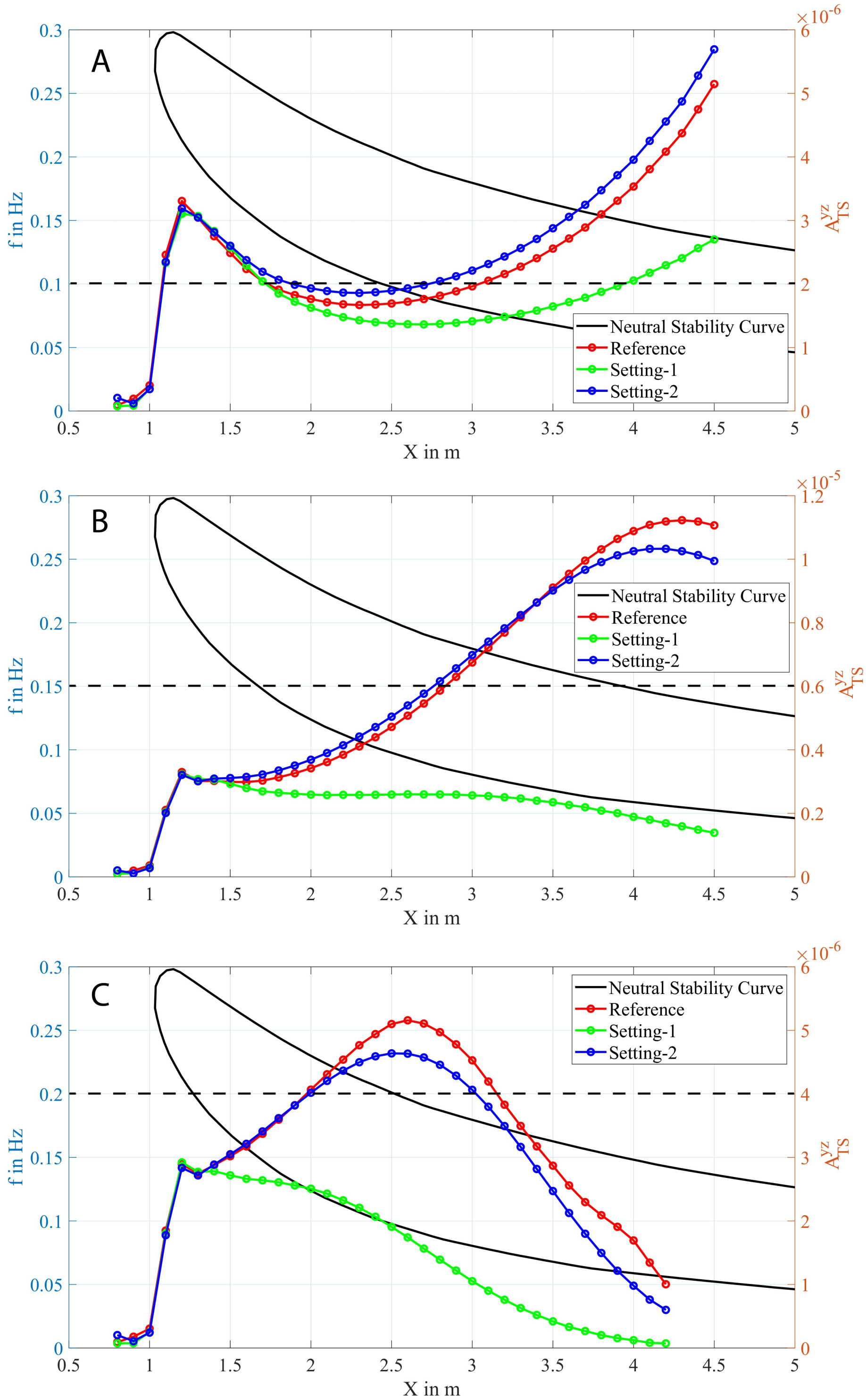

Figure 3.13: **Integral streamwise fluctuation profiles for different cases.** Red curve - Reference Blasius case, Green curve - Setting-1, Blue curve - Setting-2, (A) f = 0.1 Hz. (B) f = 0.15 Hz. (C) f = 0.2 Hz

Claim-2 *What effect could the scales-induced streaks have on the flow with pressure gradients. Is the scale structure possibly more related to flow separation control?*

The body of the bony fish studied herein is similar to an aerofoil, hence, the boundary-layer flow around the body will experience a pressure gradient, both while gliding or actively swimming. Therefore the flow is prone to possibly separate at the aft body. We expect that the observed streaky flow generation for the flat plate case is also present in the case of favorable or adverse pressure gradients and therefore could have an effect on the separation. This hypothesis was tested in a preliminary study from purely an engineering point of view (no scaling aspects were addressed). A new experiment was done to study the flow over a hydrofoil with approximately the same cross section of the investigated fish. A NACA-0020 hydrofoil was used in the experiments, which has a chord length of 150 mm and spanwise length of 342 mm. The thickness-length ratio of the foil was selected on the basis of the ratio in sea bass and carp. The experiments were conducted in a return type open surface water tunnel with a velocity range of 0.1 to 2 m/s. Flow straighteners were installed before the convergent section in the settling chamber to achieve uniform flow in the test section. The test section is 40 cm wide x 50 cm depth x 120 cm in length and transparent on all the sides to provide an optical access for flow studies. To eliminate the tip effects and enable two-dimensional flow in the center, two perspex circular discs of 400 mm diameter were attached on either end of the wing (not shown here). Two models were used, one taken as the reference plain hydrofoil and the other one covered with biomimetic fish scales (hereafter scaled hydrofoil), see Fig.3.14 . It should be noted here that the geometrical scaling of the biomimetic scales is about a factor of 5 larger than compared to the actual scales of the investigated fish (typical scale height h_s 0.5 mm in the experiment compared to about 100micron on the fish). This aspect takes into account the limits of available manufacturing methods at City during the time of the study and during the Covid period. Therefore, it was printed in larger scale to ensure a low roughness value relative to the dimensions of the scales.

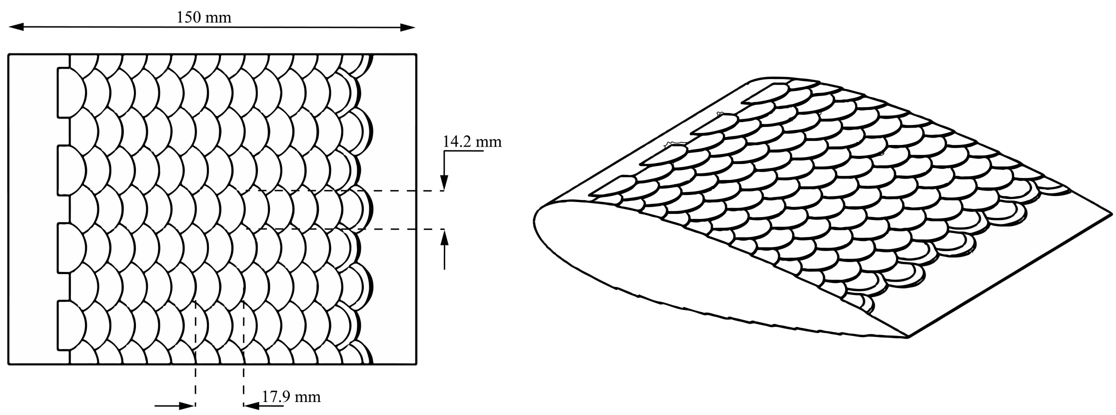

Figure 3.14: CAD drawing of hydrofoil

Figure.3.15 shows the experimental setup. Time-Resolved Particle Image Velocimetry (TR-PIV) was done at three different free stream velocities namely at U_∞ = 10, 20 and 30 cm/s (Reynolds number based on chord Re_C = 15000, 30000 and 45000) at zero angle of attack. A 3 mm thick laser light sheet was focused on the region behind the hydrofoil (in the wake region). Neutrally buoyant particles of 50 μm were introduced into the water tunnel with a suitable seeding density required for the PIV measurements. The images were captured with a Phantom Miro M310 camera at a frame rate of 250 Hz, with a pulse separation time of 2000 μs for a flow period of 4 seconds. The image frame had a pixel size of 1280 x 800 which relates to a physical dimension of 185 x 115 mm. The post-processing of PIV images was carried out using TSI Insight 4G software software with 2D cross correlation PIV algorithm applied to successive frames. The interrogation window size was 32 x 32 pixels in the first pass and 16 x 16 pixels in the final pass. Velocity vectors were validated with 3 x 3 median filter and the spurious or missing vectors were interpolated using the local mean (Raffel et al., 2007)

At the above mentioned Reynolds numbers, the flow over the plain NACA 0020 hydrofoil is dominated by boundary layer separation in the aft part because of

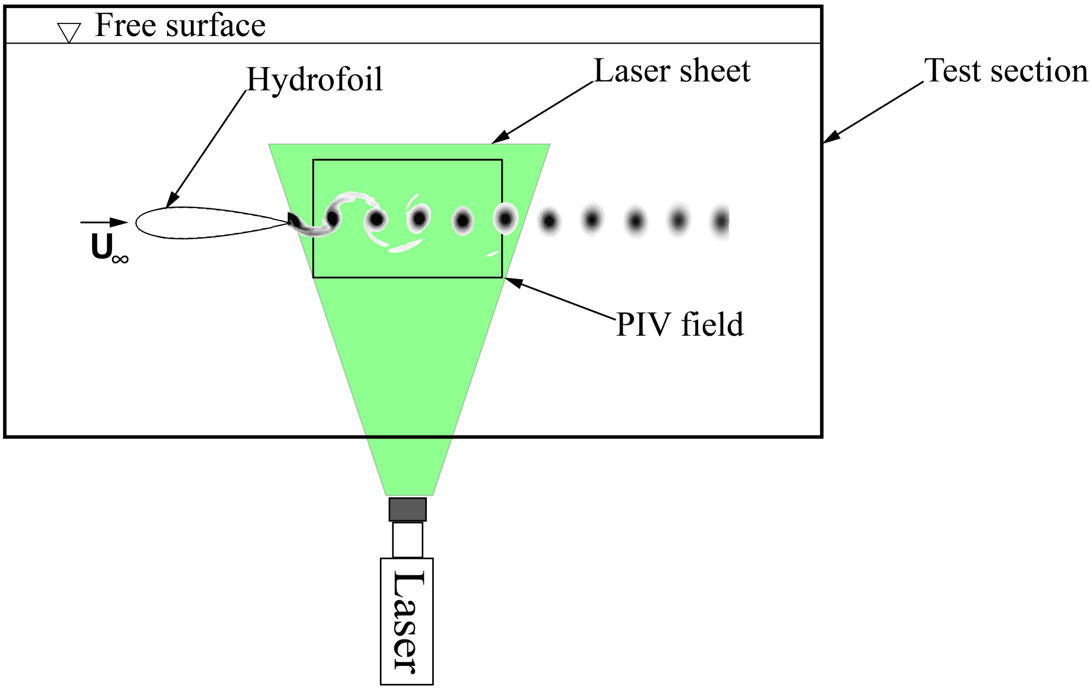

Figure 3.15: Schematic diagram of the experimental set-up. Circular End plates were used to avoid spanwise leakage flows (not shown here).

the adverse pressure gradient. The separation causes shear-layer instabilities which finally transforms the wake into a quasi-regular vortex street with rows of alternating vortices (wake mode of the hydrofoil) in the downstream direction. This quasi-periodic fluctuation process is studied by proper orthogonal decomposition (POD) to investigate the energy distribution of organized structures in the flow field. The POD modes were calculated by using the following steps (Berkooz et al., 1993). The fluctuating velocity components were calculated from each PIV frame and made into a vector form $\mathbf{u} = [u; v]$, where 'u' and 'v' are streamwise and crosswise fluctuating velocity components. All these snapshot vectors were arranged in a matrix as given in Eqn.3.6. Then the auto-covariance matrix $\mathbf{M}$ was created by using Eqn.3.7. Now, matrix $\mathbf{M}$ can be solved as an Eigen value problem, where λ and $\mathbf{A}$ are the Eigen values and corresponding Eigen vectors respectively. The Eigen values are then arranged in descending order, where the first few modes contribute to the largest

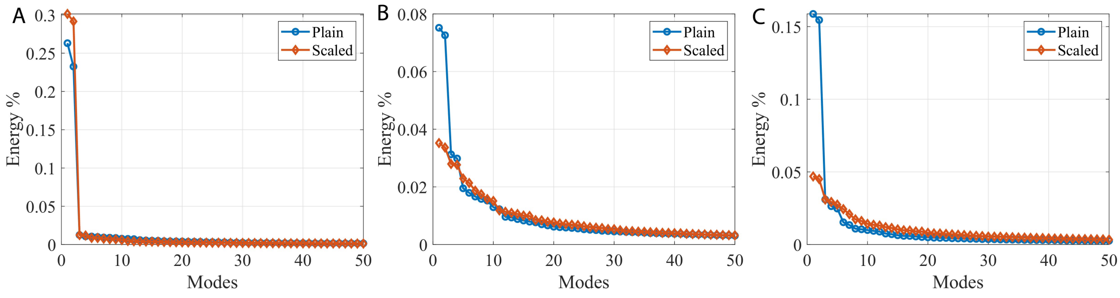

Figure 3.16: Comparison of Energy for plain and scaled hydrofoil. (A) 10 cm/s (B) 20 cm/s (C) 30 cm/s.

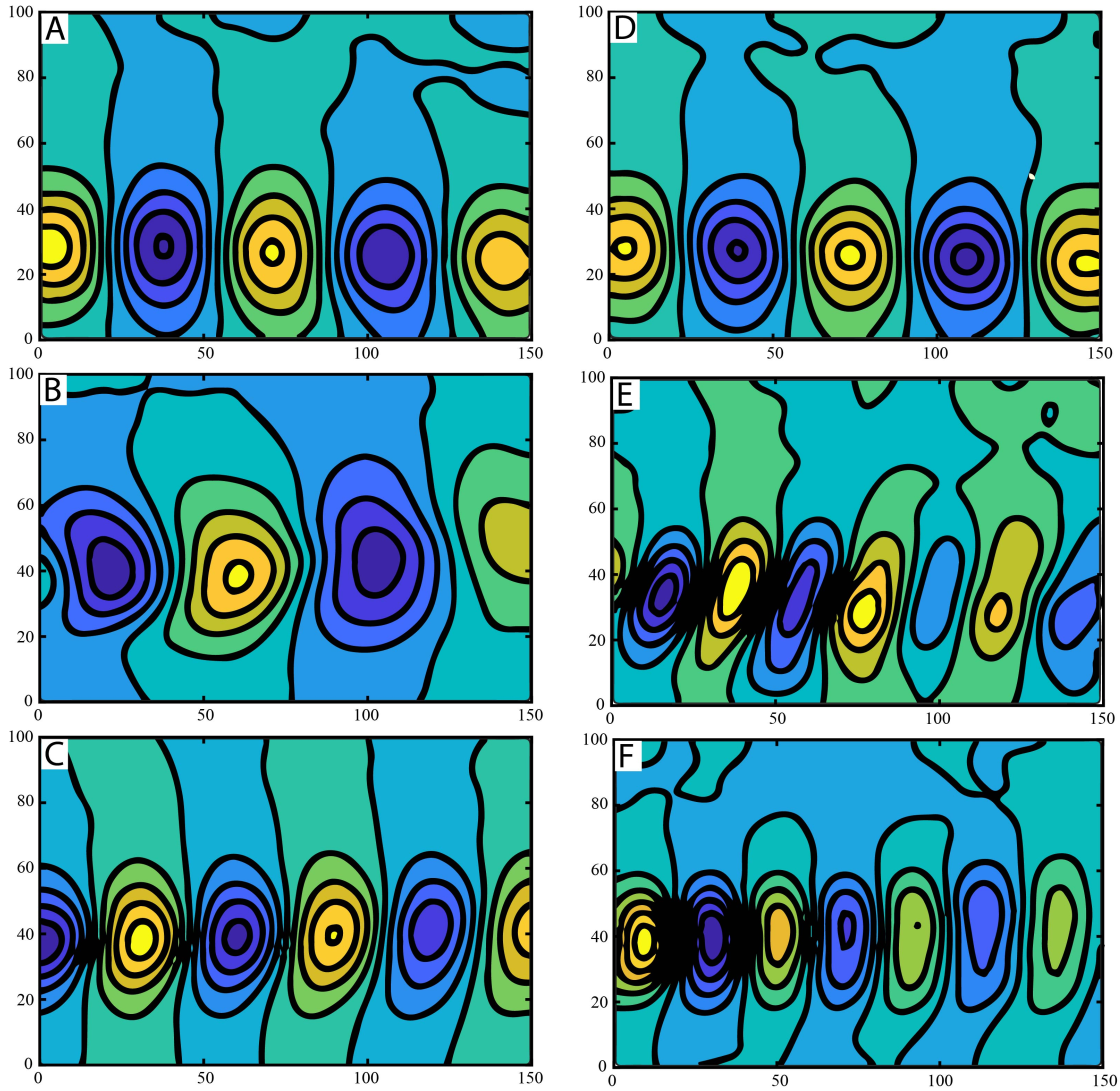

Figure 3.17: Mode-1 from cross velocity. Plain hydrofoil (A) 10 cm/s (B) 20 cm/s (C) 30 cm/s, Scaled hydrofoil (D) 10 cm/s (E) 20 cm/s (F) 30 cm/s.

energy values in the flow.

$$\mathbf{U} = [\mathbf{u}_1 \mathbf{u}_2 .... \mathbf{u}_N] \tag{3.6}$$

$$\mathbf{M} = \mathbf{U}^T \mathbf{U} \tag{3.7}$$

$$\mathbf{M}\mathbf{A}_i = \lambda_i \mathbf{A}_i \tag{3.8}$$

The Eigen vectors are used to construct the POD modes through Eqn.3.9.

$$\phi_i = \frac{\sum_{n=1}^{N} A_{i,n} \mathbf{u}_n}{\left\| \sum_{n=1}^{N} A_{i,n} \mathbf{u}_n \right\|}, \; i = 1, 2....N \tag{3.9}$$

Fig.3.16 displays the result from POD on the plain and scaled hydrofoil for all the investigated cases. At 10 cm/s, the energy distribution and mode structure are similar for the plain and scaled hydrofoils as shown in Figure.3.16A. The highest values of energy are contained in the first two modes, and the displayed mode shape (Mode-1) using the cross-velocity component is similar in structure for both these modes, refer Fig.3.17A and Fig.3.17D. For higher Re flows, the energy distribution changes in magnitude and dominant modes. The dominant modes for the scaled hydrofoil cases have lower energy as shown in Figure.3.16B and Figure.3.16C. In addition, for the plain hydrofoil case, the first mode remains similar to the lower Re case with clear alternating velocity fields (see Fig.3.17B and Fig.3.17C). However, for the scaled hydrofoil, the dominant POD mode has a higher wave-number and shows a lower coherence in the streamwise direction.

The power spectrum at 30 cm/s using the cross-velocity behind the scaled hydrofoil

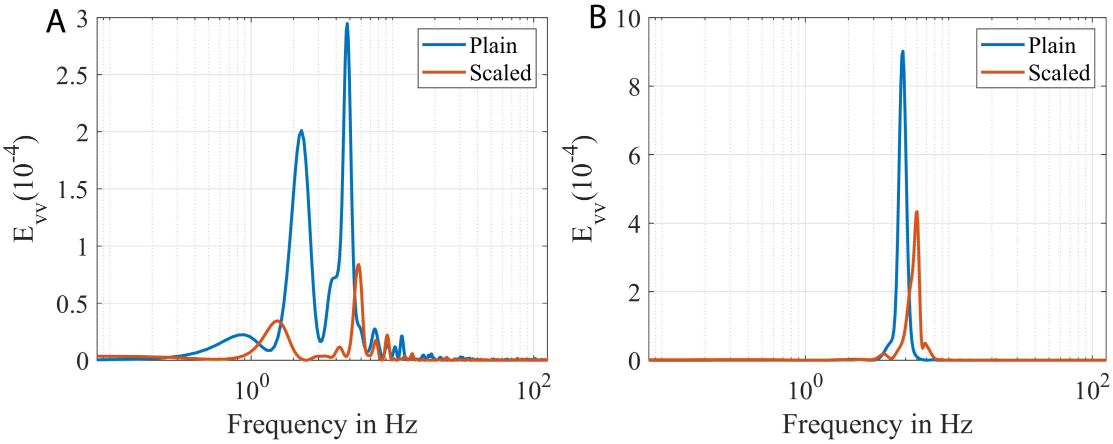

Figure 3.18: **Power spectrum for plain and scaled hydrofoil at $U_\infty = 30cm/s$** (A) spectrum from cross velocity behind trailing edge of hydrofoil. (B) spectrum for POD mode-1.

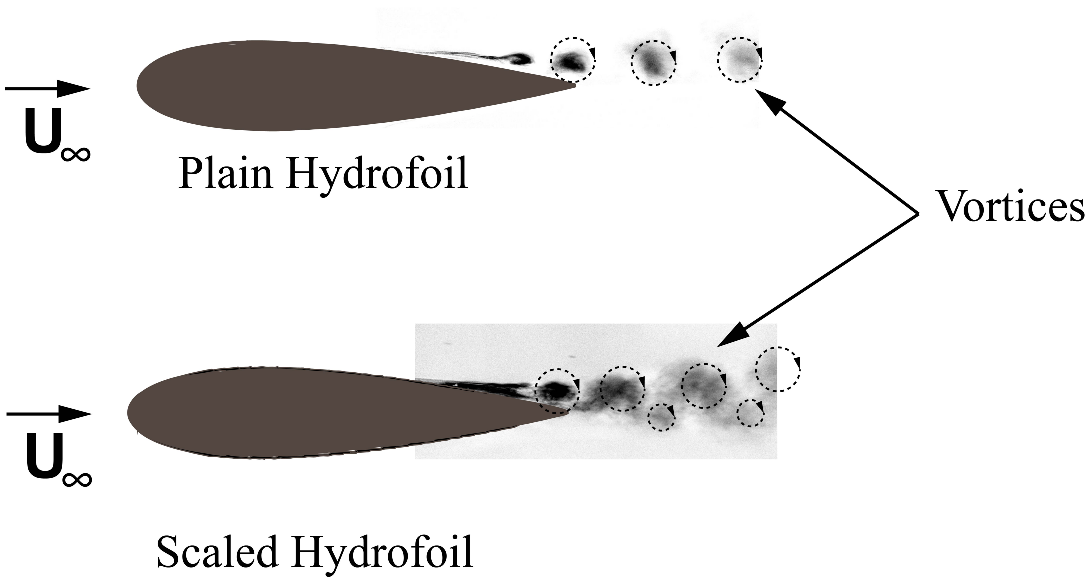

Figure 3.19: Flow visualisation results for Plain hydrofoil (top) and Scaled hydrofoil (bottom) at $U_\infty = 30cm/s$.

(just behind the trailing edge) case is given in Fig.3.18A. The plain hydrofoil has a dominant frequency (f_0) at about 5 Hz and also a subharmonic peak at 2.5 Hz. The Strouhal number ($St = f_0 D/U_\infty$) defined with the dominant peak (f_0) is $St \simeq 0.5$, where 'D' is the thickness of the hydrofoil. This Strouhal number value and the sub-harmonic peak are comparable with the results mentioned for vortex shedding behind symmetric aerofoils at similar Reynolds numbers (Yarusevych et al., 2009).

For the scaled hydrofoil, the dominant peak has a magnitude of only about 30% when compared to the plain hydrofoil, which is similar to the magnitude obtained from the spectrum using the first POD mode. This indicates that the energy in the cross-velocity fluctuations have been largely reduced by the effect of the scales. It is observed that the shedding frequency also has slightly increased (dominant frequency $f_0 \simeq 6Hz$ and $St \simeq 0.6$). Note that, this result represents only the flow in a single plane behind the hydrofoil (at the low-speed location) and more information needs to be taken at different planes to get a better picture of the 3D structure of the wake.

First indicative studies on the flow structure using flow visualisation were done using pottassium permanganate to identify the coherent structures which were formed on one side of the hydrofoil. Therefore, the flow structures in the wake seen by the visualization represent only one part of the vortex street. Typical flow visualisation images for the plain and the scaled hydrofoil cases are shown in Fig.3.19 for 30cm/s. Both images were taken from phase-synchronized snapshots of the quasi-periodic shedding process and processed as an average over 8 vortex shedding cycles. For the plain hydrofoil case, the coherence of the flow structures is clearly identified by the dark concentrated patches of dye. However, for the scaled hydrofoil case, the dye is spread over in a staggered arrangement which results from the streaky base flow on the hydrofoil. Note that, the visualization image represents an integration of the scattered light over a certain depth of field in viewing direction, therefore averaging the results over the depth.

Inference from the experiments

The PIV results from the flow over plain hydrofoil at low Reynolds numbers are comparable with the literature in terms of the Strouhal number and the sub-harmonic frequency peak (Yarusevych et al., 2009), therefore the results are valid and are considered as a baseline case. To compare the results between plain and scaled hydrofoil cases, the ratio between the boundary-layer thickness (δ) to maximum scale height h_s ratio will be used. At low Reynolds number (Re = 15000), the boundary-layer thickness will be around 3mm where the scale array starts (using flat plate boundary-layer thickness formula), giving a δ/h_s ratio of 6. However, the scale array is placed in the adverse pressure gradient region as seen in Fig.3.14. Hence, the streak amplitude will not be strong enough to create a spanwise modulation of the flow. It is assumed that this is the reason why the energy from POD modes are nearly equal, as seen from Fig.3.16A. As the Reynolds number increases the δ/h_s ratio decreases to produce higher streak amplitudes ($\delta/h_s \simeq 4$ for Re = 30000 and $\delta/h_s \simeq 3$ for Re = 45000). For these cases, the relative energy is clearly reduced when compared with the plain hydrofoil case (see Fig.3.16B and Fig.3.16C). Also for Re = 45000 case, the integral energy is lower than that of the plain hydrofoil case as seen from the spectrum plots (Fig.3.18A). Therefore, it can be hypothesized that once the Reynolds number crosses a particular value, the scales produce streaks of sufficient amplitude to modify the flow separation process. Further experiments are needed to explore the flow physics in detail.

Future work

The following points are worth considering for possible future works.

- **Critical Reynolds number.**

  The scale array used in the presented study showed the effective means to prolong laminar flow by attenuating the fundamental TS-waves. However, the scales also represent a hydrodynamic roughness. Any roughness element which operates beyond a certain Reynolds number will trigger transition even without any external disturbances. The limiting Reynolds number where the flow changes quickly from laminar to turbulent is known as the critical Reynolds number. Based on the aspect ratio of the roughness element, the Reynolds number and the boundary layer to roughness height ratio, the element can induce symmetric or antisymmetric unstable modes (Puckert and Rist, 2018). Therefore, further parametric studies of different scales of the biomimetic surface and Reynolds-numbers should be continued to explore the range of effective transition delay using such surfaces.

- **Influence of pressure gradient in transition.**

  Adverse pressure gradients are known to destabilize the laminar flow by amplifying the TS wave instabilities and vice versa (Schlichting and Gersten, 2017). Therefore, the scales should be investigated further in a controlled experiment with well defined pressure gradient. This could be done with a flat plate configuration with additional displacement body to impose a pressure gradient.

- **Possible importance of flexibility of the scales.**

  During the microscopic examination of the scales on sea bass, it was observed that, when the fish body is bent, the scales on the convex part tend to increase the surface roughness by the relative movement between each other, possibly increasing the step-height in the central and overlap regions. Hence, there could also exist another passive but adaptive flow control effect such as to increase the streak amplitude in order to support the boundary layer to remain attached or to trigger transition.

- **Dynamic flow conditions.**

  All the results reported in this thesis were obtained under steady inflow conditions. In reality, fishes move their body by undulating their tail and body in a dynamic manner which can change the boundary layer properties (Kunze and Bruecker, 2011). Therefore, it is necessary to study the behaviour of the flow over biomimetic scale array with dynamic flow conditions.

Chapter 4

Flow turning effect and laminar control by the 3D curvature of leading edge serrations from owl wing

Abstract

This work describes a novel mechanism of laminar flow control of straight and backward swept wings with a comb-like leading edge device. It is inspired by the leading-edge comb on owl feathers and the special design of its barbs, resembling a cascade of complex 3D-curved thin finlets. The details of the geometry of the barbs from an owl feather were used to design a generic model of the comb for experimental and numerical flow studies with the comb attached to the leading edge of a flat plate. Due to the owls demonstrating a backward sweep of the wing during gliding and flapping from live recordings, our examinations have also been carried out at differing sweep angles. The results demonstrate a flow turning effect in the boundary

layer inboards, which extends downstream in the chordwise direction over distances of multiples of the barb lengths. The inboard flow-turning effect described here, counter-acts the outboard directed cross-span flow typically appearing for backward swept wings. This flow turning behavior is also shown on SD7003 airfoil using precursory LES investigations. From recent theoretical studies on a swept wing, such a way of turning the flow in the boundary layer is known to attenuate crossflow instabilities and delay transition. A comparison of the comb-induced cross-span velocity profiles with those proven to delay laminar to turbulent transition in theory shows excellent agreement, which supports the laminar flow control hypothesis. Thus, the observed effect is expected to delay transition in owl flight, contributing to a more silent flight.

4.1 Introduction

One of the remaining puzzles in the silent flight of owls is the function of the serrated leading edge. This 'comb-like' structure is more developed in nocturnal than diurnal owl species (Weger and Wagner, 2016), suggesting that the leading-edge comb must have some benefit for hunting in the night. Indeed it was suggested early on (Graham, 1934; Lilley, 1998) that the serrations are one of the adaptations found in owls that underlie silent flights, where the owl needs to be as quiet as possible when hunting nocturnally. Acoustic measurements by Neuhaus et al. (1973) and Geyer et al. (2020) support this suggestion, although the effect was marginal for low angles of attack, the situation being relevant for the gliding phase persisting up to the final phase of direct attack of the prey. Alternative suggestions for their function were focusing on a possible aerodynamic benefit of a serrated leading edge (Hertel, 1963; Kroeger et al., 1972; Klän et al., 2010; Winzen et al., 2014; Wagner et al., 2017; Rao et al., 2017; Ikeda et al., 2018; Wei et al., 2020), summarized in the most recent review given in 2020 by Jaworski and Peake (2020).

An early contribution interpreted the leading edge comb as a tripping device, which triggers the boundary layer to turbulent transition, keeping the flow over the aerofoil attached (Hertel, 1963). However, this would cause some extra turbulent noise, which is not observed (Geyer et al., 2020). Kroeger et al. (1972) presented a comprehensive study of the flow around the leading edge of an owl wing. Using wool tufts, these authors showed a spanwise flow behind the comb, which they interpreted as a way to prevent flow separation. Acoustic measurements by these authors, however, showed no direct influence of the presence of the comb. It was only at high angles of attack that a difference of about 3 dB was noticeable. This result was later confirmed by Geyer et al. (2020) using acoustic 2D sound maps. These authors could show that the sources of higher noise levels for high angles of attack stem from the wing tip. Jaworski and Peake (2020) speculated that the leading edge comb may play a role in reducing spanwise flow variations due to separation at high angles of attack ($\alpha = 24°$, in Geyer et al. (2020)), thereby reducing the strength of the tip vortex and the associated tip noise (Jaworski and Peake, 2020). If so, it would, however, not be relevant for the gliding phase.

In a similar way, aerodynamic performance measurements on wings with serrated leading edge show benefits mostly with increasing angle of attack, again not much relevant for the gliding phase. Rao et al. (2017) showed that planar leading-edge serrations can passively control the laminar-to-turbulent transition over the upper wing surface. Each of the serrations generates a vortex pair, which stabilizes the flow similar as vortex generators do. Wei et al. (2020) applied such serrations on a UAV propeller to shift the location of laminar-to-turbulent transition on the suction side. Ikeda et al. (2018) investigated different length of the serrations to find the optimum of lift-to-drag ratio at angles of attack $< 15°$.

A remaining contribution to noise reduction at gliding flight conditions may be the influence of the comb on leading-edge noise from incoming vortices and unsteady flow components present in the air environment. To test this hypothesis, researchers investigated the noise emission of wings in an anechoic wind tunnel with unsteady inflow conditions generated by an upstream inserted turbulence grid Geyer et al. (2017). The results showed that serrations can attenuate unsteady flow effects caused by oncoming vortices and turbulence. Similar results were found from LES simulations of serrations in turbulent inflow conditions (Chaitanya et al., 2017). These findings agree with measurements on noise emission of stationary aerofoils where artificial serrations led to a lower noise radiation in unsteady flow (Geyer et al., 2017; Narayanan et al., 2015).

Herein, we introduce a novel hypothesis which is related to the influence of serrations on swept wing aerodynamics. First, data of owls in gliding flight clearly demonstrate that the leading edge of the handwing is swept backward, about 10–20°, see Figure 4.1 (adapted from snapshots of the movie produced in Durston et al. (2019) for a gliding American barn owl). Second, the serrations in nature are curved in a complex 3D shape protruding out of the plane of the wing (Bachmann and Wagner, 2011). All of this may influence the flow over the wing and probably - by the complex coupling between flow and sound generation - it may influence also the overall noise emission. For swept wings it is known that a backward sweep can introduce considerable crossflow instabilities, which trigger transition (Serpieri and Kotsonis, 2016; Radeztsky et al., 1999; White and Saric), invoking the substantially drag-increasing turbulent boundary-layer state (Wassermann and Kloker, 2002). To overcome this drag penalty, flow control methods such as suction (Kloker, 2008) and plasma actuators (Dörr and Kloker, 2015) have been developed to attenuate the instabilities. The present work demonstrates, that a similar effect may be achieved in a passive way by using a comb-like leading-edge structure with 3D curved finlets, inspired from the geometry of serrations on the owl wing. We show in the following that the serrations cause a change in flow direction near the surface of the wing model (flow turning) at sweep angles observed in nature, thereby delaying transition and hence, could be a contributing factor to a more silent flight.

4.2 Methods

4.2.1 Coordinate System of the wing

The world coordinate system of the flying body is typically defined in relation to the body axes and the direction of the flight path. Herein, we define (in capital letters) another Cartesian coordinate system which is fixed with the wing and oriented with the leading edge, see Fig. 1. The positive X-axis points in chordwise direction, the positive Y-axis vertically upwards, and the positive Z-axis is aligned with the leading edge of the wing (Fig. 4.1).The same coordinate system was used to describe the morphology of the leading edge comb of the owl feather in nature and for the model data, see Table 4.1. Often a flat swept plate is chosen as a research platform for swept wing instabilities. This is due to the better control of the boundary conditions and access for measurement methods (Abegg et al., 2001). Additional wing curvature effects on laminar-turbulent transition can also be simulated on a flat plate, by imposing either a negative or a positive pressure gradient on the potential flow outside, which is typically done by using a displacement body (Abegg et al., 2001). However, for this study a swept flat plate with no additional pressure gradient is used.

4.2.2 Generation of the generic comb model

As may be seen in Fig. 1b, the feather that forms the leading edge has an outer vane with separated, filamentous barb endings. These barb endings are the serrations (Bachmann and Wagner, 2011). Many parallel serrations form a leading edge comb-like structure. Each single serration has a complex shape with strong curvature in

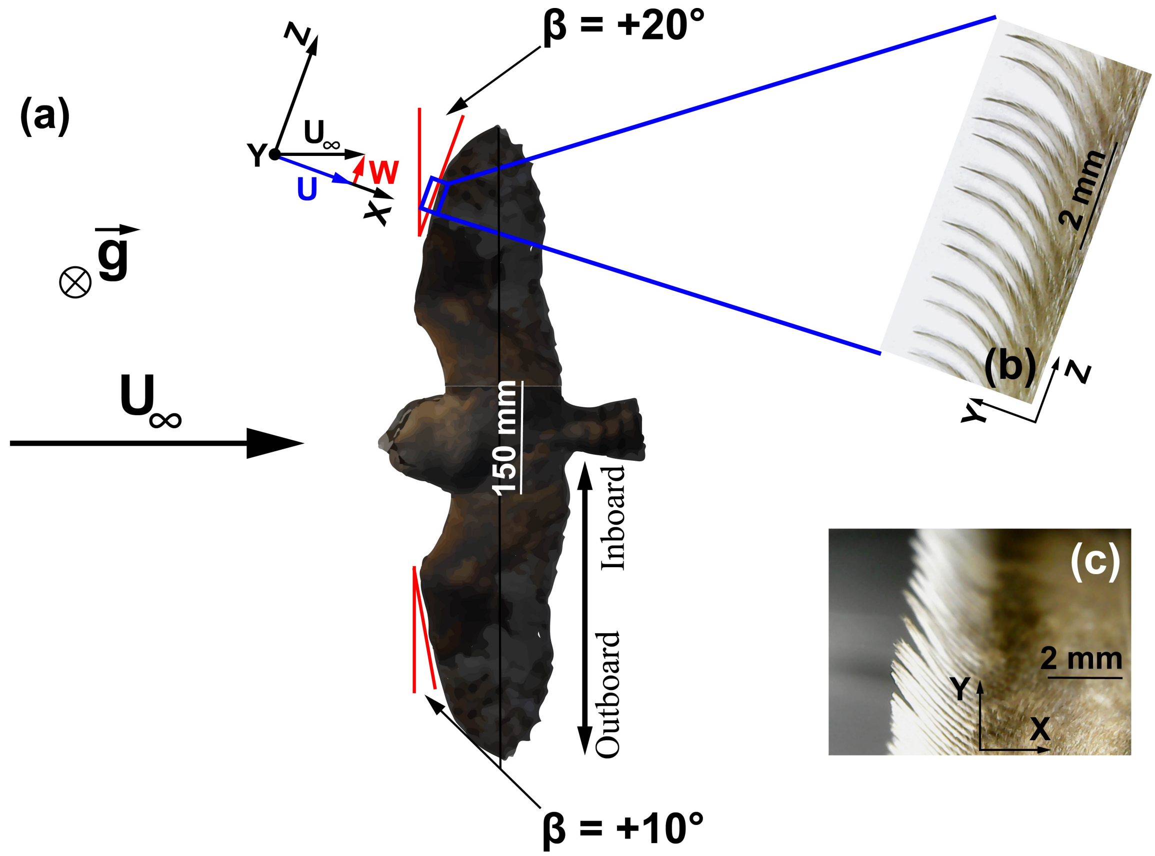

Figure 4.1: Gliding owl and leading edge serrations. a) Top view of an owl in gliding flight, illustrating the backward sweep of the wing. The situation is shown in a body-fixed observer situation with wind coming from left at a velocity (U_∞). The wing portion at mid span has an effective positive sweep angle of $\beta \approx 10°$, increasing to $\beta \approx 20°$ further towards 3/4 span. The picture of the owl is reproduced/adapted from the video published in (Durston et al., 2019) with permission from Journal of Experimental Biology, reference (Durston et al., 2019) with DOI: 10.1242/jeb.185488. Inset b) pointed picture of leading edge comb in back view with flow coming out of the paper plane; inset c) pointed picture of side view of the serrations with flow coming from left .

two major planes of the feather, the frontal Y-Z plane and the cross-sectional X-Y plane (Bachmann and Wagner, 2011).

A generic model of the leading edge comb was built based on data available in (Bachmann and Wagner, 2011). The model consists of a series of barbs. Each barb starts with the root and ends with the tip. While the roots of the serrations are connected to each other, the tips are separated. In the following we first describe

Nomenclature	**Barn owl data**	**Idealized model**
Length (μm)	1823 – 2716	1840
Wavelength (μm)	490 – 670	500
Width (μm) @ tip	157 – 215	250
Width (μm) @ root	528 – 652	500
Thickness (μm) @ tip	46.9 – 53.9	50
Thickness (μm) @ root	82 – 87.2	= plate thickness
Tilt Angle (°)	35.3 – 36.7	37.5
Average Inclination Angle (°)	50	55.8
Angle LE / flight path (°)	106 – 138	90 – 110

Table 4.1: Dimensions and key geometric parameters of the idealised modeled barb element, leaned upon measurements on barn owls presented by Bachmann and Wagner (2011).

the properties of the single barbs in more detail, before we explain how the barbs are aligned to form a leading-edge comb.

Table 4.1 indicates the range of values for the key geometric parameters of measured barbs found from the barn owl in nature, comparing those with the selected parameter of our generic model, following the data provided in (Bachmann and Wagner, 2011). The definition of the geometric parameters is illustrated in Fig. 4.2. The width is the extension of the major axis of the barb and the thickness is the extension of the minor axis of the barb. The inclination angle is defined herein between the barb's base and the Z-direction in the X-Z plane (Fig. 4.2c). The tilt angle is the angle between the barb's tip and the base in the Y-Z plane (Fig. 4.2b). The height and the length of the barb is referred to as H and L as illustrated in Fig. 4.2.

The software SolidWorks (Dassault Systèmes, France) was used to design a synthetic barb in the form of a beam with elliptical cross-section (long axis: width, short axis: thickness) and a linear taper from root to tip (root width: 500 μm, thickness: plate thickness; tip: width: 250 μm, thickness: 50 μm) (see Tab. 4.1) . The length of the initially straight beam was 2250 μm. The elliptical beam was first twisted by 30°

(see stagger angle in Fig.4.3b, then tilted in the X-Z plane and finally curve-bent in the X-Y plane to reach the desired angles of tilt and inclination given in Tab.4.1.

In a second step, the root of the beam was then smoothly integrated into the elliptical nose of the flat plate (aspect ratio of about three, thickness of the plate: thickness of the barb at the root) to form the serrated leading edge comb. The comb was built as a row of successive barbs with the same spacing (wavelength λ = 500 μm) and size. The back, side and top views of the recreated leading edge comb is shown in Fig. 4.2. A final qualitative check was done with the geometry of a digitized piece of a 10$^{\text{th}}$ primary feather of an American barn owl (*Tyto furcata pratincola*). The generic model resembled the natural geometry well in all major details of the barb's 3D shape, compare Fig. 4.1a,b and 4.2b,c.

In the following, we interpret the comb as a cascade of blades following the classical nomenclature used in the field of turbomachinery. Each blade is represented by one barb and the cascade blade spacing is equal to the comb wavelength. According to this, we can define the stagger angle as the angle between the chord line of the barb and the axis normal to the leading edge (LE) in the X-Z plane (Fig. 4.3a) (Dixon and Hall, 2014). Cross-sectional views of individual barbs along the root, middle and tip locations are shown in Fig. 4.3a. The stagger angle is about 30° at the root of the barb and decreases to zero at the barbs' tip. Also, the chord decreases along the barbs' height, hence, with same spacing the spacing to chord ratio increases from root towards the tip as shown in Fig. 4.3b.

4.2.3 Numerical Flow Simulations

American barn owls have an average wing chord length of C_W = 0.178 m (Klän et al., 2009) and are supposed to fly with velocities of U_∞= 2.5 m/s to 7 m/s (Bachmann et al., 2012), a number derived from data on European barn owls (Mebs and Scherzinger, 2000). At these velocities the Reynolds number Re_{wing}, defined with the

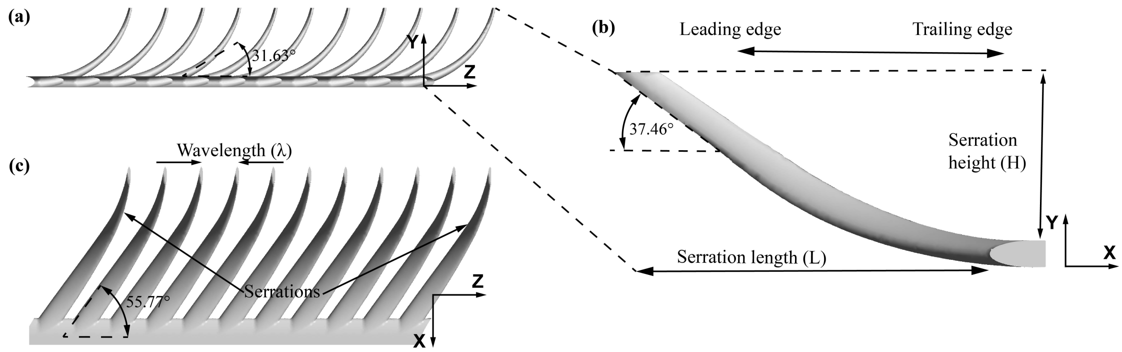

Figure 4.2: Orientation of the reconstructed serrated leading edge. a) back-view of the comb, looking from the back over the feather onto the outstanding barbs of the right wing, compare also Fig. 1b. b) Side view on a single barb in enlarged scale showing the tilt angle (37.5°) c) top-view of the comb in the feather plane, showing the inclination angle (55.8°) of serrations along the spanwise direction.

wing chord C_W, ranges between 30,000 and 100,000, if air temperatures are between 10°C and 20°C. All the simulations and the flow visualisation in the work refer to an average flight speed of 5m/s, which lies within the specified flight-velocity range. For the corresponding Re_{wing} of 60,000 the boundary layer is in the transitional regime to turbulence, where growing instabilities have an important contribution on noise production. Therefore, any possible means to manipulate the flow at or near the leading edge to delay transition may have consequences on the overall flow and acoustic characteristics of the whole wing. For our studies, we consider the situation of the animal in gliding flight at constant speed within an otherwise quiescent environment. Therefore, we can chose steady in-flow conditions. For the first 10 percent chord of the wing including the barbs on the leading edge, the flow is expected to remain laminar and steady. As the barbs have a tiny filamentous shape with a diameter of only few tenth of micron, the local Reynolds-number (built with the chord of the barb) falls around 50, which is small enough that no vortex shedding will occur, see the work of (Paul et al., 2014) for elliptic cylinders. These conditions pave the way to use a steady-state flow solver in Computational Fluid Dynamics (CFD) to investigate the flow behind the serrations. Numerical simulations were carried out using ANSYS-Fluent 19.0. The wing-fixed coordinate system as defined in Â§4.2.1

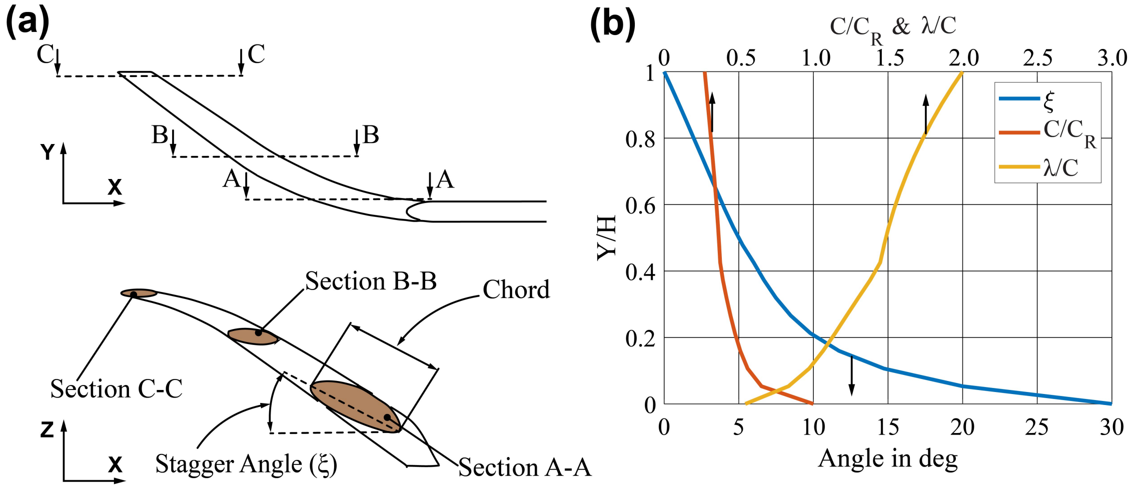

Figure 4.3: Serration drawings and plots a) Single barb with three sections showing the cross-section twist, where section A-A is the cross-section near to the root of the barb, section B-B is the cross-section at the mid-point of the barb and section C-C is the cross-section at the tip of the barb. b) Stagger angle (ξ), Normalised chord (C/C_{Root}) and spacing to chord ratio (λ/C) with normalised height of serration

is used to analyze the data. The computational domain extends six serration lengths upstream and downstream along the X-axis, from the leading edge of the flat plate where the serrations were attached. Similarly, the domain length in wall-normal direction (Y-axis) extends five serration lengths in either direction and the span-wise direction (Z-axis) has a length which accommodates 11 serrations as shown in Fig.4.4a. The domain is meshed with tetrahedral elements with inflation layers near the serrations, furthermore, the mesh was refined near the serrations to capture the flow gradients accurately, the mesh is shown in Fig.4.12 and the reported results are mesh independent (see Appendix-A). Computations were performed with a steady-state solver and the $k-\omega$ model for solving the RANS turbulence equations. At the inlet a constant free stream velocity (U_∞) is assumed. The direction of this velocity vector relative to the coordinate system of the wing and the leading edge indicates whether the flow is facing a swept wing or not. Zero sweep means that the leading edge is aligned with the outboard directed spanwise axis of the flying body and the inflow velocity vector is parallel to the chord-wise axis of the wing ($\beta = 0°$ relative to

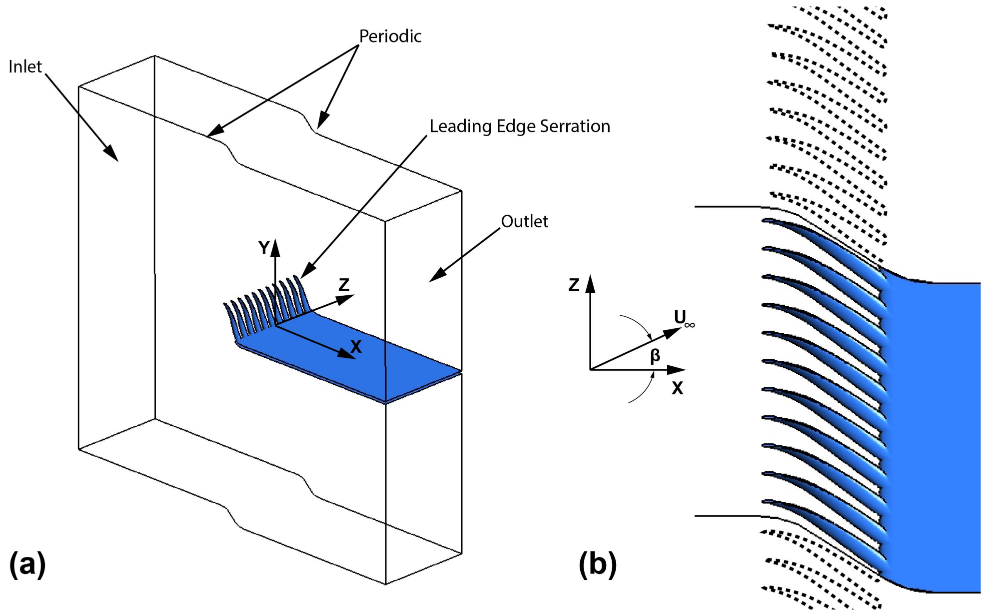

Figure 4.4: Sketches of the CFD domain and the flow configuration with respect to the comb. (a) Isometric view of the CFD domain with periodic conditions in Z-direction. Leading edge serrations attached with the flat plate is shown in blue colour surface (b) Enlarged view of leading edge serration in the X-Z plane showing the direction of the inlet flow velocity vector (U_∞) at an angle (β) (sweep angle) with X-axis. (Hidden lines of the serration are indicating the periodic boundary condition)

the X-axis in the X-Z plane) as shown in Fig. 4.4b. To simulate the sweep effect of the wing, the angle β was varied from -10° (forward swept wing) to +20° (backward swept wing). Constant pressure was assumed at the outlet and periodic boundary conditions were given at the lateral sides, which results in infinite repetitions of the serrations (neglecting end effects).

4.2.4 Flow Visualization

For the experimental flow studies, the model of the flat plate with the leading-edge comb was 3D printed with a 20:1 upscaling factor (Stratasys OBJET 30 PRO printer with a print accuracy of 30 microns, material Veroblack). Fabrication of the serrations in their original size was discarded after testing different micro-manufacturing

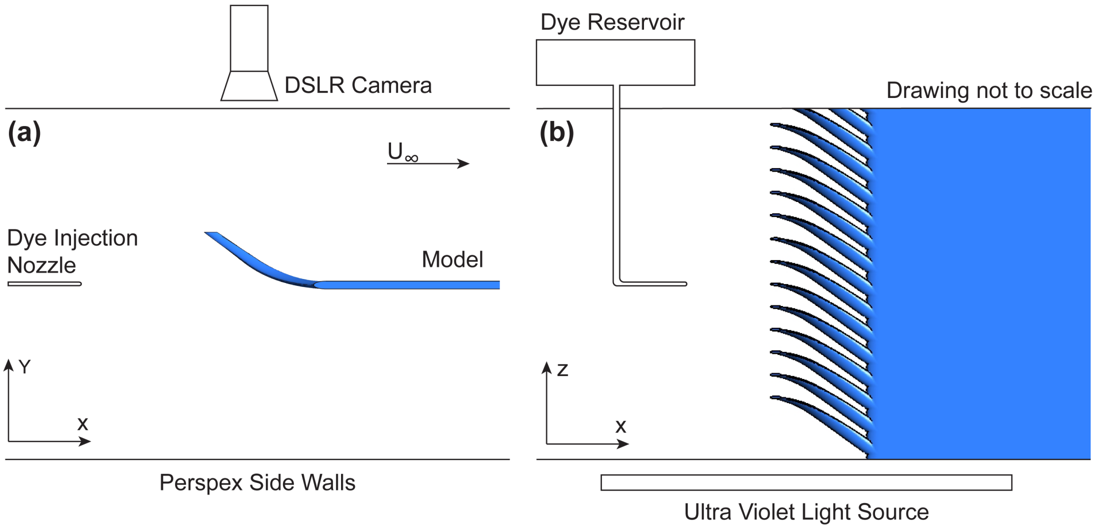

Figure 4.5: Sketches of the experimental set-up for the dye flow visualizations carried out in the CHB Water Tunnel at City, University of London. (a) plan view of the set-up in the horizontal cross-section. (b) Side view on the vertically mounted flat plate.

methods showed extreme difficulties in order reproduce the shape of the barbs in a high quality. Hence they were up-scaled and by the method of dynamic similitude in fluid mechanics (Durst, 2006), the flow conditions could be matched to the simulations with the use of the CHB Water tunnel facility at City, University of London. The tunnel is a closed loop, open surface tunnel which operates horizontally with a 0.4 m wide, 0.5 m deep and 1.2 m long test section. According to the laws of similitude, the freestream velocity of the water was set to 3.3 cm/s, corresponding to the situation of 5 m/s in air with the serration in original scale. The leading edge of the up-scaled model was placed vertically in the tunnel, at an angle of attack $\alpha = 0°$, 0.4 m downstream of the entrance of the test section, extending from the floor of the tunnel up to the free water-surface (Fig. 4.5). This situation reproduces the flow along the flat plate with zero sweep of the leading edge. Fluorescent dye was injected through a small needle (1 mm inner diameter, 1.6 mm outer diameter) which was placed upstream of the model (Fig. 4.5b) and in a Y position such that the dye streamline was just on the surface of the model. Care was taken to control the dye exit velocity the same as the bulk fluid flow. This is crucial to avoid instabilities of the fine dye streakline ultimately compromising the result (Merzkirch, 2012). An ultra-violet (UV) lamp was placed underneath the perspex floor of the test section to enhance the contrast of the fluorescent dye against the background. A NIKON D5100 DSLR camera was used to capture the resulting flow visualization (Fig. 4.5a). The camera was mounted on a tripod and was situated parallel to the surface of the model, to observe the evolution of the dye filament on the surface of the model. Due to the low light level, a long exposure (20 seconds) image was taken with the lens aperture set to f/10. Such a long-time exposure is allowed as the flow pattern remained stationary, indicating a steady flow situation. The images were then subsequently enhanced using 'Adobe Photoshop' to provide better clarity.

4.3 Results

In the following we present both experimental and simulation data on a new hypothesis on the function of the serrated comb of the leading edge of the owl wing. The new hypothesis states that the 3D curvature of the serrations cause a change in the direction of the flow. The flow is turned inboards towards the owl's body (called "flow turning" in the following), in this way it counteracts the outboards directed cross-span flow induced by the backward sweep of the wing. We first show the basic predictions of our model and the validation of these predictions by experiments in a water tunnel. In a second part, we examine the properties of the flow turning in more detail.

4.3.1 Basic results of experiments and CFD simulations

Figure 4.6 shows the streamlines (Fig.4.6a experiment, Fig.4.6b computed from the steady state CFD simulation), upstream of the serrations to downstream of them.

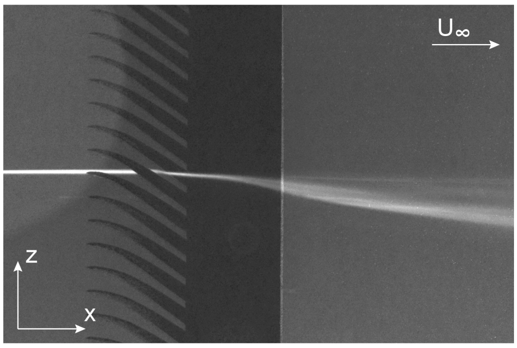

(a) Long-time exposure image of the dye flow visualisation, illuminated under ultra violet light (image has been contrast-enhanced for better clarity).

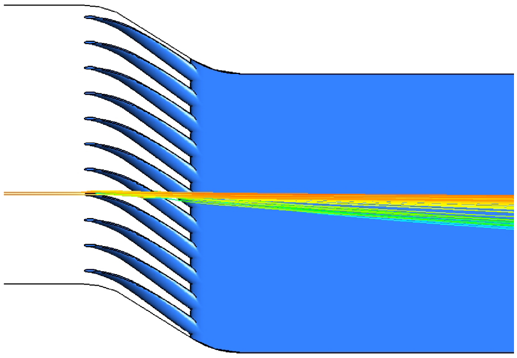

(b) Top view on streamlines with different starting points along the wall-normal axis in color (green: near-wall to red: tip of the serrations, CFD simulation at $\beta = 0°$).

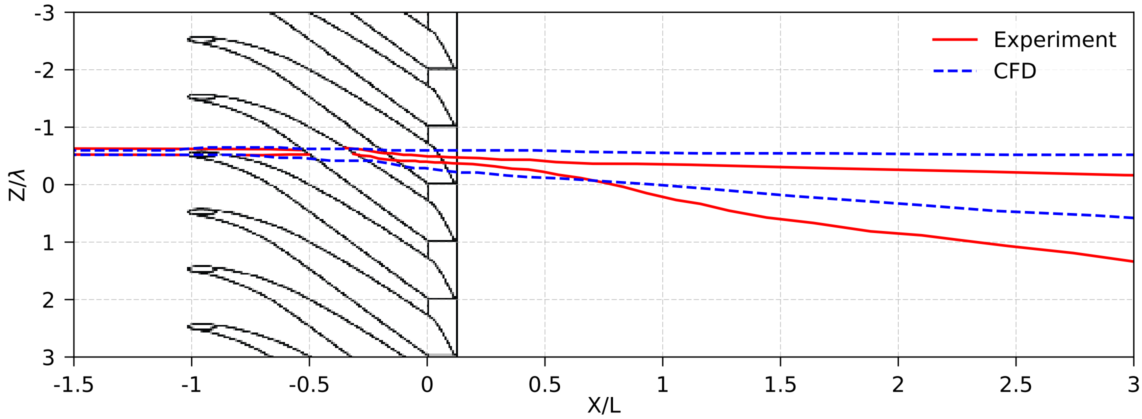

(c) Range of the most-extreme turning streamline relative to the streamline at the tip. From the CFD simulation and the dye trace from the water tunnel experiment

Figure 4.6: Comparison of flow visualisation and CFD results.

They have been first analyzed for the situation of zero sweep. The flow situation in the water tunnel with dye flow visualization shows a white coloured thick streamline upstream of the serrations in direction parallel to the X-axis. Once the water passes the serration, a flow turning effect can be seen as the streamline is directed downwards, at a certain angle in negative Z-direction (inboards). Furthermore, the visualization shows that the flow remains laminar and steady. This justifies our decision to use a steady-state flow solver. The near-surface streamlines generated from the CFD results, Fig. 4.6b, look very similar to that of the experimental result. The different colours indicate different streamlines started at the same X, Z location but at varying wall-normal distances 'Y' to the flat plate. Near the wall (blue to green colours), the flow turning is maximum. As the distance from the plate increases, the observed flow turning effect reduces and disappears completely at the serration tip (red colour). This indicates an induced crossflow near the wall. We interpret this data such that the 3D curved shape of the serrations cause this change in flow direction, because on a plate without serrations or a plate with symmetric planar serrations such a change in flow direction is not expected to occur. In Fig. 4.6c the envelope of the flow turning effect is given by the two extreme streamlines, the one with zero and the one with maximum turning, respectively, for both the CFD and the flow visualization. Since the result from the flow visualisation and the CFD are in good agreement, further results from CFD simulations can be accepted with confidence. Fig.4.7 shows the near-surface streamlines (along the first cell away from the wall of the numerical mesh) on the flat plate surface for various inlet flow angles in the X-Z plane. In Fig.4.7b the inlet flow is aligned with X-axis (zero sweep) and once the fluid passes through the serration the flow is turned towards the inboard direction as already explained above. The same trend of flow turning is observed also for increasing backward sweep (angle $\beta = 10°$ Fig. 4.7 c and 20° Fig. 4.7d). Altogether, this data proves that the serrations work as a cascade of guide vanes or finlets, which turn the flow in the boundary layer in the opposite direction of the normally observed cross-span flow in a coherent manner along the span.

4.3.2 Detailed examination of the flow turning

Further information is gained from the flow turning angle just behind the serrations shown in Fig.4.8 for various inlet flow angles. As the chord and the stagger angle are largest at the root of the barbs (Fig. 4.3b), it is obvious that the flow turning is more pronounced near their root, while it reduces when moving towards the tip. We

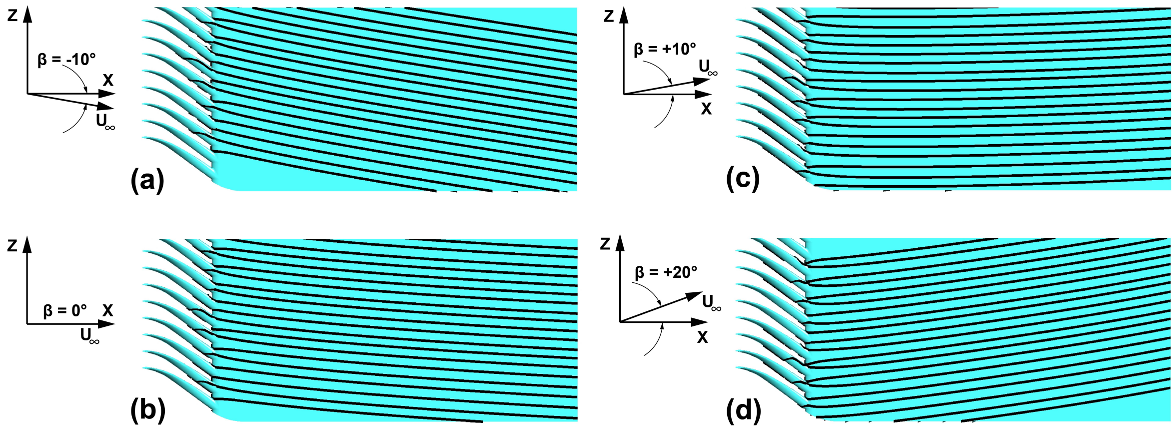

Figure 4.7: Surface streamlines from CFD simulations. (a) Negative sweep angle β = -10°. (b) Zero Sweep angle $\beta = 0°$. Positive sweep angle (c) β=+10°. (d) β=+20°

again take help from the similarity to stationary guide-vanes and approximated the flow turning angle as proportional to the difference between inlet flow angle (β) and the stagger angle (ξ). The correlation of the turning angle equal to $(\beta - \xi)/2$ is based on the classical exit flow angle formula used for cascade blades ξ (Dixon and Hall, 2014). For cases with an inlet flow angle of $\beta = 0$ and +10 degrees the correlation is reasonably good (Fig.4.8b and Fig.4.8c), even for larger $\beta = +20$ degrees the trend is captured quite well (Fig.4.8d). The observed correlation captures the overall trend based on considerations for classical 2D guide vanes, indicating that even though the serrations have a 3D curved shape, the main factors in defining the flow turning is mostly determined by the dimensional variation of the chord and the stagger angle.

Note, that the flow turning effect induced at the plane of the serrations is affecting the direction of the streamlines even far downstream the chord until at the downstream end of the simulation domain (Fig. 4.6c), see also the flow visualisation experiment. Therefore the serrations have a far-reaching effect on the boundary-layer flow down the chord. To show that, we compared simulations for the plain plate with those having attached the leading-edge comb under otherwise identical boundary conditions. Normalised chordwise and spanwise velocity profiles at the outlet section at X/L=6 for a sweep angle of 10 degrees are shown in Fig.4.9a and

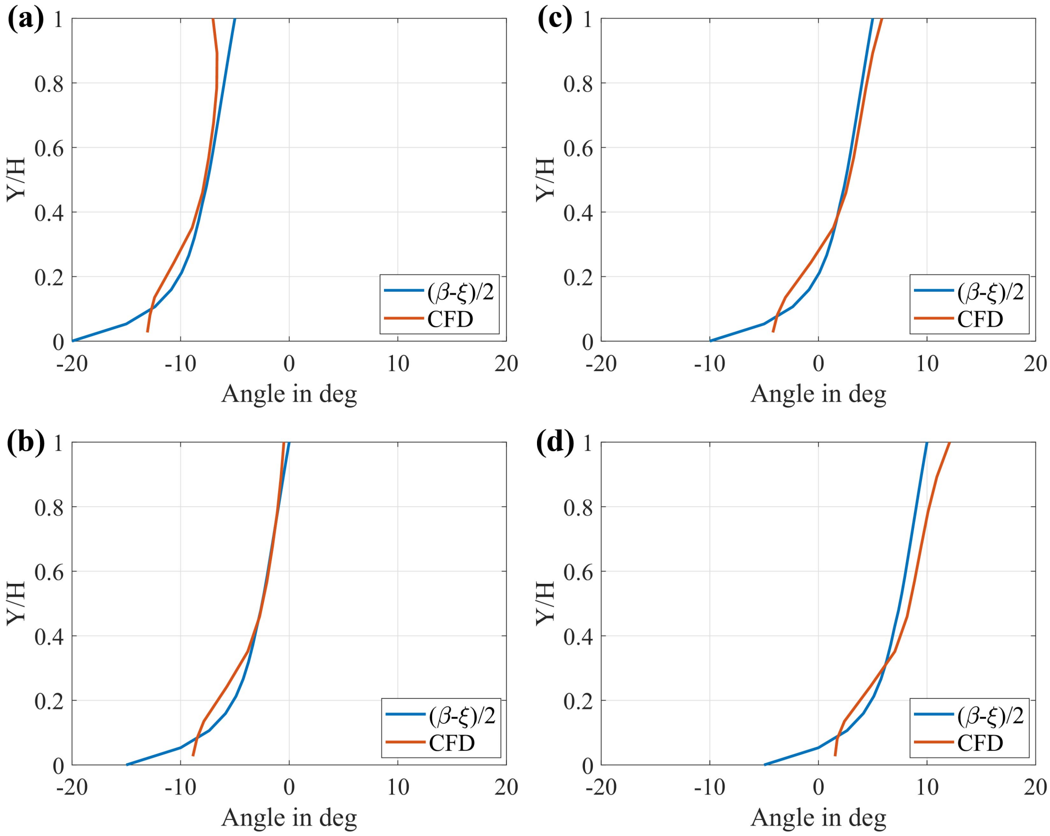

Figure 4.8: Wall-normal variation of turning angle behind serrations at X/L=0 for different sweep angles from CFD results and analytical formula. (a) β = -10°. (b) β = 0°. (c) β = 10°. (d) β = 20°.

Fig.4.9b. With serrations, the chordwise velocity profile shows a larger deficit than without serrations (Fig. 4.9a), which leads to an increase of the displacement (δ^*) and momentum thickness (θ) to twice the value without serrations (flat plate). However, the shape factor ($H = \delta^*/\theta$) remains around 2.4, suggesting that the serrations are not acting as a flow tripping device (this is when the shape factor exceeds 3.5). The spanwise velocity profile for the plain plate (without serrations) resembles the one in chordwise direction (Fig. 4.9b). However, adding the leading-edge comb leads to a dramatic decrease of the spanwise flow inside the boundary layer region with further reach into the free-stream. For a better illustration of the net-effect induced by adding the leading-edge comb, we plot the difference of the spanwise velocity profile (ΔW) defined as $W_{wi} - W_{wo}$ for all the cases considered here (wi - with ser-

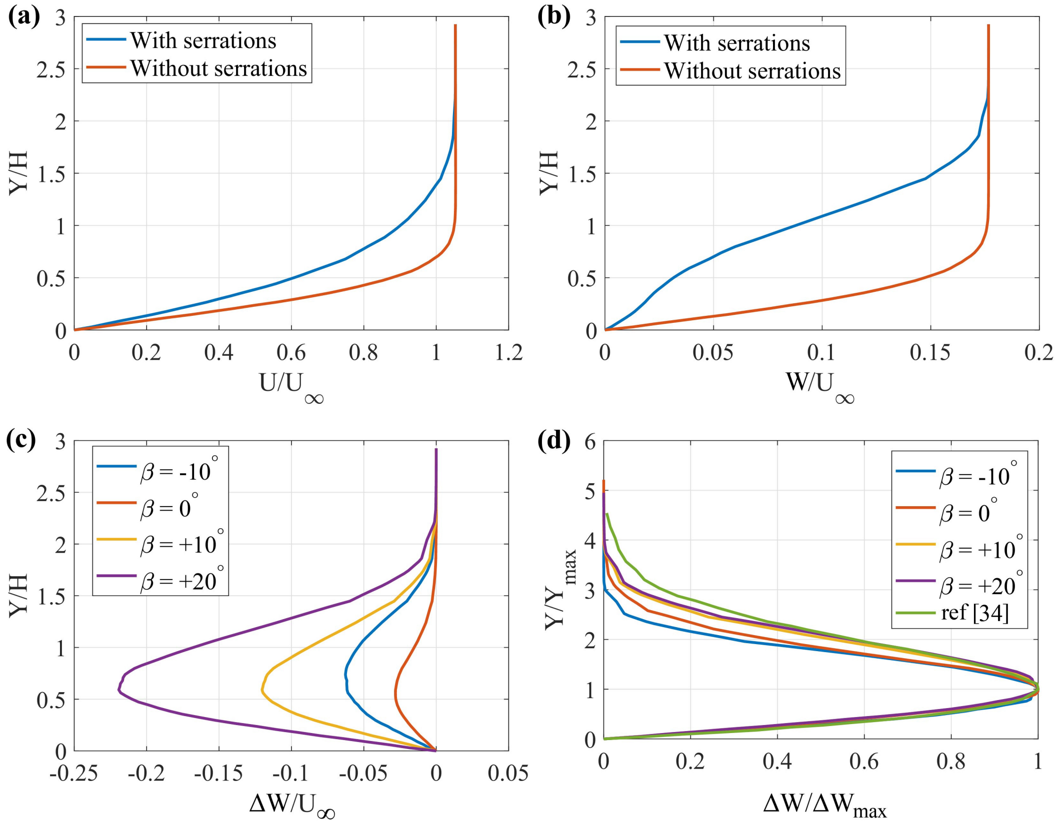

Figure 4.9: Velocity profiles from CFD simulations at X/L = 6 downstream of the leading edge. (a) Chordwise velocity for β = +10°. (b) Spanwise velocity for β = +10°. Net-effect of crossflow profile (c) For all sweep angles. (d) Normalised crossflow velocity profile with comparison to Ustinov and Ivanov (2018)

rations, wo - without serrations).This resultant velocity profile increases from zero to a maximum value within half the height of the barb and then it monotonically decays to minimal value at a height which is more than twice the height of the barb. Hence, this profile strongly resembles that of a wall jet, which counter-acts the sweep-induced spanwise flow in the plain plate (Fig. 4.9c). The peak values in ΔW are reached at about half the serration height for all flow angles. Furthermore, the magnitude of the peaks increase with increasing sweep angle. These results show also a significant flow turning effect for the negative sweep angle ($\beta = -10°$), which was not clearly recognizable from the illustration of the surface streamlines (Fig. 4.7a).

When all the ΔW profiles are normalised with respect to their corresponding maximum and the coordinates are scaled with respect to the position of maximum velocity, the profiles nearly collapse (Fig.4.9d). The data well resembles the spanwise velocity profile used in the theoretical work from Ustinov and Ivanov (2018) that was effective in counter-acting the cross-wise instabilities in swept wing flows.

4.4 Large Eddy Simulation Results

To study the laminar flow turning on a serrated airfoil, preliminary Large Eddy Simulations were performed to support the hypothesis that the flow turning will delay instabilities. To the best knowledge of the authors, only one LES study around swept wing at sweep angles and Reynolds number similar to the conditions which is expected in a owl wing flight, exists (Uranga et al.). Flow over swept wings at low Reynolds numbers (around 10^5) is complex due to the interaction between various instabilities. Tollmien-Schlitching waves, crossflow vortices and Kelvin Helmholtz instability from laminar separation bubbles (if present based on adverse pressure gradient) interact in a non-linear way, making them unable to be decoupled, as it is modeled in standard RANS models (Uranga et al.). Hence to investigate the laminar flow turning effect and possible flow control mechanism a preliminary Large Eddy Simulation study was performed with Ansys Fluent version 19.0 using WALE (Wall-Adapting Local Eddy-viscosity) subgrid scale model. The mesh details are given in Appendix-B and the domain lengths are similar to the size reported in previous literature (Uranga et al.). All simulations were done on SD7003 airfoil with a chord length (c) of 150mm and at a free stream velocity (U_∞) of 5.8 m/sec at a sweep angle (β) of 20 degrees and at zero angle of attack. The non-dimensional time step size was set at Δt = dt $\times$ U_∞/c = 0.008 for the simulations reported in this LES study.

Figure 4.10 shows the time averaged surface streamlines on plain airfoil and serrated airfoil. For the plain airfoil the surface streamlines are tilted at an angle which is

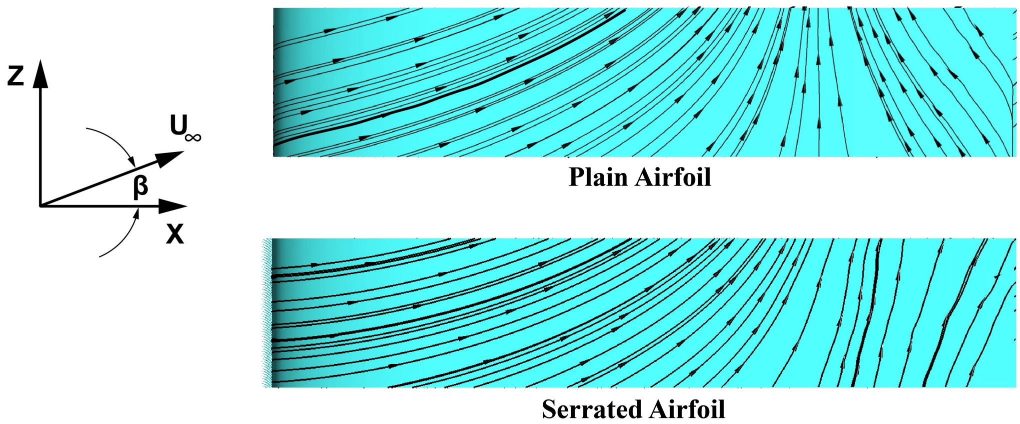

Figure 4.10: Time averaged surface streamline for Plain airfoil (top), Serrated airfoil (bottom).

equal to the inlet sweep angle. As the flow moves over the airfoil at an oblique direction, the flow becomes separated at around 73% of the chord length as seen from the streamline direction. Whereas, as explained in the previous section, (using flat plate simulations) the serrated airfoil shows the tilting of the streamlines towards inboard direction mostly parallel to the chord line until about 10% initial chord length. This flow turning near the leading edge largely changes the flow downstream to completely suppress the separation as it is clear from the streamline direction towards the aft part of the airfoil.

Figure 4.11 depicts the instantaneous vortices identified by the 'Q' criterion on the plain airfoil and serrated airfoil. For the plain airfoil case the 'Q' rollers are located at regular intervals which represents TS waves. However, the TS waves are deformed in the spanwise direction and this is due to the crossflow effects. On the serrated airfoil, because of the initial flow deflection, which is largely parallel to the chord line, the TS waves are mostly two dimensional indicating that the crossflow effects are pushed downstream. This is reflected in the surface flow which was explained above. It should be noted here that the laminar flow turning is proved for an airfoil with delay of crossflow effects. This result is comparable to the stabilization of swept wing boundary layer by distributed cylindrical roughness elements on the leading edge of an airfoil (Hosseini et al., 2013). The data strongly suggests here that the leading edge serrations will definitely have multiple roles on different flow regimes based on the operating conditions which is beyond the scope of the current investigation.

While these initial LES study already indicate a positive effect on the instabilities, some limitations need to be discussed here. Firstly, the largest wavelength to be captured is limited by the periodic domain in the simulations (Uranga et al.). However typically the crossflow instabilities have a wavelength or order of several boundary-layer thickness which is well captured herein. Secondly, due to the large disparity in scales between the serrations (length of 2.5mm) and the full wing (chord length 150mm is similar to owl wing) the time step to achieve a Courant number less than 1 needs to be very small, enforced by the small micron-size mesh spacing in the serration regions. However, as the flow near the leading edge is laminar and almost steady, a somewhat larger time-step is allowed herein to recover the temporal evolution of the flow instabilities further downstream where grid spacing is increasing. A similar issue happens to limit experiments with original scale models of the serrated wing as it requires precise micron-size printing of the complex shape of the serrations on a large wing. Such limitations may be overcome in the future by high-resolution nano-printing devices and is therefore left for future work.

4.5 Discussion and Conclusions

We showed that serrations at the leading edge of an owl inspired model induce an inboard directed flow that is in opposite direction to the cross-span flow induced by the backward sweep of the wing. In the following we shall first discuss these data with respect to the existing literature, arguing about some methodological considerations and then speculating about its consequences for owl flight and flight in general.

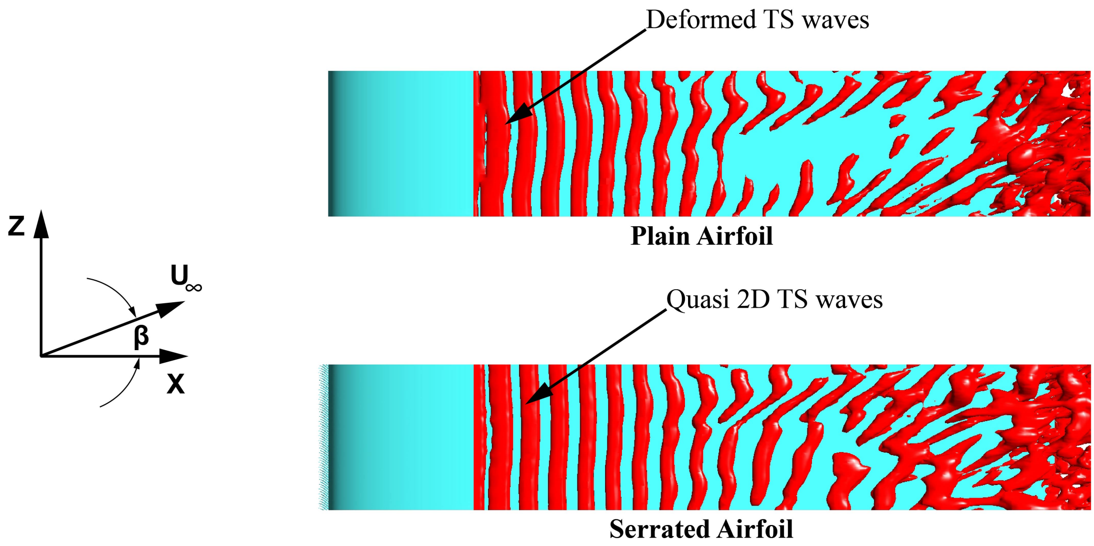

Figure 4.11: Instantaneous vortices identified with 'Q' criterion. Plain airfoil (top), Serrated airfoil (bottom).

4.5.1 Comparison with other work

To the best of our knowledge, no study has directly addressed how the sweep angle influences the flow in nature-inspired serrated wings. The work most important to our new data and hypothesis is that by Ustinov and Ivanov (2018). The near overlap of the curves in Fig. 4.9d shows that the serrations reproduce the effect envisioned by Ustinov and Ivanov (2018). These authors discussed this effect as to counter-acting the cross-wise flow in swept wing and thereby attenuating the crossflow instabilities, a negative feature of backward swept wing aerodynamics. The work of these authors is based on a theoretical consideration of micro-perforation or winglets on the surface of a wing, which are arranged in a way that they produce a spanwise flow in the boundary layer opposite in direction to the cross-span flow induced by the sweep-effect. With this configration, Ustinov and Ivanov (2018) observed a wall-jet like flow profile in spanwise direction that is similar in shape and relative magnitude to our net-effect result. Therefore, the 3D curved serrations of the barn owl wing could be thought of as a leading-edge laminar flow control device which counteract the crossflow instabilities in swept wing aerodynamics.

As we could show here, the serrations of the owl wing are not comparable to classical vortex generators, which was speculated so far in previous work (Geyer et al., 2020; Hertel, 1963). These vortex generators are used traditionally to control the flow separation on the suction side of the airfoils (Lin et al., 1994). They produce strong streamwise vortices to mix the fluid flow via the lift-up effect which results from the ejection of fluid elements in low velocity region and injection into high velocity regions, thus increasing streamwise momentum near the wall. In comparison, our study found that the serrations studied herein, behave similar to 3D curved cascade blades which turn the flow to a certain degree depending on the spacing to chord ratio and the blade angle (stagger angle). Hence, near the root of the serrations the spacing to chord ratio is low and the stagger angle is high to guide the flow to turn at relatively high angles when compared with the tip. Kroeger et al. (1972) hinted on the cascading effect of the leading edge serrations. However, they stated that the serrations push the flow behind the leading edge towards the outboard region of the owl wing, which is opposite to our observation. Note, that their statement resulted from tuft flow visualisation where the length of the tufts was greater than 4 mm. Therefore, the tuft motion will be the result of an integration all over the complete boundary layer thickness and part of the external flow. Since the height of the serrations is less than 2 mm, they probably could not see our results because of this integration effect. In addition, any method of flow visualization or flow measurement must ensure to get data very close to the wall as provided herein. This is where we benefit from the testing of an enlarged model in a water tunnel, fulfilling the rules of fluid mechanical similitude.

A vague indication of flow turning may be found in the results from Wei et al. (2020), although not mentioned therein. It seems from their Fig. 10b in Wei et al. (2020)) that the hook-like serrations changed the direction of flow. However, since the graph is cut downstream at about 0.5 of serration length, it is difficult to infer a concluding answer on any flow turning.

4.5.2 Methodological considerations

It is obvious from live recordings of the gliding flight of owls that the leading edge in the region of serrations, is swept backward (Kroeger et al., 1972; Durston et al., 2019), an aspect which has so far not found attention in the discussion of the function of the serrations. We observed a flow turning effect induced by the 3D curved serrations, which counter-acts the crossflow induced in backward-swept wing. In this respect it seems important that we have carefully rebuilt the natural shape of the serrations, characterized by twisting and tilting and taper, which Bachmann and Wagner (Bachmann and Wagner, 2011) called a first order approach and not used the zero order approach, i.e. use simply-shaped, often symmetric serrations as is done in most studies (Geyer et al., 2020; Rao et al., 2017; Ikeda et al., 2018; Geyer et al., 2017). The focus of the study was to demonstrate the basics of the novel turning effect. A good correlation was found between the observed turning angle and the classical formula for cascade blades, approximated as the summation as inlet flow angle β and the stagger angle ξ (Dixon and Hall, 2014).

Not all parameters could be assessed in this first study. Further work might unravel the role of the wavelength, as it is obvious that a too large inter-spacing will destroy the homogeneity of the induced crossflow and a too small inter-spacing will cause unnecessary form drag. More studies are also necessary to find out how the angle of attack and the Reynolds number influences the flow turning, and how far the laminar hypothesis is valid.

4.5.3 Consequences for owl flight

The inboard portion of the owl wing has thick and highly cambered airfoil where laminar separation bubbles form. These bubbles are reduced by the velvet-like surfaces on the suction side of the owl wing (Wagner et al., 2017). However, towards the outboard portion of the wing there is a big variation in the sweep angle of the wing. Therefore the comb like elements should have an impact on the swept wing boundary layer. The consequence of a manipulation on the flow reported in Ustinov and Ivanov (2018) for a swept wing is that it delays transition to turbulence. Because of the striking similarity of the effect of the manipulation on the boundary layer profile to the effect we observed, we conclude that the leading-edge comb acts to delay transition on the swept wing of the owl. A delay of transition would correspond to a reduction in noise production as the portion on the wing surface where the flow is turbulent is reduced or even completely removed. Owl flight is so silent that it is difficult to measure directly (in absolute terms) the noise these birds produce. Only in comparison with other, non-serrated wings, does the noise-reduction of owl flight become clear (Neuhaus et al., 1973; Geyer et al., 2020). Thus, the influence on the air flow as demonstrated here may be critical in nature, where a hunting owl has to remain silent until right before the strike. Serrations which can help to keep the flow laminar and preventing crossflow instabilities for typical flight conditions with backward swept wing, therefore, may provide a major advantage for the hunt.

4.5.4 Conclusions

To conclude, we have investigated the effect of a nature-inspired leading edge comb on the flow along a swept flat plate and an SD7003 airfoil. Special focus is laid on the leading-edge comb influence on the backward swept wing in gliding flight, which is known in classical wing aerodynamics to introduce considerable cross-span flow, which suffers instabilities and triggers early transition (Serpieri and Kotsonis, 2016; Radeztsky et al., 1999; White and Saric). As evidenced in the CFD and the experiments, our model produces a flow turning which is counter-acting the cross-span flow. The magnitude of this effect is proportional to the stagger angle of the local cross-section of the barbs. If the sweep angle is increased, the flow turning becomes more pronounced, suggesting that the owl's leading-edge comb is tailored for attenuating the crossflow instabilities. Ultimately, this means a laminar flow control with benefit of a quiet flight.

Appendix

A. Mesh Convergence

Three different mesh were generated with unstructured grid around the serrations along with inflation layers to resolve the boundary layer. The region surrounding the serrations were discretised into several blocks to generate the structured grid. The coarse, medium and fine mesh had 2.1, 4.9 and 16 million elements respectively. The coarse mesh is shown in Figure 4.12a, b and c, as an example. The streamwise and crosswise velocity profile for zero sweep angle behind the serration (five serration length downstream) is compared and shown for all the grids in Fig.4.13. The profiles for all the grids overlap, which indicates that the results reported in this study are mesh independent.

B. Mesh Around Airfoil With and Without Serrations

Figure.4.14 shows the mesh around plain airfoil and serrated airfoil in X-Y plane used in LES simulations. The chord length (c) of the airfoil is 150mm. For both cases the domain extends '6c' upstream and '9c' downstream direction and '6c' in the 'y' direction each side. The spanwise direction of the domain is fixed at '0.2c' which is selected from previous literature. For the plain airfoil the surface is discretised with 125 points in streamwise direction on either side and 100 points in spanwise direction, the structured mesh shown in Fig. 4.14a. The first cell distance from the airfoil surface was 0.05 mm which resulted in a y+ value less than 1 with a

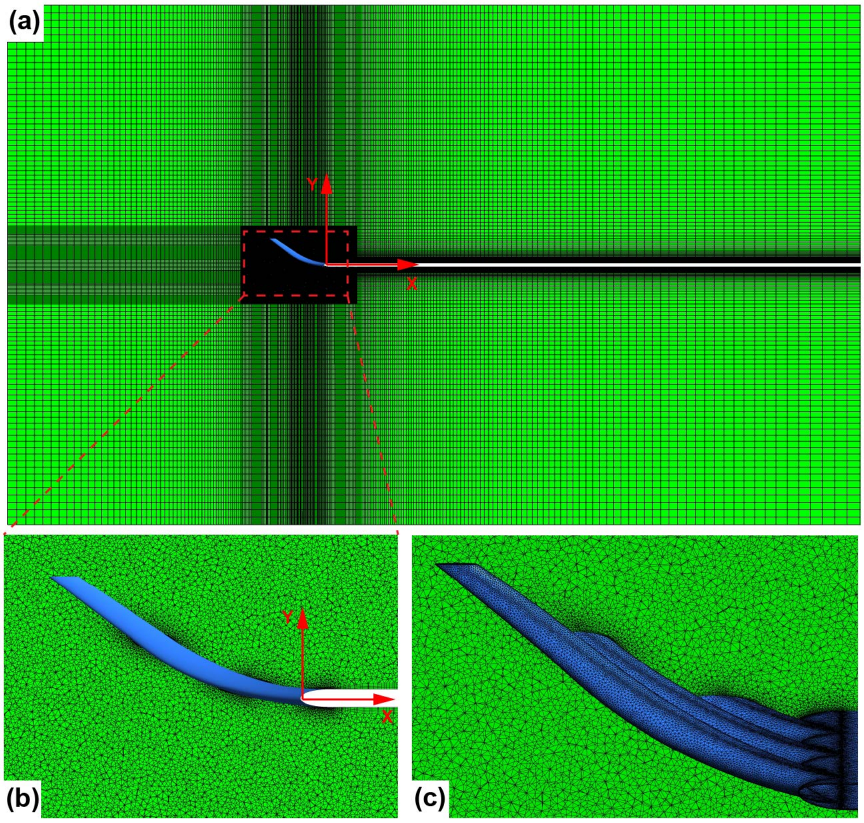

Figure 4.12: Computational domain with serrations. (a) Unstructured mesh near serrations (shown inside red rectangle) and structured mesh in all other regions. (b) and (c) Enlarged view around the serrations.

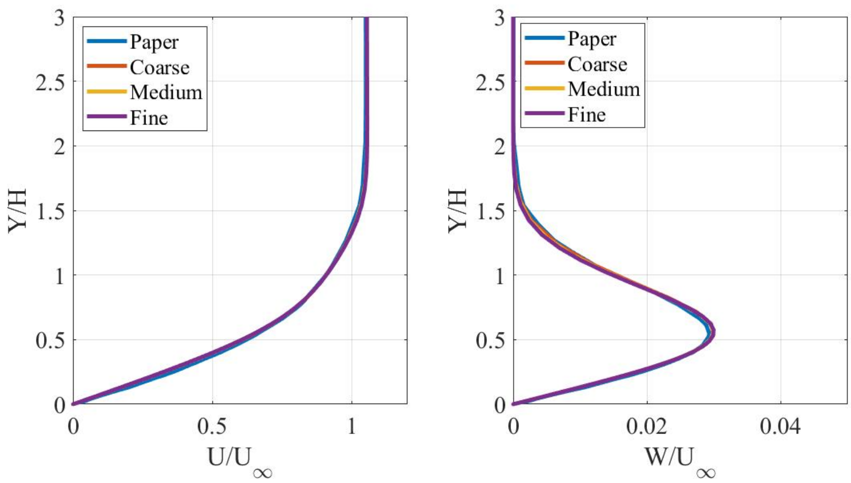

Figure 4.13: Mesh dependency result for all grids. Normalised velocity profiles behind five times the serration length. Streamwise velocity (U/U_∞) (Left) and Crosswise velocity (W/U_∞) (Right).

total mesh size of 5.5 million. For the serrated case, unstructured mesh was used surrounding the leading edge region of the aerofoil which increased the total mesh size to 14.4 million elements. The mesh for serrated airfoil is shown in Fig.4.14b. The close view of serrations is shown in Fig.4.14c and d. For the spanwise length of '0.2c' sixty serrations were accommodated. Periodic conditions were used in the 'Z' axis faces to simulate infinite serrations.

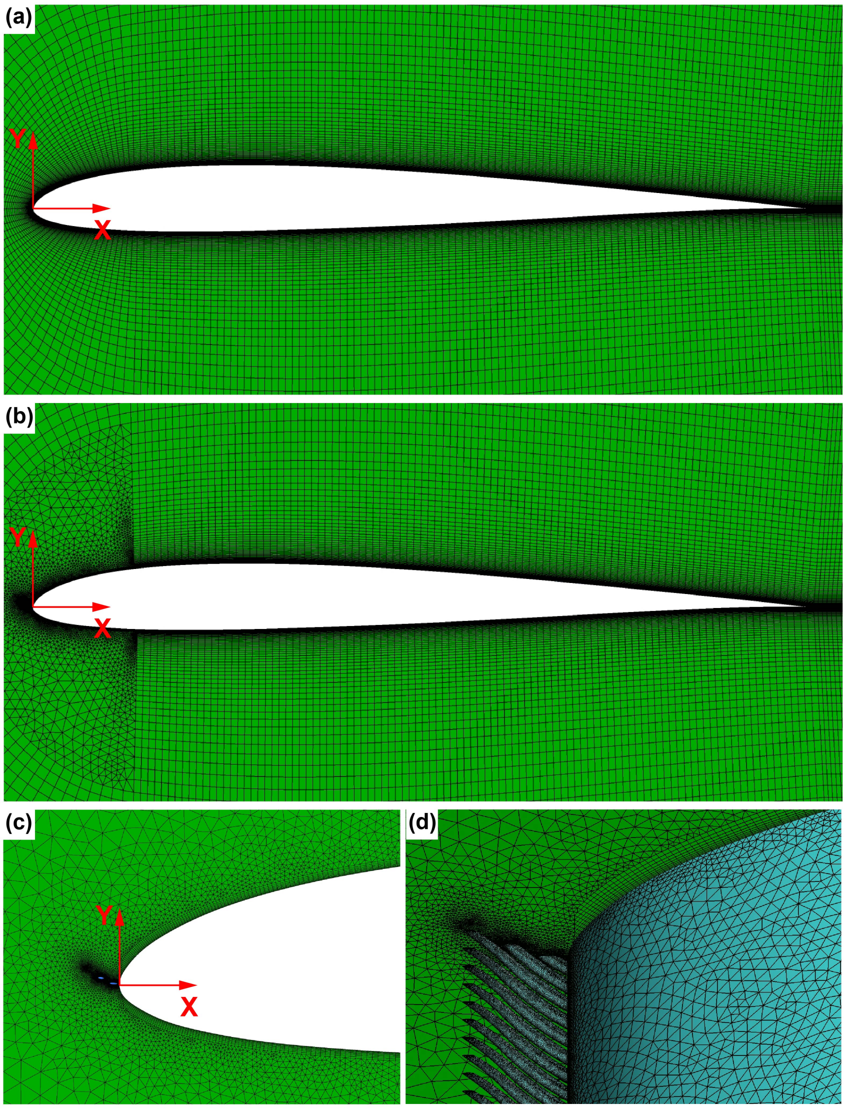

Figure 4.14: Mesh for plain airfoil with and without serrations. (a) Structured mesh around plain airfoil. (b) Mesh for airfoil with serrations (c) and (d) Enlarged view around the airfoil with serrations.

Point of clarification: Two methods have been used to control crossflow instabilities, namely discrete roughness elements (DRE) and upstream flow deformation (UFD). Does the present work compares with any of these two methods or does it relate to a new flow control technique?

Discrete roughness elements (usually cylindrical roughness elements) placed near the leading edge of the swept wing at shorter spanwise wavelengths when compared to critical wavelength is known to attenuate the primary crossflow instability(Saric et al., 1998). This method is a passive flow control technique which is very sensitive to the roughness shape and dimensions. Upstream flow deformation (UFD) technique is done by placing plasma actuators forcing along or against the natural crossflow direction to promote or delay crossflow transition(Serpieri et al., 2017). This is an active flow control technique. Recently this technique was experimentally investigated using AC-DBD plasma actuator to delay transition(Yadala et al., 2018). Therefore, the leading-edge serrations can be compared to passive flow control UFD technique since it turns the flow opposite to the natural crossflow in a coherent manner. Also, from the nature point of view, if the serrations are only roughness elements, which control the wavelengths of the primary instability, then the complex three dimensional shape is not needed and straight serrations are sufficient to delay the instabilities.

4.6 Critical Analysis

The CFD results and the flow visualisations revealed that the leading-edge serrations from owl wings produce a coherent flow turning (spanwise inboard flow) which could play an important role on flow over swept wings. In this section, responses to the queries which arose during the review and from other researchers have been recorded.

Claim-1 *A swept flat plate at zero angle of attack, without a displacement body above it or an otherwise enforced streamwise pressure gradient, develops no (true) crossflow perpendicular to the boundary-layer edge streamline direction. The streamlines are largely straight (but oblique in a plate-fixed coordinate system). As it is understood, negative pressure gradient was not enforced (without comb, uncontrolled wing-like flow). Hence the comb-induced crossflow - the local turning - naturally relaxes downstream causing (anti-)curved streamlines - and does not need to counteract a natural crossflow here like on a lifting wing.*

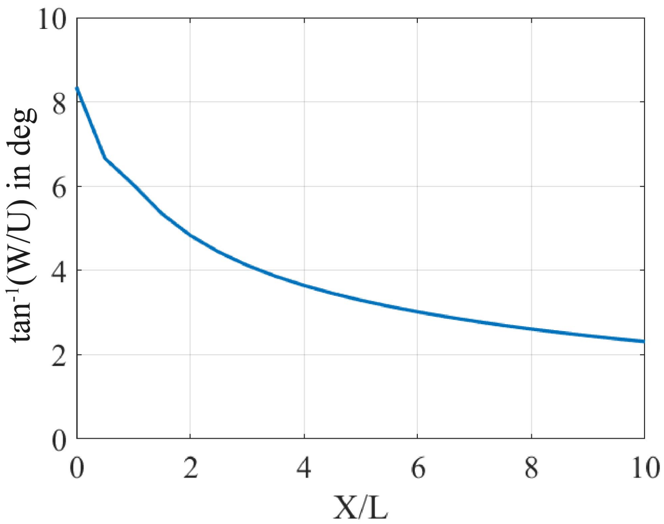

Figure 4.15: Maximum flow turning angle specified in degrees over downstream distance normalised by the serration length (L).

The claim is reasonable and indeed, the flow along a swept flat plate without a pressure gradient will not generate any crossflow vortices. However, the flow turning effect was also demonstrated on a cambered aerofoil using a precursor LES simulation (which has a pressure gradient), refer chapter-4. Therefore, it is suggested that the basic nature of this effect is not affected to a great extent by the pressure gradient. To investigate the relaxation of this flow turning due to viscous diffusion, the studies on the flow along the flat plate are more suitable and easier to conduct. The direction of the streamlines are determined by the angle between the crossflow velocity and the streamwise velocity and its maximum value is displayed along the streamwise coordinate in Fig.4.15. Immediately downstream of the serrations, the maximum flow turning angle is about 8°. As the flow travels further downstream, the value decreases monotonically and reaches a turning angle of 2° at a distance of 10-times the length of the serration. Furthermore, a small remaining flow deflection near the wall can be observed even after around 40 serration lengths (not shown here), so the flow-turning effect is not considered to be a local effect.

Claim-2 *How does the aerodynamic characteristics of the aerofoil changes with and without serrations? Why was this not included in the LES results?*

The scope of the published work was mainly on understanding the spanwise flow behind the serrations and to link this flow-turning effect to the situation of swept wings and the possible control of crossflow instabilities. Therefore, the LES investigations were done to prove the same flow-turning effect on a SD7003 airfoil with a chord length (c) of 150mm at a free stream velocity (U_∞) of 5.8 m/sec at a sweep angle (β) of 20 degrees and zero angles of attack, similar to the flat plate case (zero pressure gradient). After publication of these results, the LES data was analyzed to provide the aerodynamic forces acting on the aerofoil and the results are included herein. Fig.4.16 shows the aerodynamic forces for both the plain and serrated aerofoil at zero angles of attack. The results are presented for the total period of six non-dimensional time cycles where $T = c/U_\infty$ and t is the flow time in seconds. When examining the lift coefficient for the plain and serrated aerofoil case in Fig.4.16a, it is clear that the serrated aerofoil produces about 29.35% more mean lift compared to the plain aerofoil. In addition, , there is only a slight increase (about 1.5%) in mean drag as shown in Fig.4.16b. This result was intentionally not included in the published article because it is only a single operating point for which the flow around the aerofoil was simulated. To judge the overall performance of the serration, further information is necessary for the full range of angles of attack in all flow regimes, such as linear, non-linear and post-stall regions.

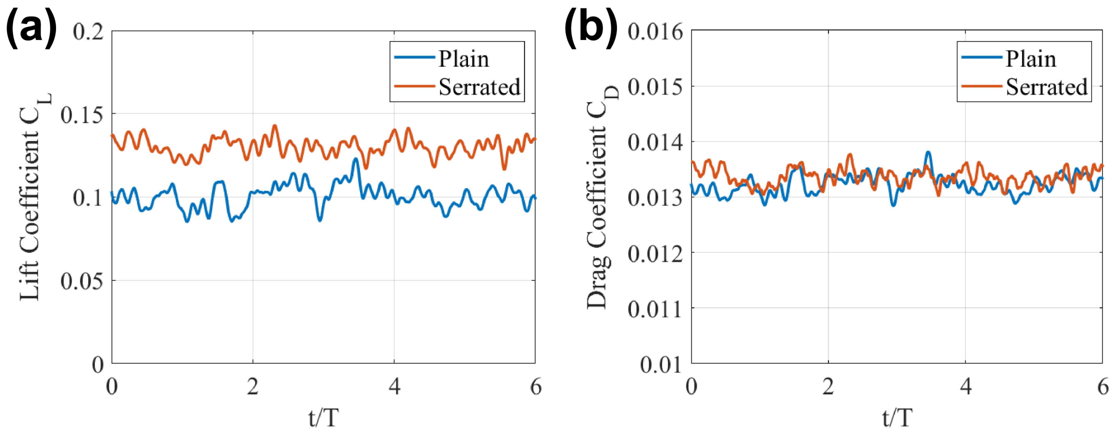

Figure 4.16: Aerodynamic characteristics of plain and serrated aerofoil. (a) Lift Coefficient. (b) Drag Coefficient.

Claim-3 *The inboard bending of streamlines is shown, but how is that flow-turning affects the possible attenuation of noise in owl flight at higher angles of attack?*

The owl wing during gliding flight is typically operating in the low Reynolds number range (Re 10^5). For aerofoils operating in this regime the emergence of a laminar separation bubble is often observed. At small angles of attack, the separation is seen near the trailing edge of the aerofoil. As the angle of attack increases, the separation point propagates further upstream so that the separation region grows. Shear-layer instabilities eventually trigger transition which causes the flow to reattach as a turbulent boundary layer, closing the region of reversed flow (closed bubble). The formation of rollers at the outer edge of the shear-layer eventually promotes quasi-periodic vortex shedding which results in unsteady forces and tonal noise emission when travelling over the trailing edge. Based on previous investigations and operating conditions, such a laminar separation bubble is assumed to exist on the owl wing. With the given results of the serrated wing causing the separation bubble to cease, it is expected that the leading-edge serrations could reduce the tonal noise from the laminar separation bubble at moderate angles of attack. Further ongoing studies are also looking at the effect of the serrations on the roll-up of the tip-vortex and its possible contribution to noise at larger angles of attack.

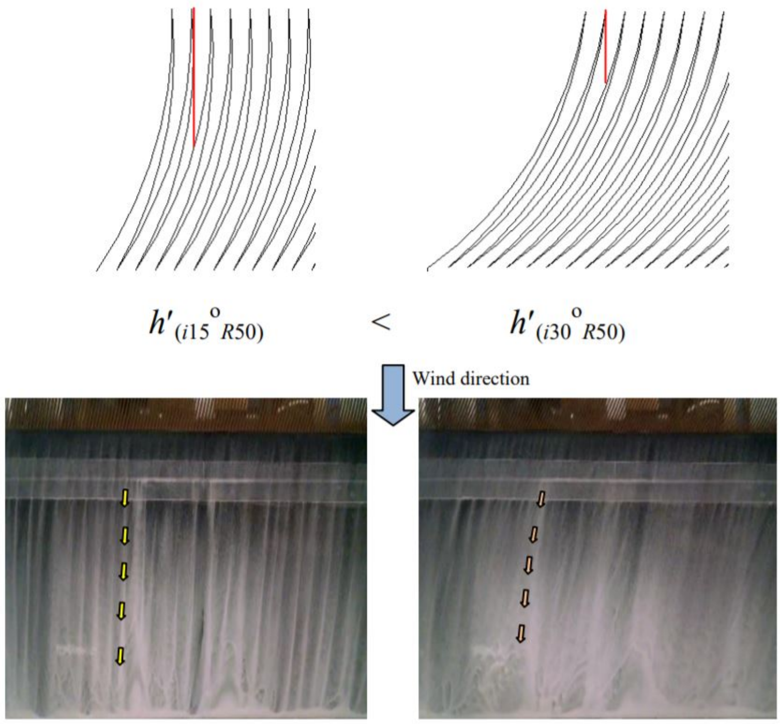

Figure 4.17: Flow deflection picture behind 2D curved serrations. Reproduced from (Juknevicius et al., 2017).

Claim-4 *Possible overlap with the research work on curved serrations from Auris Juknevicius et al. (Juknevicius et al., 2017)*

The above cited conference paper on curved serrations was not intentionally omitted in the reference list of the published papers, by chance, it was found only during the critical analysis of the thesis that we came across one figure, which is related to

Parameter	(Juknevicius et al., 2017)	Thesis
Curvature	2D	3D
Serration length	5 to 30mm	2.5mm
Serration wavelength	2.5 to 20mm	0.5mm
Identification like cascade	No	Yes
Swept wing	No	Yes
Reynolds number	200,000 to 600,000	60,000
Inlet flow	Turbulent	Laminar
Flow mechanism	Turbulence leading-edge noise interaction	Crossflow instability

Table 4.2: Comparison of investigated details in this thesis and Juknevicius et al. (2017)

the current work. This figure is not included in the peer-reviewed work of the same authors, which was read and analyzed for possible relevance of the studies in our original publication (Juknevicius and Chong, 2018). The authors studied several straight and 2D curved serrations which were laser-cut from thin sheets and were very different from the actual curved serrations. In addition, there was no mention of the swept wing effect and the crossflow related instability. The serrated aerofoils were tested in an acoustic wind tunnel with high incoming turbulence and focused on the leading edge interaction noise rather than on the laminar flow turning effect presented herein. Therefore, for all these reasons, it was considered that the effect of curved serrations on laminar flow manipulation was not studied. Therefore it was not cited in our original publication. The following table.4.2 will provide a brief summary of the differences between the technical points under discussion.

As mentioned above, during the critical analysis of this thesis, I noticed that the Fig.4.17 (reproduced here from the conference paper) (Juknevicius et al., 2017) suggesting a flow-turning effect. This figure is not included in the peer-reviewed journal paper and therefore seemingly has not found much attention to the authors. The mechanism of flow turning is not explained and apart from this picture, all other ideas and results discussed in this thesis are entirely different.

Future work

The results presented in this thesis provide strong indications that the serrations play an important role in laminar flow control over owl wing, with possible links to improved aerodynamic performance and noise attenuation. Further studies should continue with aerofoils with a more realistic representation of the owl wing profiles, such as the AS6092 aerofoil with a thickness to chord ratio of approximately 5%. Flow over this aerofoil should be analyzed at different sweep angles and at different angles of attack. Crossflow vortices and their interaction with TS waves or laminar separation bubbles should be explored in detail. Subsequently, the roll-up and strength of the tip vortex should be studied for the different wing parameters and serration conditions. Finally, the serrated aerofoil should be studied under the same experimental conditions in an anechoic wind tunnel. In this way, it is also possible to explore the different aspects of the serrations on the overall acoustic benefit.

An alternative approach may also be applied to study the serrated swept wing. In this method, a flat plate along with an adjacent contoured plate could be used to simulate the pressure distribution on the AS6092 aerofoil. Both the flat and contoured plates must be swept at an angle to exhibit the swept wing configuration. The leading edge region of the flat plate can be designed in such a way that both the elliptical leading edge and the serrations can be interchanged to test both flow configurations. All measurements, such as flow visualization, PIV or hot wire, should be relatively easy on a flat plate as compared to a real aerofoil. However no acoustic results can be generated with this approach.

Uncertainty analysis

Fish scale measurements

As explained in chapter-1, the fish scale array were measured using a digital microscope, however, the measurements were not done on regular shapes where uncertainty could have been quantified. All measurements were done by visual inspection on each scale array image and manually the radius and the length of the scale were noted.

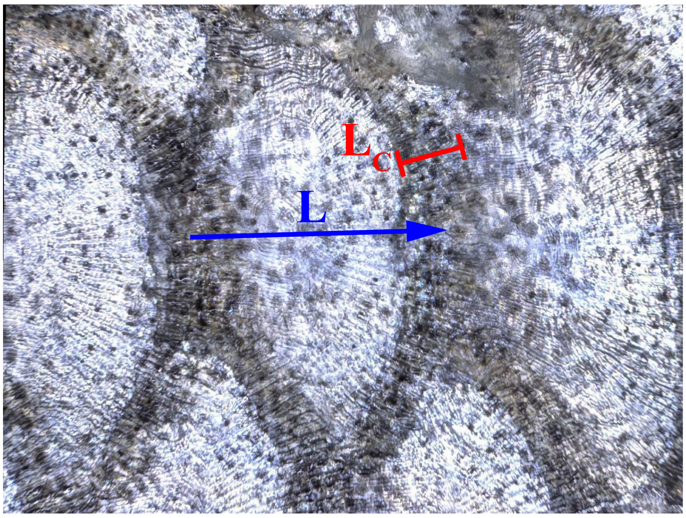

Figure 4.18: Image of fish scales with length (L) and length of the ctenii (L_C) marked.

Figure.4.18 shows the length (L) marked manually. The red marking shows the length of the ctenii which is present on the scale end. It differentiates the inner and outer part of the scales clearly by changing texture. Therefore, the ctenii region was used to mark the length and radius of the scales in all images. So, the length and radius of the scales always fall within $L_{avg} \mp L_C/2$ and $R_{avg} \mp L_C/2$, where L_{avg} and R_{avg} is the average length and average radius of one particular scale and not to be confused with the averages from all scale images.

Hot-film measurements

Measurement of velocity fluctuations using hot-film anemometry are always subjected to uncertainties. Few of them are listed below.

- Calibration errors
- Calibration drift errors
- High frequency errors
- Spatial resolution errors
- Disturbance errors
- Natural convection errors in close proximity of the boundary

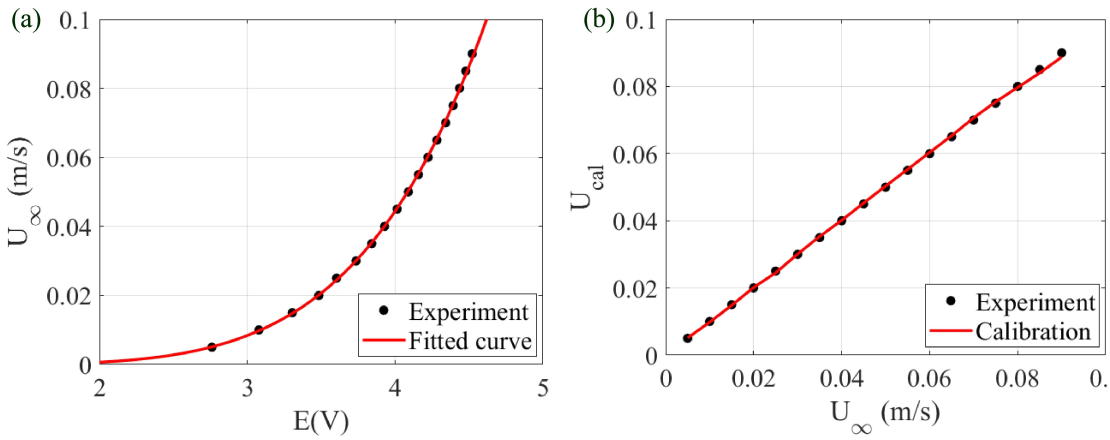

Figure 4.19: Hot-film calibration curves. (a) Voltage vs velocity. (b) Experimental velocity vs calibrated velocity from the hot-film probe.

Due to the limited hot-film measurements, the uncertainty due to the calibration will only be quantified. The hot-film was calibrated in the water tunnel by traversing the probe with prescribed velocities using the automatic traverse. The voltage values from the hot-film at different velocities are shown in Fig.4.19a, the experimental points are then fitted with a curve using $U = \left[\frac{E^2 - A}{B}\right]^{\frac{1}{C}}$. Therefore, the uncertainty from a hot film arises from the calibration constants. The standard deviation of the measured velocity from N = 18 samples is calculated using the Eqn4.1.

$$\sigma_U = \sqrt{\frac{1}{N-1}\sum_{n=1}^{N}(U_{cal} - U_{\infty})^2} = 0.000506m/s \tag{4.1}$$

Progress Report

I started my doctoral research in January-2018 and my research position is supported by the German Research Foundation in the grant DFG BR 1494/32-1, with the project titled "Combined volumetric PIV-LIF-measurements of the correlation between bubble cluster dynamics and mixing in a co-moving frame of a stable/unstable bubble plume". The following content will discuss about the progress that have been made until now.

In the first year of my PhD (2018), the experimental set-up for the swirl bubble interaction flow studies was not able to be transferred from Technical University Bergakademie Freiberg, Germany. Therefore, my labmate Dr Qianhui had already started designing an experimental set-up at the City, University of London. Hence, along with this research study, I was also working on nature-inspired fluid mechanics in which I concentrated on the interaction of vortex street on sea lion whiskers. In that research work, I learned to use Particle Image Velocimetry (PIV) and image processing techniques which completely falls in-line with the DFG project as a learning phase. In the later part of the year, I started working on investigating the role of fish scale arrays on flow dynamics.

During 2019, I worked on the modelling of fish scale array and visited University of Stuttgart, Germany to use the water channel to study the effect of biomimetic fish scales on transitional flows and also ideas were discussed on using the fish scales near the bubbly flow to increase the residence time of the bubble cloud, hence reducing the drag. At the same time, Dr Qianhui was completing the flow rig and the necessary 3D scanning PIV set-up which is necessary for the DFG project. During November-2019, experiments on the flow-rig were completed initially with plane PIV results. An abstract titled "An experimental study on bubble dynamics in a jet plume with and without axial swirl" was accepted by the 20th International Symposium on the Application of Laser and Imaging Techniques to Fluid Mechanics, Lisbon, Portugal (2020). However, by March-2020 lockdown was imposed because of COVID-19 and the university was closed till June 2020. From July-2020, only restricted access was granted which largely constrained the experimental plans. To sum up, with the DFG funding, I have made significant progress in learning PIV techniques and carried out the preliminary experiments on the bubbly flow, however, I have also worked on various projects to write this thesis focusing on Nature-inspired fluid mechanics.

Bibliography

Abegg, C., Bippes, H., Boiko, A., Krishnan, V., Lerche, T., Pöthke, A., Wu, Y., and Dallmann, U. (2001). Transitional flow physics and flow control for swept wings: Experiments on boundary-layer receptivity, instability excitation and HLF-technology. In *Aerodynamic Drag Reduction Technologies*. Springer.

Afroz, F., Lang, A., Habegger, M. L., Motta, P., and Hueter, R. (2016). Experimental study of laminar and turbulent boundary layer separation control of shark skin. *Bioinspiration & Biomimetics*, **12**(1):016009.

Anderson, E., McGillis, W., and Grosenbaugh, M. (2001). The boundary layer of swimming fish. *Journal of Experimental Biology*, **204**(1):81–102.

Anderson, J. D. (2005). Ludwig Prandtl's boundary layer. *Physics Today*, **58**(12):42–48.

Anderson, J. D. (2011). *Fundamentals of Aerodynamics*. McGraw-Hill, New York, United States.

Bachmann, T. and Wagner, H. (2011). The three-dimensional shape of serrations at barn owl wings: towards a typical natural serration as a role model for biomimetic applications. *Journal of Anatomy*, **219**(2):192–202.

Bachmann, T., Wagner, H., and Tropea, C. (2012). Inner vane fringes of barn owl feathers reconsidered: morphometric data and functional aspects. *Journal of Anatomy*, **221**(1):1–8.

Bechert, D. W., Bruse, M., and Hage, W. (2000). Experiments with three-dimensional riblets as an idealized model of shark skin. *Experiments in Fluids*, **28**(5):403–412.

Beck, N., Landa, T., Seitz, A., Boermans, L., long Liu, Y., and Radespiel, R. (2018). Drag reduction by laminar flow control. *Energies*, **11**:252.

Berkooz, G., Holmes, P., and Lumley, J. L. (1993). The proper orthogonal decomposition in the analysis of turbulent flows. *Annual Review of Fluid Mechanics*, **25**(1):539–575.

Berra, T. M. (2007). *Freshwater Fish Distribution*. The University of Chicago Press, London, United Kingdom.

Betchov, R. and Criminale, W. O. (1967). *Stability of Parallel Flows*. Academic Press, London, United Kingdom.

Bhushan, B. and Jung, Y. C. (2006). Micro- and nanoscale characterization of hydrophobic and hydrophilic leaf surfaces. *Nanotechnology*, **17**(11):2758–2772.

Bhushan, B., Jung, Y. C., and Koch, K. (2009). Self-cleaning efficiency of artificial superhydrophobic surfaces. *Langmuir*, **25**(5):3240–3248.

Carbonara, P., Scolamacchia, M., Spedicato, M., Lembo, G., Zupa, W., and McKinley, R. (2006). Swimming performances as a well being indicator of reared sea-bass *Dicentrarchus labrax* (Linnaeus, 1758). Preliminary results. *Biologia Marina Mediterranea*, **13**(1):488–491.

Chaitanya, P., Joseph, P., Narayanan, S., Vanderwel, C., Turner, J., Kim, J. W., and Ganapathisubramani, B. (2017). Performance and mechanism of sinusoidal leading edge serrations for the reduction of turbulence-aerofoil interaction noise. *Journal of Fluid Mechanics*, **818**:435–464.

Choi, H., Park, H., Sagong, W., and Lee, S. (2012). Biomimetic flow control based on morphological features of living creatures. *Physics of Fluids*, **24**(12):121302.

Daniello, R. J., Waterhouse, N. E., and Rothstein, J. P. (2009). Drag reduction in turbulent flows over superhydrophobic surfaces. *Physics of Fluids*, **21**(8):085103.

Dean, B. and Bhushan, B. (2010). Shark-skin surfaces for fluid-drag reduction in turbulent flow: a review. *Philosophical Transactions of the Royal Society A: Mathematical, Physical and Engineering Sciences*, **368**(1929):4775–4806.

Dixon, S. and Hall, C. (2014). *Fluid Mechanics and Thermodynamics of Turbomachinery*. Butterworth-Heinemann, Boston, United States.

Doenhoff, A. E. V. and Braslow, A. L. (1961). The effect of distributed surface roughness on laminar flow. In *Boundary Layer and Flow Control*. Pergamon Press.

Domel, A. G., Saadat, M., Weaver, J. C., Haj-Hariri, H., Bertoldi, K., and Lauder, G. V. (2018). Shark skin-inspired designs that improve aerodynamic performance. *Journal of The Royal Society Interface*, **15**(139):20170828.

Dörr, P. C. and Kloker, M. J. (2015). Stabilisation of a three-dimensional boundary layer by base-flow manipulation using plasma actuators. *Journal of Physics D: Applied Physics*, **48**(28):285205.

Dou, Z., Wang, J., and Chen, D. (2012). Bionic research on fish scales for drag reduction. *Journal of Bionic Engineering*, **9**(4):457–464.

Dörr, P. C. and Kloker, M. J. (2018). Numerical investigations on Tollmien-Schlichting wave attenuation using plasma-actuator vortex generators. *AIAA Journal*, **56**(4):1305–1309.

Duriez, T., Aider, J.-L., and Wesfreid, J. E. (2006). Base flow modification by streamwise vortices: Application to the control of separated flows. *ASME Conference Proceedings*, (47519):791–796.

Durst, F. (2006). *Grundlagen der Strömungsmechanik*. Springer, Berlin, Germany.

Durston, N. E., Wan, X., Liu, J. G., and Windsor, S. P. (2019). Avian surface reconstruction in free flight with application to flight stability analysis of a barn owl and peregrine falcon. *Journal of Experimental Biology*, **222**(9).

Eckert, M. (2017). Ludwig Prandtl and the growth of fluid mechanics in Germany. *Comptes Rendus Mécanique*, **345**(7):467–476.

El-Nasr, T. M. A. A. (2017). Age and growth of the fish, *Gerres filamentosus* (Cuvier, 1829) from Hurghada Red Sea, Egypt. *The Egyptian Journal of Aquatic Research*, **43**(3):219–227.

Fransson, J. H. M., Brandt, L., Talamelli, A., and Cossu, C. (2004). Experimental and theoretical investigation of the nonmodal growth of steady streaks in a flat plate boundary layer. *Physics of Fluids*, **16**(10):3627–3638.

Fransson, J. H. M., Brandt, L., Talamelli, A., and Cossu, C. (2005). Experimental study of the stabilization of Tollmien–Schlichting waves by finite amplitude streaks. *Physics of Fluids*, **17**(5):054110.

Fransson, J. H. M., Shahinfar, S., Sattarzadeh, S. S., and Talamelli, A. (2014). Transition to turbulence delay using miniature vortex generators – AFRODITE –. In *Progress in Turbulence V*. Springer, Cham.

Fransson, J. H. M. and Talamelli, A. (2012). On the generation of steady streamwise streaks in flat-plate boundary layers. *Journal of Fluid Mechanics*, **698**:211–234.

Fransson, J. H. M., Talamelli, A., Brandt, L., and Cossu, C. (2006). Delaying transition to turbulence by a passive mechanism. *Physical Review Letters*, **96**:064501.

Gazzola, M., Argentina, M., and Mahadevan, L. (2014). Scaling macroscopic aquatic locomotion. *Nature Physics*, **10**(10):758–761.

Geyer, T., Wasala, S., and Sarradj, E. (2020). Experimental study of airfoil leading edge combs for turbulence interaction noise reduction. *Acoustics*, **2**(2):207–223.

Geyer, T. F., Claus, V. T., Hall, P. M., and Sarradj, E. (2017). Silent owl flight: The effect of the leading edge comb. *International Journal of Aeroacoustics*, **16**(3):115–134.

Goldstein, R. J., Eriksen, V. L., Olson, R. M., and Eckert, E. R. G. (1970). Laminar separation, reattachment, and transition of the flow over a downstream-facing step. *Journal of Basic Engineering*, **92**:732–739.

Graham, R. (1934). The silent flight of owls. *The Aeronautical Journal*, **38**(286):837–843.

Grek, G. R., Katasonov, M. M., Kozlov, V. V., and Chernoray, V. G. (2000). Experimental study of a Λ-structure development and mechanism its transformation into the turbulent spot. In *Laminar-Turbulent Transition*. Springer Berlin Heidelberg.

Helfman, G. S., Collette, B. B., Facey, D. E., and Bowen, B. W. (2009). *The Diversity of Fishes: Biology, Evolution, and Ecology*. A John Wiley & Sons, Ltd, West Sussex, United Kingdom.

Hertel, H. (1963). *Struktur, Form, Bewegung*. Krausskopf-Verlag.

Hosseini, S. M., Tempelmann, D., Hanifi, A., and Henningson, D. S. (2013). Stabilization of a swept-wing boundary layer by distributed roughness elements. *Journal of Fluid Mechanics*, **718**:R1.

Houghton, E., Carpenter, P., Collicott, S. H., and Valentine, D. T. (2017). *Aerodynamics for Engineering Students*. Butterworth-Heinemann, Oxford, United Kingdom.

Ibáñez, A., Cowx, I., and O'higgins, P. (2009). Variation in elasmoid fish scale patterns is informative with regard to taxon and swimming mode. *Zoological Journal of the Linnean Society*, **155**:834–844.

Ikeda, T., Ueda, T., Nakata, T., Noda, R., Tanaka, H., Fujii, T., and Liu, H. (2018). Morphology effects of leading-edge serrations on aerodynamic force production: An integrated study using PIV and force measurements. *Journal of Bionic Engineering*, **15**(4):661–672.

J. Ray, D. and William S., S. (1999). Crossflow stability and transition experiments in swept-wing flow. Technical report.

Jaworski, J. W. and Peake, N. (2020). Aeroacoustics of silent owl flight. *Annual Review of Fluid Mechanics*, **52**(1):395–420.

Jeong, J. and Hussain, F. (1995). On the identification of a vortex. *Journal of Fluid Mechanics*, **285**:69–94.

Jiang, C. G., Xin, S. C., and Wu, C. W. (2011). Drag reduction of a miniature boat with superhydrophobic grille bottom. *AIP Advances*, **1**(3):032148.

Juknevicius, A. and Chong, T. P. (2018). On the leading edge noise and aerodynamics of thin aerofoil subjected to the straight and curved serrations. *Journal of Sound and Vibration*, **425**:324–343.

Juknevicius, A., Chong, T. P., and Woodhead, P. C. (2017). Leading edge noise reduction of thin aerofoil by the straight and curved serrations of the add-on type. In *23rd AIAA/CEAS Aeroacoustics Conference*.

Klän, S., Bachmann, T., Klaas, M., Wagner, H., and Schröder, W. (2009). Experimental analysis of the flow field over a novel owl based airfoil. *Experiments in Fluids*, **46**(5):975–989.

Klän, S., Bachmann, T., Klaas, M., Wagner, H., and Schröder, W. (2010). Experimental analysis of the flow field over a novel owl based airfoil. In *Animal Locomotion*. Springer.

Kloker, M. (2008). Advanced laminar flow control on a swept wing - Useful crossflow vortices and suction. In *38th Fluid Dynamic Conference and Exhibit*.

Kroeger, R., Grushka, H., and Helvey, T. (1972). Low speed aerodynamics for ultra-quiet flight. Technical report.

Kruse, M. and Wagner, S. (1996). LDA measurements of laminar–turbulent transition in a flat-plate boundary layer. In *8th International Symposium on Applications of Laser Techniques to Fluid Mechanics*.

Kunze, S. and Bruecker, C. (2011). Flow control over an undulating membrane. *Experiments in Fluids*, **50**(3):747–759.

Lang, M., Rist, U., and Wagner, S. (2004). Investigations on controlled transition development in a laminar separation bubble by means of LDA and PIV. *Experiments in Fluids*, **36**(1):43–52.

Lauder, G. V., Wainwright, D. K., Domel, A. G., Weaver, J. C., Wen, L., and Bertoldi, K. (2016). Structure, biomimetics, and fluid dynamics of fish skin surfaces. *Physical Review Fluids*, **1**:060502.

Lilley, G. (1998). A study of the silent flight of the owl. In *4th AIAA/CEAS Aeroacoustics conference*.

Lin, J. C., Robinson, S. K., McGhee, R. J., and Valarezo, W. O. (1994). Separation control on high-lift airfoils via micro-vortex generators. *Journal of Aircraft*, **31**(6):1317–1323.

Lin, R. S. and Malik, M. R. (1997). On the stability of attachment-line boundary layers. part 2. the effect of leading-edge curvature. *Journal of Fluid Mechanics*, **333**:125–137.

Mebs, T. and Scherzinger, W. (2000). *Die Eulen Europas : Biologie, Kennzeichen, Bestände*. Franckh-Kosmos, Stuttgart.

Merzkirch, W. (2012). *Flow Visualization*. Academic Press, London.

Muthuramalingam, M., Villemin, L. S., and Bruecker, C. (2019). Streak formation in flow over biomimetic fish scale arrays. *Journal of Experimental Biology*, **222**(16).

Narayanan, S., Chaitanya, P., Haeri, S., Joseph, P., Kim, J. W., and Polacsek, C. (2015). Airfoil noise reductions through leading edge serrations. *Physics of Fluids*, **27**(2):025109.

Nelson, J. S. (2007). *Fishes of the World*. John Wiley and Sons, Inc, USA.

Neuhaus, W., Bretting, H., and Schweizer, B. (1973). Morphologische und funktionelle untersuchungen über den "lautlosen" flug der eulen (Strix aluco) im vergleich zum flug der enten (Anas platyrhynchos). *Biologisches Zentralblatt*, **92**:495–512.

Oeffner, J. and Lauder, G. V. (2012). The hydrodynamic function of shark skin and two biomimetic applications. *Journal of Experimental Biology*, **215**(5):785–795.

Olivier, D., Vandewalle, N., Mauguit, Q., and Parmentier, É. (2013). Kinematic analysis of swimming ontogeny in seabass (*Dicentrarchus labrax*). *Belgian Journal of Zoology*, **143**(1):79–91.

Ou, J., Perot, B., and Rothstein, J. P. (2004). Laminar drag reduction in microchannels using ultrahydrophobic surfaces. *Physics of Fluids*, **16**(12):4635–4643.

Panton, R. (2013). *Incompressible Flow*. John Wiley and Sons, Ltd, Hoboken, New Jersey.

Paul, I., Prakash, K. A., and Vengadesan, S. (2014). Onset of laminar separation and vortex shedding in flow past unconfined elliptic cylinders. *Physics of Fluids*, **26**(2):023601.

Pavlov, V., Riedeberger, D., Rist, U., and Siebert, U. (2012). Analysis of the relation between skin morphology and local flow conditions for a fast-swimming dolphin. In *Nature-Inspired Fluid Mechanics*. Springer.

Puckert, D. K. (2019). *Experimental investigation on global instability and critical Reynolds number in roughness-induced laminar-to-turbulent transition*. PhD thesis, Universität Stuttgart.

Puckert, D. K., Dieterle, M., and Rist, U. (2017). Reduction of freestream turbulence at low velocities. *Experiments in Fluids*, **58**(5):45.

Puckert, D. K. and Rist, U. (2018). Experiments on critical Reynolds number and global instability in roughness-induced laminar–turbulent transition. *Journal of Fluid Mechanics*, **844**:878–904.

Puckert, D. K. and Rist, U. (2020). Transition delay with cylindrical roughness elements in a laminar water channel. In *New Results in Numerical and Experimental Fluid Mechanics XII*. Springer.

Radeztsky, R. H., Reibert, M. S., and Saric, W. S. (1999). Effect of isolated micron-sized roughness on transition in swept-wing flows. *AIAA Journal*, **37**(11):1370–1377.

Raffel, M., Willert, C. E., Wereley, S. T., and Kompenhans, J. (2007). *Particle Image Velocimetry: A Practical Guide*. Springer, Berlin, Heidelberg.

Rao, C., Ikeda, T., Nakata, T., and Liu, H. (2017). Owl-inspired leading-edge serrations play a crucial role in aerodynamic force production and sound suppression. *Bioinspiration & Biomimetics*, **12**(4):046008.

Rist, U. and Fasel, H. (1995). Direct numerical simulation of controlled transition in a flat-plate boundary layer. *Journal of Fluid Mechanics*, **298**:211–248.

Rizzetta, D. P. and Visbal, M. R. (2007). Direct numerical simulations of flow past an array of distributed roughness elements. *AIAA Journal*, **45**(8):1967–1976.

Rosen, M. W. and Cornford, N. E. (1971). Fluid friction of fish slimes. *Nature*, **234**(5323):49–51.

Roy, A. S. (2018). Analysis and control of boundary layer transition on a NACA-0008 wing profile.

Saric, W., Ruben Carrillo, J., and Reibert, M. (1998). Leading-edge roughness as a transition control mechanism. In *36th AIAA Aerospace Sciences Meeting and Exhibit*.

Saric, W. S. (1986). Visualization of different transition mechanisms. *The Physics of Fluids*, **29**(9):2770–2770.

Saric, W. S., Reed, H. L., and White, E. B. (2003). Stability and transition of three-dimensional boundary layers. *Annual Review of Fluid Mechanics*, **35**(1):413–440.

Sayadi, T., Hamman, C. W., and Moin, P. (2013). Direct numerical simulation of complete H-type and K-type transitions with implications for the dynamics of turbulent boundary layers. *Journal of Fluid Mechanics*, **724**:480–509.

Schlatter, P., Deusebio, E., de Lange, R., and Brandt, L. (2010). Numerical study of the stabilisation of boundary-layer disturbances by finite amplitude streaks. *International Journal of Flow Control*, **2**:259–288.

Schlichting, H. and Gersten, K. (2017). *Boundary-Layer Theory*. Springer, Berlin, Heidelberg.

Schubauer, G. B. and Skramstad, H. K. (1947). Laminar boundary-layer oscillations and stability of laminar flow. *Journal of the Aeronautical Sciences*, **14**(2):69–78.

Selig, M. S., Maughmer, M. D., and Somers, D. M. (1995). Natural-laminar-flow airfoil for general-aviation applications. *Journal of Aircraft*, **32**(4):710–715.

Serpieri, J. and Kotsonis, M. (2015). Flow visualization of swept wing boundary layer transition. In *10th Pacific Symposium on Flow Visualization and Image Processing*.

Serpieri, J. and Kotsonis, M. (2016). Three-dimensional organisation of primary and secondary crossflow instability. *Journal of Fluid Mechanics*, **799**:200–245.

Serpieri, J., Yadala Venkata, S., and Kotsonis, M. (2017). Conditioning of cross-flow instability modes using dielectric barrier discharge plasma actuators. *Journal of Fluid Mechanics*, **833**:164–205.

Shahinfar, S., Sattarzadeh, S. S., Fransson, J. H. M., and Talamelli, A. (2012). Revival of classical vortex generators now for transition delay. *Physical Review Letters*, **109**:074501.

Siconolfi, L., Camarri, S., and Fransson, J. H. M. (2015). Boundary layer stabilization using free-stream vortices. *Journal of Fluid Mechanics*, **764**:R2.

Singh, K. and Lumley, J. L. (1971). Effect of roughness on the velocity profile of a laminar boundary layer. *Applied Scientific Research*, **24**(1):168–186.

Squire, L. C. (1961). The motion of a thin oil sheet under the steady boundary layer on a body. *Journal of Fluid Mechanics*, **11**(2):161–179.

Stenum, J. (2018). Slow swimming exhausts fish. *Journal of Experimental Biology*, **221**(5).

Uranga, A., Persson, P.-O., Drela, M., and Peraire, J. Preliminary investigation into the effects of cross-flow on low Reynolds number transition. In *20th AIAA Computational Fluid Dynamics Conference*.

Ustinov, M. and Ivanov, A. (2018). Cross-flow dominated transition control by surface micro-relief. *AIP Conference Proceedings*, **2027**.

Wagner, H., Weger, M., Klaas, M., and Schröder, W. (2017). Features of owl wings that promote silent flight. *Interface focus*, **7**(1):20160078.

Wainwright, D. K. and Lauder, G. V. (2016). Three-dimensional analysis of scale morphology in bluegill sunfish, *Lepomis macrochirus*. *Zoology*, **119**(3):182–195.

Wainwright, D. K. and Lauder, G. V. (2017). *Mucus Matters: The Slippery and Complex Surfaces of Fish*. Springer International Publishing, Cham.

Wainwright, D. K., Lauder, G. V., and Weaver, J. C. (2017). Imaging biological surface topography in situ and in vivo. *Methods in Ecology and Evolution*, **8**(11):1626–1638.

Wassermann, P. and Kloker, M. (2002). Mechanisms and passive control of crossflow-vortex-induced transition in a three-dimensional boundary layer. *Journal of Fluid Mechanics*, **456**:49–84.

Watmuff, J. H. (2014). Stability characteristics of low-amplitude jets in cross-flow. In *19th Australasian Fluid Mechanics Conference*.

Weger, M. and Wagner, H. (2016). Morphological variations of leading-edge serrations in owls (*Strigiformes*). *PLoS One*, **11**(3):1–21.

Wei, Y., Xu, F., Bian, S., and Kong, D. (2020). Noise reduction of UAV using biomimetic propellers with varied morphologies leading-edge serration. *Journal of Bionic Engineering*, **17**:767–779.

Wen, L., Weaver, J. C., and Lauder, G. V. (2014). Biomimetic shark skin: design, fabrication and hydrodynamic function. *Journal of Experimental Biology*, **217**(10):1656–1666.

White, E. and Saric, W. Application of variable leading-edge roughness for transition control on swept wings. In *38th Aerospace Sciences Meeting and Exhibit*.

White, F. M. (2006). *Viscous Fluid Flow*. McGraw-Hill, Singapore.

Wiegand, T. (1996). *Experimentelle untersuchungen zum laminar-turbulenten transitionsprozess eines wellenzugs in einer plattengrenzschicht*. PhD thesis, Universität Stuttgart.

Winzen, A., Roidl, B., Klän, S., Klaas, M., and Schröder, W. (2014). Particle-Image Velocimetry and force measurements of leading-edge serrations on owl-based wing models. *Journal of Bionic Engineering*, **11**(3):423–438.

Wu, L., Jiao, Z., Song, Y., Liu, C., Wang, H., and Yan, Y. (2018). Experimental investigations on drag-reduction characteristics of bionic surface with water-trapping microstructures of fish scales. *Scientific Reports*, **8**(1):12186.

Yadala, S., Hehner, M. T., Serpieri, J., Benard, N., Dörr, P. C., Kloker, M. J., and Kotsonis, M. (2018). Experimental control of swept-wing transition through base-flow modification by plasma actuators. *Journal of Fluid Mechanics*, **844**:R2.

Yanase, K. and Saarenrinne, P. (2015). Unsteady turbulent boundary layers in swimming rainbow trout. *Journal of Experimental Biology*, **218**(9):1373–1385.

Yarusevych, S., Sullivan, P. E., and Kawall, J. G. (2009). On vortex shedding from an airfoil in low-Reynolds-number flows. *Journal of Fluid Mechanics*, **632**:245–271.

Zhang, J., Xu, M., Pollard, A., and Mi, J. (2013). Effects of external intermittency and mean shear on the spectral inertial-range exponent in a turbulent square jet. *Physical Review E*, **87**:053009.